

**COHERENT INTERACTIONS
IN ON-CHIP PHOTONIC-CRYSTAL CAVITIES**

A DISSERTATION
SUBMITTED TO THE DEPARTMENT OF
MATERIALS SCIENCE AND ENGINEERING
AND THE COMMITTEE ON GRADUATE STUDIES
OF STANFORD UNIVERSITY
IN PARTIAL FULFILLMENT OF THE REQUIREMENTS
FOR THE DEGREE OF
DOCTOR OF PHILOSOPHY

Jun Pan

May 2010

© 2010 by Pan Jun. All Rights Reserved.

Re-distributed by Stanford University under license with the author.

This dissertation is online at: <http://purl.stanford.edu/rj901qh4677>

I certify that I have read this dissertation and that, in my opinion, it is fully adequate in scope and quality as a dissertation for the degree of Doctor of Philosophy.

James Harris, Primary Adviser

I certify that I have read this dissertation and that, in my opinion, it is fully adequate in scope and quality as a dissertation for the degree of Doctor of Philosophy.

Mark Brongersma

I certify that I have read this dissertation and that, in my opinion, it is fully adequate in scope and quality as a dissertation for the degree of Doctor of Philosophy.

Shanhui Fan

Approved for the Stanford University Committee on Graduate Studies.

Patricia J. Gumport, Vice Provost Graduate Education

This signature page was generated electronically upon submission of this dissertation in electronic format. An original signed hard copy of the signature page is on file in University Archives.

ABSTRACT

There has been substantial interest in study of coherent interactions in on-chip photonic-crystal microcavities. Such efforts have recently led to realizations of important phenomena, including an all-optical analogue to electromagnetically induced transparency (EIT) and flat-top reflection filters. In this work, we demonstrate EIT-like and flat-top reflection optical resonances in a single on-chip photonic-crystal cavity structure. Most importantly, by tuning the index of refraction and thus the propagation phase in the waveguide between two cavities, we smoothly change the behavior of the structure from EIT-like to flat-top optical resonance. Both resonances are of great significance in applications. EIT-like optical resonance renders an integrated optical system transparent over a very narrow frequency range. The potential for slowing and stopping light on chip in such a system has profound impacts in both fundamental science and optical communications. Flat-top reflection filter, which reflects a narrow range of wavelengths while letting other wavelengths pass through, is a higher-order filter compared to the regular Lorentzian response commonly observed in photonic-crystal resonator filters. This box-like lineshape, featuring a flattened resonance and sharp transition from transmission band to reflection band, is important for achieving low inter-channel cross-talk in wavelength-division multiplexing.

In addition, we show an optical analogue to the superradiance effect in photonic-crystal cavities. This work is along the direction of recent substantial interest and

progress in mapping coherent effects in atomic systems to on-chip nanophotonics systems. But unlike the previous demonstration in atomic systems where emitters have to be placed within a distance smaller than a wavelength, the two resonators in our system can be separated by a distance much larger than a wavelength. It is enabled by the use of a waveguide to enforce the coherent interaction in a one-dimensional regime. The effect enhances waveguide-resonator coupling, which is essential for low loss device operation, so has broad implications for on-chip photonic integration. Moreover, using laser-pumped thermal differential tuning to align and detune cavity resonances, we experimentally demonstrate structural tuning of the superradiance effect in the system.

ACKNOWLEDGMENTS

During the course of my Ph.D. work, I owe many thanks to a great number of people, without whom this work would not have been possible.

First, I must acknowledge my principal advisor, Professor Harris, known as “The Coach”. He is an amazing advisor. On one hand, he gave me plenty of flexibility in research and encouraged me to work independently. On the other hand, he was always there to provide guidance and resources when necessary. It is a great honor to be part of the Harris group. I am truly impressed by Professor Harris’s ability to adapt his research focus as well as the diversity of the research projects under his supervision.

Professors Shanhui Fan and Martin Fejer, along with Professor Harris, are the co-PIs of this research project. I am very grateful for their guidance and suggestions, which are absolutely critical in this project. Professor Fan is one of the pioneers in photonic crystal research. His insights were invaluable from initiation to implementation in this work. There would not have been this project in the first place if there were not his novel idea of stopping light in a dynamic system. Professor Fejer regularly spent a substantial amount time from his busy schedule to help us overcome the difficulties in the project. His expertise helped us solve many problems in different aspects of the experimental work. I am also amazed by Professor Fejer’s wide range of knowledge.

I would like to thank Professor Brongersma for spending his precious time to participate in many milestone events in my Ph.D. program. He sat on my qualifying exam, dissertation reading, and oral exam committees.

I am very thankful to the entire research team, Yijie, for his tremendous help and work on optical measurements, Sunil and Michelle, for the theory, design, FDTD simulation, and even paper writing, Norbert, for his current work on thermal modeling, and Kazuhiko and Luigi for their help in teaching me the e-beam lithography and etching techniques that became central fabrication elements of this project in the first year of my Ph.D. research.

Gail, the “Chief Operating Officer” of the Harris group, deserves special recognition for her efforts to keep the group running smoothly.

In the past few years, I spent many long days and nights in the SNF clean room. I would like to thank the SNF staff and members for making it a great community, in particular, James, Maurice, Nancy, Eric, Sanja and Sora for discussing fabrication issues and generously sharing their experience.

In the end I would like to thank the Harris group and other neighbors in the basement of Allen-X for providing a rich intellectual and social environment.

TABLE OF CONTENTS

Abstract.....	iv
Acknowledgments.....	vi
Table of Contents.....	viii
List of tables.....	x
List of figures.....	xi
1. Introduction.....	1
1.1. Photonic Crystals.....	1
1.2. Electromagnetically Induced Transparency.....	4
1.2.1. EIT in Atomic Systems.....	4
1.2.2. Optical Analogue to EIT.....	5
1.2.3. Stopping Light.....	7
1.3. Flat-Top Reflection Filter.....	10
1.4. Optical Analogue to the Superradiance Effect.....	12
2. Coupled-Mode Theory.....	14
2.1. Single Cavity Side-Coupled to a Waveguide.....	14
2.2. Two Cavities Side-Coupled to a Waveguide.....	19
2.2.1. General Theoretical Calculation.....	19
2.2.2. The Propagation Phase.....	23
2.2.3. Optical Analogue to the Superradiance Effect.....	27
3. Structure Design.....	32
3.1. Photonic-Crystal Slab.....	33
3.2. Strip Waveguides.....	37
3.3. Device Layout.....	39
4. Fabrication.....	41
4.1. Overview.....	41

4.2.	Pattern Transfer.....	50
4.3.	Selective Membrane Release	52
4.4.	SEM-Based Fabrication Analysis.....	57
5.	Post-Fabrication Tuning.....	63
5.1.	Laser-Pumped Tuning.....	64
5.1.1.	Diffusion Length of Free Carriers.....	67
5.1.2.	Spatial Characterization of Thermal and Free-Carrier Effects	68
5.1.3.	Estimation of Free-Carrier Concentration	70
5.2.	Differential Tuning to Align Cavity Resonances.....	72
6.	Experiments	77
6.1.	Experimental Setup.....	77
6.2.	Tuning the Propagation Phase	79
6.2.1.	Device under Test	79
6.2.2.	Transmission Spectra.....	81
6.2.3.	Estimation of Index Change.....	85
6.3.	EIT-like Optical Resonance and Group Delay	86
6.4.	Optical Analogue to the Superradiance Effect.....	90
6.4.1.	Experimental Results and Theoretical Fitting.....	90
6.4.2.	Resonator Separation	95
7.	Conclusion	98
8.	Bibliography	102

LIST OF TABLES

<i>Number</i>	<i>Page</i>
Table 5.1. Carrier concentration estimated from the increased intrinsic loss or decreased intrinsic quality factor, which is extracted from Figure 5.3.	71
Table 6.1. The parameters used in Equation (2.21)-(2.23) to fit the experimental curves in Figure 6.3. The second column is the power of the laser beam that is delivered to the sample. In the remaining columns the subscripts A or B label the two resonators. $\lambda_{A,B}$ are the resonant wavelengths. $Q_{\text{int},A}$ and $Q_{\text{int},B}$ are the intrinsic quality factors. $Q_{c,A}$ and $Q_{c,B}$ are the waveguide-resonator coupling quality factors. ϕ_0 is a parameter that determines the waveguide propagation phase $\phi_{\text{wg}}(\omega) = \tau\omega + \phi_0$, where $\tau = -6.0 \times 10^{-12}$ sec as calculated by the finite-difference time-domain simulation.....	83

LIST OF FIGURES

<i>Number</i>	<i>Page</i>
Figure 1.1. Scanning electron microscope (SEM) graph of an example of suspended photonic-crystal slab consisting of air holes. A cavity was created by filling five consecutive air holes. A waveguide was generated by filling a row of air holes.	3
Figure 1.2. The schematics of the general condition for stopping light. (a) The state that the system bandwidth is large in order to accommodate a signal with a given bandwidth. (b) The state that the system bandwidth is compressed and the group velocity is reduced. An adiabatic transition between the two states stops and releases a light pulse. [30].....	8
Figure 1.3. Transmission spectrum of a structure with two cavities side-coupled to one waveguide. The linewidth of the central transmission peak is highly sensitive to the frequency detuning of the two cavities. In plotting the curves, we assume two intrinsically lossless resonators with same coupling rate to a waveguide γ . The resonant frequencies are detuned at various numbers $\omega_{1,2} = \omega_0 \pm \Delta\omega / 2$. (a) $\Delta\omega = 1.5\gamma$ (b) $\Delta\omega = 0.5\gamma$ (c) $\Delta\omega = 0.1\gamma$. The distance along the waveguide between two resonators is $L = \pi c / \omega_0$ and the waveguide satisfies a dispersion relation $\beta(\omega) = \omega / c$, where c is the speed of light in the waveguide.....	9
Figure 1.4. Comparison of a Lorentzian (blue curve) and flat-top reflection lineshape. The flat-top reflection optical resonance features a flattened resonance and sharper transition from the reflection band to the transmission band as compared to the Lorentzian lineshape.	11
Figure 2.1. Illustration of a structure with one microcavity side-coupled to one waveguide. S_{m+} ($m=1,2$) are amplitudes of the waveguide modes going	

toward the cavity, and S_{m-} ($m=1,2$) are amplitudes of the waveguide modes going away from the cavity. $S_{1\pm}$ represent of the modes in the left part of the waveguide with respect to the cavity, and $S_{2\pm}$ represent the modes in the right part of the waveguide.15

Figure 2.2. Illustration of a structure with two cavities side-coupled to one waveguide.

E_i is the incident fields, E_c is the circulation fields in the waveguide between the cavities, and E_t is the transmitted fields.20

Figure 2.3. Graphical illustration of the transmission spectra computed with coupled-mode theory. In plotting the curves, we assume two intrinsically lossless resonators with the same coupling rate to a waveguide: $\gamma_{A,B}^i = 0$, $\gamma_{A,B}^c = \gamma$.

The resonance frequencies are detuned at an arbitrary small number, $\omega_{A,B} = \omega_0 \pm \frac{\delta\omega}{2}$, and here we let $\delta\omega = 0.8\gamma$. We also assume that the

waveguide has a linear dispersion relation $\phi_{wg}(\omega) = -0.2 \frac{\omega - \omega_0}{\gamma} + \hat{\phi}$. (a)

EIT-like transmission spectrum when $\phi_{wg}(\omega_0) = 2n\pi$. (b) Flat-top

reflection filter when $\phi_{wg}(\omega_0) = (2n + 1)\pi$ 26

Figure 2.4. Transmission spectra (black curves) of the two intrinsically lossy cavities side-coupled to one waveguide. This configuration is directly compared to

Figure 1.3 in which cavities are intrinsically lossless. In plotting the curves, we assume waveguide-cavity coupling rate γ_c equals γ and cavity intrinsic

loss rate $\gamma_i = \gamma/10$. The resonant frequencies are detuned at various numbers $\omega_{1,2} = \omega_0 \pm \Delta\omega/2$. (a) $\Delta\omega = 1.5\gamma$ (b) $\Delta\omega = 0.5\gamma$ (c) $\Delta\omega = 0.1\gamma$.

The distance along the waveguide between two resonators is $L = \pi c / \omega_0$ and the waveguide satisfies a dispersion relation $\beta(\omega) = \omega / c$, where c is the speed of light in the waveguide. As a reference, the red dashed curve is

the Lorentzian-shaped transmission dip generated by a single cavity.30

Figure 3.1. Schematic of the device structure. The photonic crystal is etched into a suspended silicon membrane. The input and output strip waveguides, which are surrounded by oxide claddings, are coupled to the photonic-crystal waveguide. The strip waveguides are tapered at the coupling facet to reduce back-reflections. Top insert: SEM of the interface between the photonic-crystal waveguide and the strip waveguide. Bottom insert: SEM of the cross section of the inverse taper.	32
Figure 3.2. SEM graph of a fabricated photonic-crystal slab. The photonic crystal is formed by air holes in a triangular lattice in a silicon slab. The line defect, missing one row of air holes, is a waveguide. The point defect, missing five consecutive holes, is a cavity. The two cavities are separated by a distance L . Inserts: magnified view of the cavities and part of the waveguide.	34
Figure 3.3. Transmission spectrum of a photonic-crystal structure calculated with FDTD simulation. The two-cavity structure gives rise to an optical analogue of electromagnetically-induced transparency, with a transmission spectrum featuring a narrow transparency peak within a broad transmission dip. (Courtesy of Sunil Sandhu and Professor Shanhui Fan)	36
Figure 3.4. Comparison of the transmission spectra from devices (a) without and (b) with inverse tapers at coupling facets. (a) The prominent oscillations are due to strong back reflections at coupling facets. Features from coherent interactions are mixed with the oscillation noise. Experimental results are ambiguous, and could be fitted by multiple theoretical curves, <i>e.g.</i> either the red or blue dashed curves. (b) Oscillations are suppressed by the use of inverse tapers. The red theoretical curve fits well with the blue experimental result.	38
Figure 4.1. Schematics of the steps of (a) bi-layer lithography (b) metal evaporation (c) life-off.	48
Figure 4.2. SEM of a completed device. The photonic crystal membrane is suspended. The strip waveguides extend to the oxide cladding.	50

Figure 4.3. Comparison of cross sections of the photonic crystal air holes in silicon slabs. (a) Patterns transferred from PMMA to silicon directly. (b) Patterns transferred from PMMA to oxide and then to silicon. Method (b) results in much more vertical side walls.....	51
Figure 4.4. Examples of unsatisfactory photonic crystals etched by over-heated processes.	52
Figure 4.5. Results of membrane release with SU-8 masks. (a) and (b) shows optical microscopic images of the two ends of a same waveguide. The left part survived and right part suffered HF leakage and collapsed. (c) SEM of a released photonic crystal membrane with connected strip waveguides. The waveguide on the right hand side of the photonic crystal was good but the part on the left hand side collapsed. In conclusion, SU-8 mask provides inconsistent results. Figure (c) also shows some hard-to-remove SU-8 residues.	53
Figure 4.6. Gold coverage. (a) Evaporation process resulted in poor coverage of gold mask at the edge of the strip waveguide. (b) The deposited oxide cladding smoothed the surface and significantly improved the coverage of gold.....	54
Figure 4.7. 3 μ m-thick oxide. (a) Deposited by the “sts” PECVD system, and annealed at 1100 °C for 1 hour. (b) Dipped in 10:1 HF for 5 minutes. (c) Placed in 10:1 HF for 25 minutes with a gold mask. The gold mask was removed before taking this picture.	55
Figure 4.8. Results of low temperature oxide (LTO) deposited in the “tylanbpg” tube. (a) Without annealing. (b) Annealed at 1100 °C for 1 hour.....	56
Figure 4.9. Results of the oxide deposited in the “teos2” tube. (a) Cross section of the strip waveguide surrounded by oxide cladding. (b) Top view of the interface between the suspended waveguide and the cladding-supported waveguide.	56
Figure 4.10. Etching rate of the oxide deposited in the “teos2” tube, etched with 10:1 HF. The average etching rate is 570 Å/min, the slowest among all the deposited oxide tested.	57

Figure 4.11. Digitization and combination of SEM graphs. (a) Original SEM graphs around a photonic-crystal cavity with the same magnification, orientation, brightness and contrast. (b) SEM graphs are converted to black-and-white images, and combined into a single image.	59
Figure 4.12. Analysis of air hole diameters in a fabricated photonic-crystal slab. (a) Histogram of hole diameter. The mean is 217nm and the standard deviation is 2.0nm. Smaller air holes along the waveguide and cavity are not counted. (b) Mean of extracted value of the hole diameter increases monotonically with the conversion threshold. But the standard deviation is almost a constant. So the analysis of uniformity is not affected by the choice of the threshold.	60
Figure 4.13. Analysis of the lattice constant in a fabricated photonic-crystal slab. (a) Histogram of the distance between adjacent holes. The mean is 385nm and the standard deviation 2.7nm. (b) Orientation analysis of the nearest-neighbor distance. Distances in three orientations mix well and no obvious orientation dependence is observed.	61
Figure 5.1. Single cavity tuning by a laser focused at an area a few microns away from the cavity. (a) SEM of the cavity and illustration of the laser spot by the green dot. (b) Transmission spectra in the presence of the pumping laser with different laser powers. The transmission dip corresponds to the cavity resonance. The resonance shifts to a longer wavelength with increased laser power.	65
Figure 5.2. Single cavity tuning by a laser focused on the cavity. (a) SEM of the cavity and illustration of the laser spot by the green dot. (b) Transmission spectra in the presence of the pumping laser with different laser powers. The transmission dip corresponds to the cavity resonance. In addition to the redshift, the depth of the transmission dip decreased with increased laser power, due to injected free carriers, which induced excessive material loss.	67

Figure 5.3. Spatial characterization of thermal and free-carrier effects in the slab. (a) SEM of the cavity and illustration of the laser spot scanning pathways. The blue pathways went through the cavity and the red one was $3\mu\text{m}$ away. (b) Redshift of the cavity resonant wavelength as a function of the laser position. (c) Depth of the transmission dip as a function of the laser position.	69
Figure 5.4. SEM images of the fabricated device. (a) Top view of the PhC structure with two cavities. (b) Magnified view of microcavity C1.	73
Figure 5.5. Experimental results of laser-pumped thermal tuning of photonic-crystal microcavities with laser pump light focused near microcavity C1. (a) Transmission spectra for pump powers between 0 and 6.7 mW. Solid, black lines show experimental data, and red, dashed lines show theoretical fits. (b) Resonance wavelengths (dip positions) as a function of pump power.	74
Figure 6.1. Schematic of the experimental setup. Sample waveguide is placed on a XYZ stage. In the horizontal direction, light from a tunable laser source is first coupled to the waveguide, and the transmitted power is detected at the other side of the waveguide. Above the sample, a microscope column is attached to another XYZ stage. Pumping laser beams are focused by the objective lens on the sample. A CCD camera, at the top of the column, is used to locate and monitor the laser spot and the cavity.	78
Figure 6.2. SEM images of the fabricated device for the demonstration of EIT-like optical resonance and flat-top reflection filter. (a) Top view of the photonic-crystal structure with two cavities side-coupled to one waveguide. (b) Magnified view of the microcavity C_B . The circle approximately corresponds to the size of the focal spot of the pumping laser. The actual heated region however is substantially larger due to thermal conductance.	80
Figure 6.3. Experimental transmission spectra (blue solid line) and theoretical fits (red dashed line) of the photonic-crystal system of Figure 6.2, with a pump laser beam incident on the waveguide near the mid-point between the two	

microcavities. Curves (a) – (d) correspond to different pump powers. In particular, curves (a)(b)(d) exhibit a lineshape analogous to electromagnetically-induced transparency, with the transparency peak of 0.08, 0.07 and 0.15 in linewidth respectively, corresponding to a quality factor of 19800, 22600 and 10500 respectively, which are all substantially larger than the loaded Q of each individual cavity. Curve (c) exhibits a flat-top reflection response. The detuning of the two cavity resonances is 0.26, 0.26, 0.36 and 0.45 nm respectively in curves (a) – (d).....82

Figure 6.4. The solid line is the calculated delay for the EIT-like spectrum in Figure 6.3(b), using parameters in Table 6.1. The dashed line is the delay as obtained from a sum of contributions from the two individual resonances and the propagation in the waveguide. Notice the significant excess delay due to the coherent interference between the two resonances.87

Figure 6.5. Delay spectrum of an EIT-like optical system. The blue curve is theoretically inferred group delay from the transmission spectrum. The red dots are experimentally measured delays. A maximum delay of 20 ps was generated by the EIT-like optical resonance.....88

Figure 6.6. Theoretical transmission spectra and corresponding delay spectra of an EIT-like system with different cavity resonance detuning. In plotting the blue curves, fitting parameters for Figure 6.3(b) in Table 6.1 are used. In plotting the red and black curves, the resonant wavelength of cavity A was decreased by 0.1 nm incrementally and that of cavity B was increased by 0.1 nm incrementally.89

Figure 6.7. SEM images of the fabricated device for demonstration of the superradiance effect. (a) Top view of the PhC structure with two resonators. (b) Magnified view of a single resonator and a portion of waveguide.91

Figure 6.8. Experimental transmission spectrum (solid line) and theoretical fits (dashed line) for the two-resonator system shown in Figure 6.7 at different resonance frequency detuning $\Delta\lambda$ between resonators: (a) $\Delta\lambda = 0.65\text{nm}$,

(b) $\Delta\lambda = 0.17\text{nm}$, (c) $\Delta\lambda = 0\text{nm}$. Plots in (a) include the theoretical transmission spectrum (dotted line) of a single-resonator system with coupling rate γ_c , and plots in (c) include the theoretical transmission spectrum (dotted line) of a single-resonator system with coupling rate $2\gamma_c$. The inset of (c) shows the depth of the experimental transmission dip (solid line) is deeper compared with the depth of the single-resonator system experimental transmission dip (dashed line) from (a), indicating enhancement of waveguide-resonance coupling in the superradiance regime of the two-resonator system.....92

Figure 6.9. Comparison of experimental transmission spectrum of the two-resonator system using an incoherent ASE source (solid line), and a tunable coherent laser source (dashed line). Plots show system at different resonance frequency detunings, $\Delta\lambda$, between resonators.....94

Figure 6.10. Theoretical plots from coupled-mode theory showing the power transmission spectrum (left, solid line) and the impulse response (right, solid line) for different cavity separations L in Figure 1. Plots in (b) and (c) include the $L = 0$ plots (dotted line).....97

1. INTRODUCTION

1.1. PHOTONIC CRYSTALS

A photonic crystal [1] is a periodic arrangement of media with differing dielectric constants. Even though the term was not introduced until 1987, photonic crystals exist in nature and were studied in one way or another scientifically more than a century ago. One-dimensional photonic crystals in the form of multilayer dielectric stacks were first explained by Lord Rayleigh in 1887 [2]. When incident on a multilayer film, such as a quarter-wave stack, light of proper wavelength is completely transmitted. The reason is that the light wave is partially reflected at each layer interface and, if the spacing is periodic, the multiple reflections of the incident wave interfere destructively to eliminate the back-reflecting wave. This principle led to many applications, such as anti-reflection coatings.

The ideas of photonic band gaps and higher-dimensional photonic crystals grew and blossomed after the two milestone papers published by Eli Yablonovitch [3] and Sajeev John [4], which provided a basic platform for controlling the flow of light. The analogy for photonic crystal is the successful model for electronic materials, crystal, in which atoms and molecules are repeated in space to form a lattice, and present a periodic potential to an electron propagating through it. The theory of quantum mechanics explains that electrons propagate as waves, and that there are gaps in the energy band

structure for these periodic structures, meaning that electrons with certain energies are forbidden to propagate in certain directions. Now, in photonic crystals, the atoms and molecules are replaced by macroscopic media, and the periodic potential is replaced by a periodic index of refraction. The structures can produce many of the same phenomena for photons that the atomic potential produces for electrons. Through extensive studies of the past two decades, researchers have predicted and demonstrated many important properties of these crystals. Photonic band gaps have been used to prevent light from propagating in certain directions with specified frequencies, and more importantly, allow propagation in various useful ways.

Depending on the dimension of the periodicity, there are one-, two- and three-dimensional photonic crystals. However, one- and two-dimensional photonic crystals, which require homogeneity in the remaining two and one dimension respectively, are just imaginary structures. A three-dimensional photonic crystal, an optical analogue to an ordinary crystal, can confine light in all three dimensions. Nevertheless, the actual fabrication of a structure that is periodic in all three dimensions remains difficult. Hybrid structures, such as photonic-crystal slabs, confine light in three dimensions by a combination of photonic band gaps and index guiding (or total internal reflection in the language of ray-optics). They can be fabricated based on two-dimensional patterns by techniques used in the integrated circuits industry, so they are widely used in research and applications. For this reason, photonic-crystal slabs are adopted in the work contained in this dissertation.

Photonic-crystal slabs resemble the two-dimensional photonic crystal, but have finite thickness in the vertical direction. The confinement of light in the vertical dimension is enforced by index guiding. But qualitatively new behavior is introduced by the finite thickness. A primary difference between the case of a slab and the case of a truly two-dimensional photonic crystal is that the band diagram of the slab has a light cone. Like in two-dimensional photonic crystals, a waveguide can be generated by introducing a line defect in the photonic-crystal slabs. In particular, one can change the average dielectric constant along a particular line. A fabricated sample of such a waveguide is shown in Figure 1.1. Similarly, we can create a resonant cavity to trap a localized mode by generating a point defect. However, the presence of the line cone means that localized modes in the slab are leaky resonances, with intrinsic vertical radiation losses.

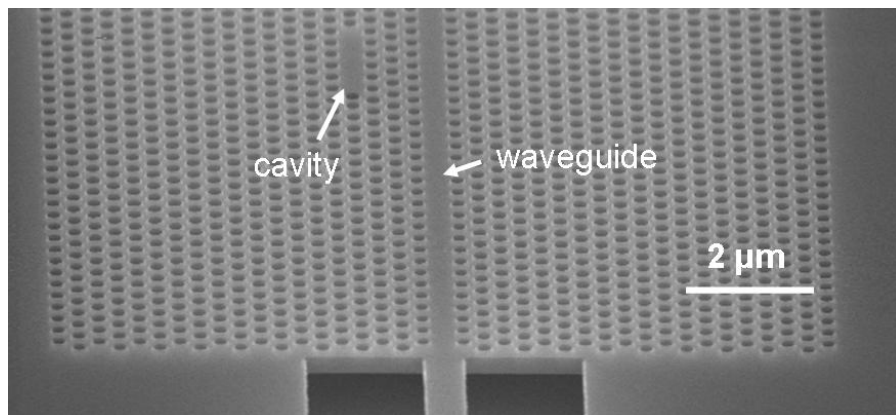


Figure 1.1. Scanning electron microscope (SEM) graph of an example of suspended photonic-crystal slab consisting of air holes. A cavity was created by filling five consecutive air holes. A waveguide was generated by filling a row of air holes.

1.2. ELECTROMAGNETICALLY INDUCED TRANSPARENCY

1.2.1. EIT IN ATOMIC SYSTEMS

Electromagnetically induced transparency (EIT) is an unusual effect that occurs when two laser beams interact within an optical material. The phenomenon happens in atomic systems as a result of the destructive interference between excitation pathways to the excited states in an atom or molecule [5-7]. As originally implemented [5], EIT involves the interaction of laser light with a collection of atoms. It relies on the fact when an incident photon has a ‘resonant’ energy equal to the difference in the energies of two states of an atom, the photon can be absorbed by that atom and its energy is used to excite the ground state electrons into a higher energy state. When two separate laser fields drive two such atomic transitions that share the same higher energy state, destructive interference between the pathways connecting the higher energy state with the lower energy states allows the quantum-mechanical probability that the electron is in the higher energy state to vanish. As there are no electrons in the higher energy state, there has been no absorption of the applied fields. The atom is thereby rendered transparent to the applied laser fields in an extremely narrow frequency range.

The EIT phenomenon can be used to greatly strengthen nonlinear optical effects, such as the dependence of a material’s refractive index on the intensity of the incident light. Examples of profound implication include ultraslow light propagation [8] and coherent control of optical information [9]. Indeed, up to now, most experimental demonstrations of stopping light reply upon the use of EIT by completely or partially transferring the optical information to coherent electronic states [10-12]. However, a

downside of the atomic EIT effect is that it can be implemented only for light in a very small range of frequencies near fixed atomic transitions. The operating wavelength is constrained by the specific wavelength which corresponds to the appropriate atomic transitions. The experimental setup usually requires ultra-high vacuum and very low temperature. Therefore, the use of electronic states to slow and stop light has substantial limits for real applications.

1.2.2. OPTICAL ANALOGUE TO EIT

The EIT interference process has analogies in classical physics, such as plasma [13] and electric circuits [14]. More recently, it was discovered that there is an alternative way of achieving the transmission characteristics of EIT by using small on-chip optical microresonators [15-17]. The origin of the phenomenon is the interference of direct and indirect pathways for two cavities decays. This is the same Fano resonance for optical resonators that has been shown to result in sharp asymmetric line shapes in a narrow frequency range in periodic structures and waveguide-cavity systems [18, 19]. In contrast to the ‘traditional’ EIT in atomic systems where a powerful drive laser is needed, such a resonance is enforced by the geometry of the microresonator structures. The resonators come in various forms such as rings and disks in which the light skims across the outer surface as sound does in a whispering gallery, or less obvious forms such as photonic-crystal cavities which is a point defect in an otherwise perfect crystal. The small size makes them ideal to be used in integrated optics and perform operations on light analogous to those performed by electronic components on silicon chips on electrons. Moreover, the operating wavelength depends on the device structure which is highly

controllable by modern IC fabrication techniques. Recent experimental work has led to demonstrations of the EIT-like optical resonance in microring [20] and photonic-crystal [21, 22] systems.

Like in an atomic EIT system, the narrow transparency peak is associated with large group delay. Theoretical [16] and experimental [23] work in microring systems showed that the EIT-like optical resonance allows simple tuning of the frequency and linewidth. The tuning can be accomplished by changing the temperature [23-25] or injecting free carriers [26, 27], which both changing the refractive index of the materials. The effect in photonic crystal slabs will be shown in more details in Chapter 5. As larger group delay is associated with smaller EIT resonant linewidth, the photonic resonators' EIT system permits controllable delay of the optical signals, a highly desirable functionality for signal processing applications. It is impractical to achieve such a change in atomic vapors because that would require a high intensity for the drive laser. There are additional important advantages of the optical EIT-like resonance over the atomic EIT in applications in optical communications. For example, the cavity's resonance can be designed for a useful wavelength where there are semiconductor laser sources thanks to the flexibility of nanophotonic systems, whereas in atomic systems, the EIT signal depends on the electronic states of an atom, thus is limited to a small number of accessible transition frequencies. The size of the atomic system is dictated not only by the size of the atomic cells, which is on a centimeter scale, but also bulky high power lasers, compared to the microphotonic devices and semiconductor lasers which can be only tens to a few hundreds of microns.

1.2.3. STOPPING LIGHT

By stopping light, we mean controllably trapping and releasing light pulses in localized, standing wave modes. Most of the experimental demonstrations [11, 12, 28] rely upon the use of EIT in atomic vapors under extreme conditions, in which a light pulse is stopped by transferring the optical information to electronic states. Inspired by such works and in view of the advantages of EIT-like optical resonances, namely the tunable bandwidth, the flexible operating wavelength and small sizes, Stanford scientists proposed an innovative method to stop light using coupled resonator systems [29-31].

A wide variety of work has been done on slow-light structures employing coupled resonators. For example, a group velocity as low as $10^{-2}c$ has been experimentally observed at the waveguide band edges [32] or with coupled resonator optical waveguides (CROWs) [33]. However, in all such systems, the maximum achievable time delay scales inversely with the operating bandwidth, which is the delay-bandwidth product limit [34, 35]. Therefore, for a given optical pulse with a certain temporal duration and corresponding frequency bandwidth, the minimum group velocity achievable is fundamentally limited. For this reason, a static photonic structure cannot be used to stop light. As we will see, the use of the dynamic tuning overcomes this constraint by manipulating the photon spectrum in time.

The general condition for stopping light is illustrated in Figure 1.2 [30]. One starts with an initial band structure with sufficiently wide bandwidth to accommodate the incoming light pulse. After the pulse has entered the system, one can then stop the pulse by flattening the dispersion relation adiabatically, while preserving the translational

invariance. In doing so, the spectrum of the pulse is compressed and its group velocity is reduced. The light pulse can be released by reversing the process. Since the translational symmetry is still maintained, the coherent information encoded in the original light pulse is preserved. In this process, the delay is no longer limited by its bandwidth, but is instead entirely controlled by the user of the device.

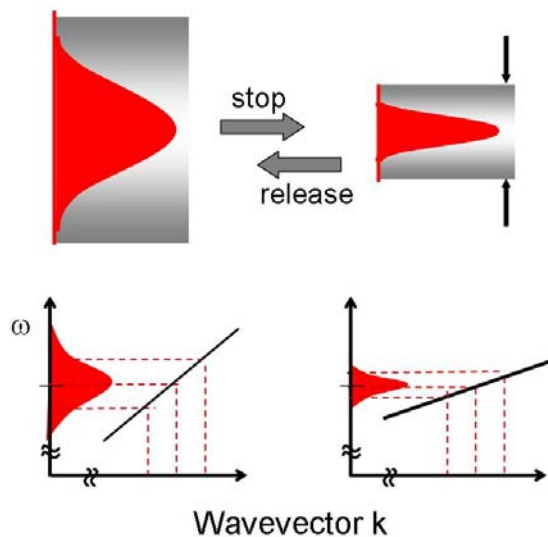


Figure 1.2. The schematics of the general condition for stopping light. (a) The state that the system bandwidth is large in order to accommodate a signal with a given bandwidth. (b) The state that the system bandwidth is compressed and the group velocity is reduced. An adiabatic transition between the two states stops and releases a light pulse. [30]

In order to achieve such dynamic processes, one needs to adjust the properties of the system over time. It can be achieved by modulating the refractive index. However, since the refractive index tuning that can be accomplished is generally quite small, interference schemes need to be devised such that a small refractive index modulation leads to a very large bandwidth change. The EIT-like optical resonance is an excellent platform, which can be realized in a properly designed configuration with two cavities side-coupled to a

waveguide. The transparency linewidth in an EIT-like optical system is highly sensitive to the frequency detuning of the two cavities (Figure 1.3). When the detuning is large, the

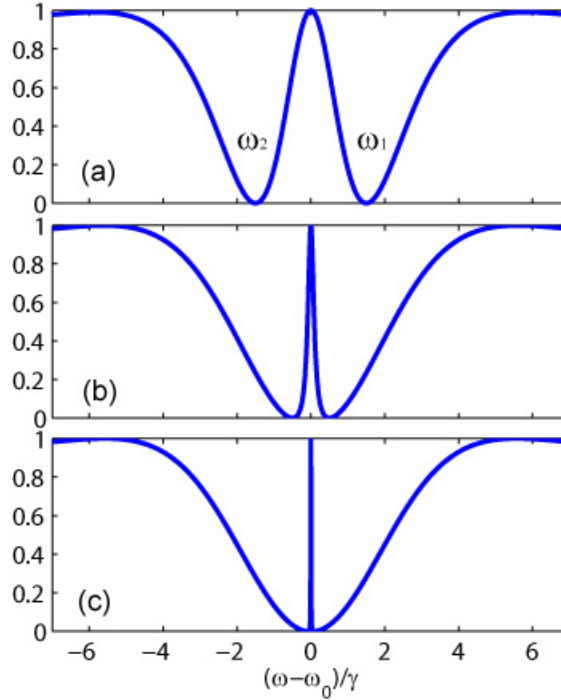


Figure 1.3. Transmission spectrum of a structure with two cavities side-coupled to one waveguide. The linewidth of the central transmission peak is highly sensitive to the frequency detuning of the two cavities. In plotting the curves, we assume two intrinsically lossless resonators with same coupling rate to a waveguide γ . The resonant frequencies are detuned at various numbers $\omega_{1,2} = \omega_0 \pm \Delta\omega/2$. (a) $\Delta\omega = 1.5\gamma$ (b) $\Delta\omega = 0.5\gamma$ (c) $\Delta\omega = 0.1\gamma$. The distance along the waveguide between two resonators is $L = \pi c / \omega_0$ and the waveguide satisfies a dispersion relation $\beta(\omega) = \omega / c$, where c is the speed of light in the waveguide.

transmission spectrum shows two distinct transmission dips each corresponding to the resonance with an individual cavity. When the detuning is small, the transmission spectrum begins to closely resemble that of an atomic EIT system and a transparency peak shows up over a very narrow frequency range. In the absence of intrinsic loss, its

linewidth can be compressed to an arbitrarily small value. In fact, the linewidth of transparency can be infinitesimal, resulting in a resonator with an infinite lifetime.

In this dissertation, I present a design of a photonic crystal slab for an EIT-like all-optical resonance. Both simulated [36] and experimental [22] transmission spectrum exhibits a narrow transparency resonance, which is of great importance in slowing and stopping light. I also show a direct measurement of the group delay directly generated by the EIT-like optical resonance.

1.3. FLAT-TOP REFLECTION FILTER

Compact optical filters are of great interest for optical communication applications as well as sensors. Guided resonances in photonic-crystal slabs provide a very compact way to generate useful spectral functions for externally incident light. So slab-based photonic-crystal filters are very attractive in a wide range of applications since they are very small and capable of implementing multiple functions and suitable for large-scale integration. Generally, photonic-crystal filters, which belong to the class of resonator-type filters, generate a transfer function with a Lorentzian lineshape.

However, a Lorentzian optical response is not always ideal. Sometimes, such as in wavelength-division multiplexing applications, it is important to access the signal on one particular channel without disturbing the signals on the other channels [37-40], so one would rather have a “box-like” optical response. Hence, a flat-top filter, which features a filter response with a flattened resonance and sharp transition from the transmission band to the reflection band (Figure 1.4), is crucial for achieving low crosstalk from other

channels and high robustness against fluctuations in input signal wavelength. In principle, flat-top filters can be approximated by cascading multiple Lorentzian filters [41-43], but this is not easily implemented.

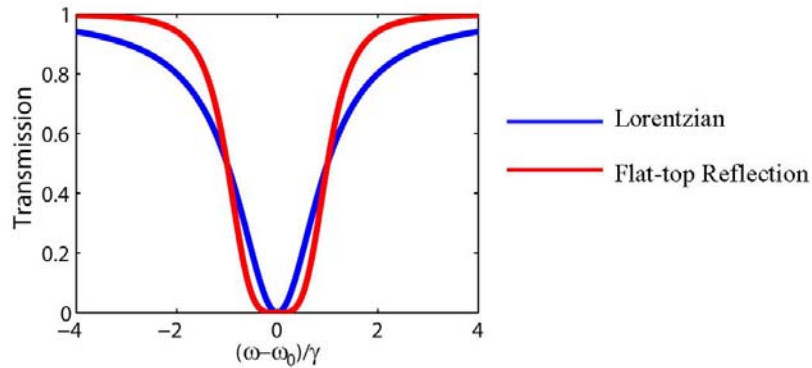


Figure 1.4. Comparison of a Lorentzian (blue curve) and flat-top reflection lineshape. The flat-top reflection optical resonance features a flattened resonance and sharper transition from the reflection band to the transmission band as compared to the Lorentzian lineshape.

In this dissertation, I will show an experimental demonstration of a new configuration of flat-top filter in a photonic-crystal slab. Furthermore, we smoothly change the device behavior from flat-top reflection to EIT-like optical resonance in the same structure [22]. Both types of optical resonances are of great importance in integrated optics, such as slowing and stopping light, as well as wavelength-division multiplexing. By observing both lineshapes in the same device, the results demonstrate greatly enhanced functionality due to the substantial re-configurability enabled by coherent resonant interactions in photonic-crystal structures. In addition to the practical significance, the results are of fundamental importance in physics. While the EIT-like lineshape has an exact atomic physics analogue, the flat-top filter lineshape does not.

Demonstrating the tuning between these two effects thus indicates some of the unique richness in nanophotonics resonance.

1.4. OPTICAL ANALOGUE TO THE SUPERRADIANCE EFFECT

In his classic work in 1954 [44], Dicke pointed out that the description of a spontaneously radiating gas has to include the fact that all atoms or molecules interact with a common radiation field. Consequently, the individual particles may not be considered as independent sources of radiation. The spontaneous emission rate of a coherently radiating ensemble of N two-level atoms can substantially exceed that of N isolated atoms. He referred to these correlated multiple atomic states exhibiting this abnormally large radiation rate as “superradiant states”.

Following Dicke’s original vision, the superradiance effect has been observed using a variety of systems, including atoms [45, 46], ions [47], quantum dots [48, 49], quantum wells [50] and Josephson junctions [51]. Superradiance occurs when different emitters couple to a common mode of light. For photon modes that are three-dimensional in nature, the superradiance effect can only occur between emitters that are placed within about less than a wavelength of each other. All previous experiments are carried out in this regime where the emitters are placed in close proximity to one another.

In this dissertation, I show that an all-optical analogue to the Dicke superradiance effect can be observed in an optical resonator system [52]. This work is along the direction of the recent substantial efforts in mapping the coherent effects in atomic systems to on-chip nanophotonic systems, such as the all-optical analogue to

electromagnetically induced transparency that led to the possibility of stopping light all-optically. The superradiance effect in an optical resonator system enhances waveguide-cavity coupling, essential for low-loss on-chip photonic integration. Moreover, unlike previous work in which the emitters have to be placed within a wavelength of each other, in our experiments the two resonators are separated by a distance much longer than the wavelength. This is enabled by the use of a single-mode tightly confined waveguide, and the specific design that enforces strong waveguide-resonator coupling. As a result, the resonators couple through a restricted one-dimensional photon continuum, which leads to the superradiance effect. In addition, we provide the first experimental demonstration of the structural tuning of the superradiance effect in on-chip silicon optical resonator systems. Our analysis also indicates that the presence of loss, which is inevitable in on-chip resonator systems, in fact facilitates the observation of the superradiance effect.

2. COUPLED-MODE THEORY

Coupled-mode theory is a powerful theoretical framework for analyzing devices composed of multiple components, such as waveguides and cavities. The theory describes a system in terms of a set of idealized and isolated components that are perturbed or coupled in some fashion. To do so, we rely on the weak coupling assumption, which is valid in our devices as Q is over 1000, much larger than π . In such a regime, the modes hardly decay at all over one optical period (i.e. $\tau \gg 2\pi / \omega$). The building blocks in coupled-mode theory are merely localized modes (cavities) and propagating modes (waveguides). As a result, the description is universal for a certain class of devices. Excellent resources in this field are the classic book by Haus [53] which focuses on microwave devices. A generalization to this for a multimode optical resonator is described in reference [17]. In this chapter, I will apply coupled-mode theory to coupled waveguide-cavity systems and predict some properties of these structures that are closely related to the research work in this dissertation.

2.1. SINGLE CAVITY SIDE-COUPLED TO A WAVEGUIDE

We start with the simplest case. Suppose one microcavity is side-coupled to one waveguide, as illustrated in Figure 2.1. Denote a as the overall amplitude (giving both magnitude and phase) of the fields in the microcavity. The unit of a is chosen such that $|a|^2$ is the electromagnetic energy stored in the microcavity. We express the fields in the

waveguide as the sum of incoming and outgoing waveguide modes $S_{m\pm}$ ($m=1,2$). Here, S_{m+} is the amplitude of the mode in left part ($m=1$) or right part ($m=2$) of the waveguide going toward the cavity, and S_{m-} is the amplitude of the mode going away from the cavity. The unit of $S_{m\pm}$ is chosen such that $|S|^2$ is the power flow in the waveguides.

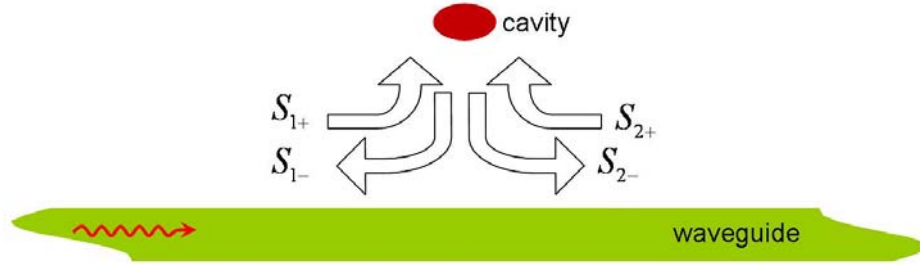


Figure 2.1. Illustration of a structure with one microcavity side-coupled to one waveguide. S_{m+} ($m=1,2$) are amplitudes of the waveguide modes going toward the cavity, and S_{m-} ($m=1,2$) are amplitudes of the waveguide modes going away from the cavity. $S_{1\pm}$ represent of the modes in the left part of the waveguide with respect to the cavity, and $S_{2\pm}$ represent the modes in the right part of the waveguide.

To begin with, we assume a lossless cavity and consider the cavity mode by itself, with no incident power from the waveguides. Due to the weak coupling assumption, the mode will decay exponentially over time with some lifetime, since the rate of energy loss is proportional to the energy stored in the cavity. Then, we include the waveguide. $\gamma_{1,2}$ is the decay rate of the fields in the cavity to the left and the right part of the waveguide respectively. Note that γ in this dissertation is defined as the field decay rate, whereas γ might be defined as the energy decay rate in some other literature. Thus the results would differ by a factor of two. Let K_1 , K_2 , d_1 , d_2 be the coupling constants, representing the

strength of the cavity-waveguide coupling. In coupled-mode theory, the equations governing these quantities in such a system can be written down as

$$\begin{aligned}
\frac{da}{dt} &= (j\omega_0 - \gamma_1 - \gamma_2)a + K_1 S_{1+} + K_2 S_{2+} \\
S_{1-} &= S_{2+} + d_1 a \\
S_{2-} &= S_{1+} + d_2 a.
\end{aligned} \tag{2.1}$$

The constants can be determined by using conservation of energy and time-reversal symmetry, $K_m = d_m = \pm j\sqrt{2\gamma_m}$. In our system, the equality $\gamma_1 = \gamma_2$ is guaranteed by symmetry of the structure. Denote $\gamma_c \equiv \gamma_1 + \gamma_2$ as the coupling loss rate of the cavity to the waveguide, so $K_1 = K_2 = d_1 = d_2 = \pm j\sqrt{\gamma_c}$. The sign, which is related to the phase, is arbitrary and not physically significant. At least, the sign does not change the results of transmission and reflection, which is related to K, d only in the forms of Kd, K^2 and d^2 . With plus sign chosen, Equation (2.1) becomes

$$\begin{aligned}
\frac{da}{dt} &= (j\omega_0 - \gamma_c)a + j\sqrt{\gamma_c} S_{1+} + j\sqrt{\gamma_c} S_{2+} \\
S_{1-} &= S_{2+} + j\sqrt{\gamma_c} a \\
S_{2-} &= S_{1+} + j\sqrt{\gamma_c} a.
\end{aligned} \tag{2.2}$$

Point-defect cavities in photonic-crystal slabs always have radiation loss in the out-of-the-plane direction. Moreover, in experimental devices, other losses, such as fundamental material losses and fabrication imperfections, are inevitable. Even though the origin of these losses may not be the same, they influence the transmission of the cavity-waveguide system in the same manner mathematically. As a result, intrinsic loss is

used to describe the collection of these losses, and corresponding terms must be added appropriately in order to describe such a structure with coupled-mode theory. Since the intrinsic loss is small, as required by the weak-coupling assumption, the effect of the intrinsic loss rate, γ_i , on other coupling constants is second-order and can be neglected. Therefore, it is appropriate to simply add γ_i to (2.2) even though the intrinsic loss technically breaks conservation of energy and time-reversal symmetry:

$$\begin{aligned}\frac{da}{dt} &= (j\omega_0 - \gamma_c - \gamma_i)a + j\sqrt{\gamma_c}S_{1+} + j\sqrt{\gamma_c}S_{2+} \\ S_{1-} &= S_{2+} + j\sqrt{\gamma_c}a \\ S_{2-} &= S_{1+} + j\sqrt{\gamma_c}a.\end{aligned}\tag{2.3}$$

Since frequency is conserved in a linear system, one can solve Equation (2.3) by considering the steady state sinusoidal waves $a \sim a_0 e^{j\omega t}$, $S_{1+} \sim S_{1+}^0 e^{j\omega t}$ and $S_{2+} = 0$:

$$\begin{aligned}a_0 &= \frac{j\sqrt{\gamma_c}}{j(\omega - \omega_0) + (\gamma_c + \gamma_i)} S_{1+}^0 \\ S_{1-}^0 &= j\sqrt{\gamma_c}a_0 = \frac{-\gamma_c}{j(\omega - \omega_0) + (\gamma_c + \gamma_i)} S_{1+}^0 \\ S_{2-}^0 &= S_{1+} + j\sqrt{\gamma_c}a_0 = \frac{\gamma_i + j(\omega - \omega_0)}{j(\omega - \omega_0) + (\gamma_c + \gamma_i)} S_{1+}^0.\end{aligned}\tag{2.4}$$

The reflection r and transmission t in amplitude follow:

$$\begin{aligned}r &\equiv \frac{S_{1-}}{S_{1+}} = \frac{-\gamma_c}{j(\omega - \omega_0) + (\gamma_c + \gamma_i)} \\ t &\equiv \frac{S_{2-}}{S_{1+}} = \frac{j(\omega - \omega_0) + \gamma_i}{j(\omega - \omega_0) + (\gamma_c + \gamma_i)}.\end{aligned}\tag{2.5}$$

The reflection and transmission coefficients in power are the square of the modulus of the corresponding complex numbers:

$$\begin{aligned} |r|^2 &= \frac{\gamma_c^2}{(\omega - \omega_0)^2 + (\gamma_c + \gamma_i)^2} \\ |t|^2 &= \frac{(\omega - \omega_0)^2 + \gamma_i^2}{(\omega - \omega_0)^2 + (\gamma_c + \gamma_i)^2}. \end{aligned} \quad (2.6)$$

They both have a Lorentzian lineshape. Note that they do not add up to unity when the cavity is intrinsically lossy, i.e. $\gamma_i \neq 0$. We define a dimensionless quality factor $Q \equiv \omega_0 / 2\gamma$. And the total decay rate $\gamma_{total} = \gamma_c + \gamma_i$ corresponds to a total quality factor $1/Q_{total} = 1/Q_c + 1/Q_i$. By replacing γ with its corresponding Q , (2.6) can be written as

$$\begin{aligned} |r|^2 &= \frac{\left(\frac{1}{2Q_c}\right)^2}{\left(\frac{\omega - \omega_0}{\omega_0}\right)^2 + \left(\frac{1}{2Q_{total}}\right)^2} \\ |t|^2 &= \frac{\left(\frac{\omega - \omega_0}{\omega_0}\right)^2 + \left(\frac{1}{2Q_i}\right)^2}{\left(\frac{\omega - \omega_0}{\omega_0}\right)^2 + \left(\frac{1}{2Q_{total}}\right)^2}. \end{aligned} \quad (2.7)$$

Two quantities in the Lorentzian lineshape, directly following (2.7), will be frequently used in analyzing experimental results: 1) fractional linewidth ($\Delta\omega / \omega$) at half-maximum of a Lorentzian peak equals $1/Q_{total}$, and 2) transmittance, defined as the ratio of the transmitting energy in the presence of the cavity to the energy in the absence of the cavity, equals $(Q_{total} / Q_i)^2$. These two properties of a Lorentzian allow us to determine Q 's from the transmission spectrum. In our devices particularly, waveguide-

cavity coupling is much stronger than cavity intrinsic loss, so $Q_i \gg Q_c$ and $Q_{total} \approx Q_c$. The fractional linewidth thus approximately equals $1/Q_c$, and the transmittance approximately equals $(Q_c / Q_i)^2$.

2.2. TWO CAVITIES SIDE-COUPLED TO A WAVEGUIDE

We now add a second cavity to the system and consider the case of two cavities side-coupled to one waveguide. One could definitely derive the equations for such a system in the same fashion as in the previous section. In this section, however, I will use the Fabry-Perot analysis and the results of a single cavity to obtain the transmission equation. I first show the general formula, and then discuss two special cases to illustrate the concept that are closely related to the experimental work.

2.2.1. GENERAL THEORETICAL CALCULATION

Suppose two cavities are placed far apart and there is no direct coupling between them, as illustrated in Figure 2.2. The setup can be viewed as a Fabry-Perot system with two mirrors, each with a Lorentzian-type response. We denote the “round-trip” gain as

$$g = r_A r_B e^{-\alpha 2L - j\beta 2L}, \quad (2.8)$$

where $r_{A,B}$ is the reflection coefficient for resonator A or B shown in Equation (2.5), α is the waveguide loss/gain coefficient, β is the waveguide wave vector, and L is the spacing of the two resonators.

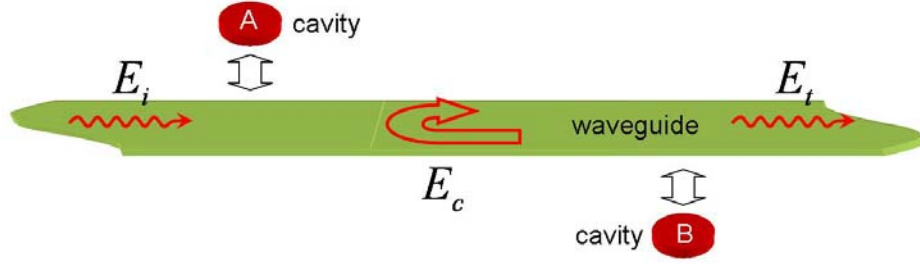


Figure 2.2. Illustration of a structure with two cavities side-coupled to one waveguide. E_i is the incident fields, E_c is the circulation fields in the waveguide between the cavities, and E_t is the transmitted fields.

The circulation fields (E_c) and the incident fields (E_i) have the following relation:

$$E_c = t_A E_i + g E_c, \quad (2.9)$$

where t_A is the transmission coefficient for resonator A (2.5) and g is defined in (2.8).

Rearrange (2.9) and consider (2.8), so

$$\begin{aligned} \frac{E_c}{E_i} &= \frac{t_A}{1 - g} \\ &= \frac{t_A}{1 - r_A r_B e^{-\alpha 2L - j\beta 2L}}. \end{aligned} \quad (2.10)$$

We subsequently relate the transmitted fields (E_t) and the circulating fields (E_c),

$$E_t = t_B e^{-\alpha - j\beta L} E_c. \quad (2.11)$$

From (2.10) and (2.11), by neglecting the waveguide gain/loss ($\alpha \approx 0$), we obtain the transmission for the system in Figure 2.2:

$$T = \frac{E_t}{E_i} = \frac{t_A t_B e^{-j\beta L}}{1 - r_A r_B e^{-j2\beta L}}. \quad (2.12)$$

Equation (2.12) can be reorganized to obtain the magnitude and phase of the transmission.

Let $r_A r_B e^{-2j\beta L} = r e^{2j\theta_1}$, where

$$\begin{aligned} r &= |r_A r_B| \\ &= \frac{\gamma_A^c \gamma_B^c}{\sqrt{(\omega - \omega_A)^2 + (\gamma_A^c + \gamma_A^i)} \sqrt{(\omega - \omega_B)^2 + (\gamma_B^c + \gamma_B^i)}} \end{aligned} \quad (2.13)$$

$$\begin{aligned} 2\theta_1 &= \text{Arg}(r_A) + \text{Arg}(r_B) - 2\beta L \\ &= \pi - \tan^{-1}\left[\frac{\omega - \omega_A}{\gamma_A^c + \gamma_A^i}\right] + \pi - \tan^{-1}\left[\frac{\omega - \omega_B}{\gamma_B^c + \gamma_B^i}\right] - 2\beta L. \end{aligned} \quad (2.14)$$

Similarly, let $t_A t_B e^{-j\beta L} = t e^{j\theta_2}$, where

$$t = \frac{\sqrt{((\omega - \omega_A)^2 + \gamma_A^{i2})(\omega - \omega_B)^2 + \gamma_B^{i2}}}{\sqrt{(\omega - \omega_A)^2 + (\gamma_A^c + \gamma_A^i)} \sqrt{(\omega - \omega_B)^2 + (\gamma_B^c + \gamma_B^i)}} \quad (2.15)$$

and

$$\begin{aligned} \theta_2 &= \text{Arg}(t_A) + \text{Arg}(t_B) - \beta L \\ &= \tan^{-1}\left[\frac{\omega - \omega_A}{\gamma_A^i}\right] - \tan^{-1}\left[\frac{\omega - \omega_A}{\gamma_A^i + \gamma_A^c}\right] + \tan^{-1}\left[\frac{\omega - \omega_B}{\gamma_B^i}\right] - \tan^{-1}\left[\frac{\omega - \omega_B}{\gamma_B^i + \gamma_B^c}\right] - \beta L. \end{aligned} \quad (2.16)$$

With (2.13) - (2.16), (2.12) can be rewritten in a form which illustrates the underlying physics more explicitly:

$$\begin{aligned}
T &= \frac{te^{j\theta_2}}{1-re^{j2\theta_1}} \\
&= \frac{te^{j\theta_2}e^{-j\theta_1}}{\sqrt{r}\left(\frac{1}{\sqrt{r}}e^{-j\theta_1}-\sqrt{r}e^{j\theta_1}\right)} \\
&= \frac{te^{j\theta_2}e^{-j\theta_1}}{\sqrt{r}\left[\left(\frac{1}{\sqrt{r}}-\sqrt{r}\right)\cos\theta_1-j\left(\frac{1}{\sqrt{r}}+\sqrt{r}\right)\sin\theta_1\right]} \\
&= \frac{te^{j\theta_2}e^{-j\theta_1}}{(1-r)\cos\theta_1-j(1+r)\sin\theta_1} \\
&= \frac{te^{j\theta_2}e^{-j\theta_1}\left((1-r)\cos\theta_1+j(1+r)\sin\theta_1\right)}{(1-r)^2\cos^2\theta_1+(1+r)^2\sin^2\theta_1} \\
&= \frac{te^{j\theta_2}e^{-j\theta_1}\sqrt{(1-r)^2\cos^2\theta_1+(1+r)^2\sin^2\theta_1}e^{j\tan^{-1}\left[\frac{1+r}{1-r}\tan\theta_1\right]}}{(1-r)^2\cos^2\theta_1+(1+r)^2\sin^2\theta_1} \\
&= \frac{t}{\sqrt{(1-r)^2\cos^2\theta_1+(1+r)^2\sin^2\theta_1}}e^{j\theta_2}e^{-j\theta_1}e^{j\tan^{-1}\left[\frac{1+r}{1-r}\tan\theta_1\right]} \\
&= \frac{t}{\sqrt{(1-r)^2+[(1-r)^2-(1+r)^2]\sin^2\theta_1}}e^{j\theta_2}e^{-j\theta_1}e^{j\tan^{-1}\left[\frac{1+r}{1-r}\tan\theta_1\right]} \\
&= \frac{t}{\sqrt{(1-r)^2+4r\sin^2\theta_1}}e^{j\theta_2}e^{-j\theta_1}e^{j\tan^{-1}\left[\frac{1+r}{1-r}\tan\theta_1\right]} \\
&= \frac{t}{(1-r)\sqrt{1+4\left(\frac{\sqrt{r}}{1-r}\right)^2\sin^2\theta_1}}e^{j\theta_2}e^{-j\theta_1}e^{j\tan^{-1}\left[\frac{1+r}{1-r}\tan\theta_1\right]} . \tag{2.17}
\end{aligned}$$

Consequently, the transmission coefficient in power from the two-cavity system is

$$\begin{aligned}
|T|^2 &= \frac{t^2}{(1-r)^2} \frac{1}{1+4\left(\frac{\sqrt{r}}{1-r}\right)^2\sin^2\theta_1} \\
&= \frac{|t_A t_B|^2}{(1-|r_A r_B|)^2} \frac{1}{1+4\left(\frac{\sqrt{|r_A r_B|}}{1-|r_A r_B|}\right)^2\sin^2\theta_1}, \tag{2.18}
\end{aligned}$$

and the phase from the transmission amplitude is the argument of the complex number in (2.17)

$$\theta_t = \theta_2 - \theta_1 + \tan^{-1}\left[\frac{1+r}{1-r} \tan \theta_1\right]. \quad (2.19)$$

In order to understand (2.19), we first consider a case that the cavity resonances are far-detuned from each other, so $|\omega_A - \omega_B|$ is large. From the expression of r in (2.13), obviously $r \approx 0$ as $(\omega - \omega_A)$ and $(\omega - \omega_B)$ cannot both be small. The last two terms in (2.19) cancel out and the equation becomes $\theta_t \approx \theta_2$. Recall from (2.16) that θ_2 is the phase accumulated from the transmission of both resonators and the propagation in the waveguide between the two resonators. In this case, the two resonators behave independently (i.e. no Fabry-Perot resonance). Consequently, we denote the phase from the Fabry-Perot resonance as the interference phase θ_i :

$$\theta_i \equiv -\theta_1 + \tan^{-1}\left[\frac{1+r}{1-r} \tan \theta_1\right]. \quad (2.20)$$

2.2.2. THE PROPAGATION PHASE

As one of the conclusions in Section 2.2.1, the waveguide-microcavity system in Figure 2.2 has the normalized transmission spectrum

$$|T(\omega)|^2 = \frac{|t_A(\omega)t_B(\omega)|^2}{(1 - |r_A(\omega)r_B(\omega)|)^2} \frac{1}{1 + 4\left(\frac{\sqrt{|r_A(\omega)r_B(\omega)|}}{1 - |r_A(\omega)r_B(\omega)|}\right)^2 \sin^2 \frac{\Phi(\omega)}{2}}, \quad (2.21)$$

where $t_{A,B}(\omega)$ and $r_{A,B}(\omega)$ are the amplitude of the transmission and reflection coefficients for resonators A and B, respectively:

$$t_{A,B}(\omega) = \frac{j(\omega - \omega_{A,B}) + \gamma_{A,B}^i}{j(\omega - \omega_{A,B}) + (\gamma_{A,B}^c + \gamma_{A,B}^i)} \quad (2.22)$$

$$r_{A,B}(\omega) = \frac{-\gamma_{A,B}^c}{j(\omega - \omega_{A,B}) + (\gamma_{A,B}^c + \gamma_{A,B}^i)}. \quad (2.23)$$

Here, $\omega_{A,B}$ is the resonant frequency of the resonator A or B, $\gamma_{A,B}^i$ is intrinsic-loss rate, $\gamma_{A,B}^c$ is the waveguide-cavity coupling-loss rate, $\Phi(\omega)$ (equal to $2\theta_1$ in (2.14)) is the total phase accumulated as light goes through a round trip by reflection from both microcavities and propagation in the waveguide. Mathematically, $\Phi(\omega) = \phi_A(\omega) + \phi_B(\omega) + \phi_{\text{wg}}(\omega)$, where $\phi_{A,B}(\omega)$ are the phase associated with the reflection by the coupled microcavity A or B: $\phi_{A,B}(\omega) = \text{Arg}[r_{A,B}(\omega)]$, and $\phi_{\text{wg}}(\omega)$ is the round-trip propagation phase in the waveguide: $\phi_{\text{wg}}(\omega) = -2\beta(\omega)L$, where $\beta(\omega)$ is the waveguide dispersion relation and L is the spacing between the cavities.

While the one-cavity system shown in Figure 2.1 invariantly generates a Lorentzian optical resonance, the two-cavity system in Figure 2.2 exhibits various lineshapes of transmission spectra depending on the resonant frequency detuning between the two cavities and the propagation phase in the waveguide. In Figure 1.3, we have seen the influence of the frequency detuning on the linewidth of the middle transmission peak.

The change of the propagation phase in the waveguide actually also drastically alters the transmission lineshape.

For simplicity, we assume two intrinsically lossless resonators with the same coupling rate to a waveguide: $\gamma_{A,B}^i = 0$, $\gamma_{A,B}^c = \gamma$. Coherent interaction between the two resonators occurs only when the two resonators have similar resonant frequencies. In such a case, the transmission lineshape depends strongly on the propagation phase ϕ_{wg} in the waveguide. As an illustration, we consider the case of $\omega_{A,B} = \omega_0 \pm \delta\omega/2$, and the reflection phases from the two resonators cancel at ω_0 . When $\phi_{\text{wg}}(\omega_0) = 2n\pi$, the system is therefore on resonance at ω_0 , resulting in a transparency resonance peak at ω_0 in Figure 2.3(a). This transparency peak is a direct consequence of the constructive interference between multiple reflecting waves. The system exhibits an optical analogue to electromagnetically induced transparency (EIT). When $\phi_{\text{wg}}(\omega_0) = (2n+1)\pi$, the transparency resonance condition is no longer satisfied. So the transparency resonance peak disappears. The structure instead behaves as a flat-top reflection filter in Figure 2.3(b), which features a flattened resonance and a much sharper transition between transmission and reflection compared with the single-resonance Lorentzian lineshape. In plotting Figure 2.3, we assume a linear waveguide dispersion relation since we are only interested in the narrow frequency range in the vicinity of the cavity resonance.

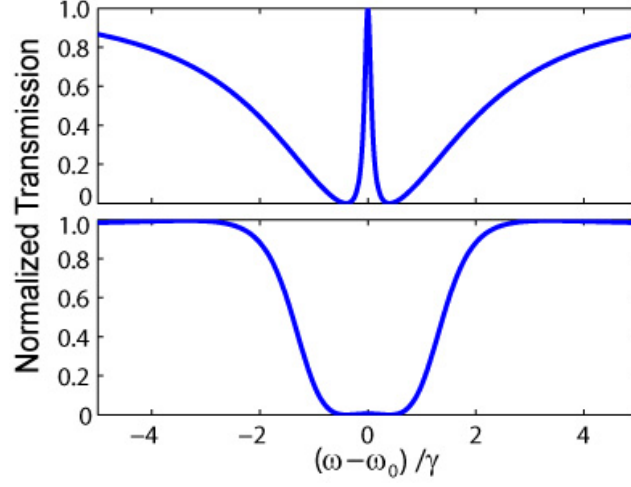


Figure 2.3. Graphical illustration of the transmission spectra computed with coupled-mode theory. In plotting the curves, we assume two intrinsically lossless resonators with the same coupling rate to a waveguide: $\gamma_{A,B}^i = 0$, $\gamma_{A,B}^c = \gamma$. The resonance frequencies are detuned at an arbitrary small number, $\omega_{A,B} = \omega_0 \pm \frac{\delta\omega}{2}$, and here we let $\delta\omega = 0.8\gamma$. We also assume that the waveguide has a linear dispersion relation $\phi_{\text{wg}}(\omega) = -0.2 \frac{\omega - \omega_0}{\gamma} + \hat{\phi}$. (a) EIT-like transmission spectrum when $\phi_{\text{wg}}(\omega_0) = 2n\pi$. (b) Flat-top reflection filter when $\phi_{\text{wg}}(\omega_0) = (2n + 1)\pi$.

Both EIT-like and flat-top reflection filter lineshapes are of substantial importance. EIT-like optical resonance renders an integrated optical system transparent at an otherwise highly reflective wavelength. As discussed in Chapter 1, the potential for slowing [35], stopping [31] and time-reversing [54] of light pulses on chip in such a system has profound impact for both fundamental science and applications in optical communication. Flat-top band-reflection filters, which reflect a narrow range of wavelengths while other wavelengths pass through, are essential in achieving low inter-channel crosstalk in wavelength-division multiplexing (WDM) and robustness against fluctuations in input-signal wavelength in communication applications [37, 38].

The Flat-top filter is a higher-order filter compared to the Lorentzian filter. To see that, for the simplicity of mathematics, we further assume $\delta\omega \rightarrow 0$. Directly from Equation (2.12) and considering (2.22) and (2.23)

$$\begin{aligned}
|T|^2 &\rightarrow \frac{|t|^4}{|1+r^2|^2} \\
&= \frac{(\omega - \omega_A)^2(\omega - \omega_B)^2 / [(\omega - \omega_A)^2 + \gamma^2][(\omega - \omega_B)^2 + \gamma^2]}{\{[-(\omega - \omega_A)(\omega - \omega_B) + 2\gamma^2]^2 + \gamma^2[(\omega - \omega_A) + (\omega - \omega_B)]^2\} / [(\omega - \omega_A)^2 + \gamma^2][(\omega - \omega_B)^2 + \gamma^2]} \\
&= \frac{(\omega - \omega_A)^2(\omega - \omega_B)^2}{(\omega - \omega_A)^2(\omega - \omega_B)^2 + \gamma^2[(\omega - \omega_A) + (\omega - \omega_B)]^2 + 4\gamma^4 - 4\gamma^2(\omega - \omega_A)(\omega - \omega_B)} \\
&\rightarrow \frac{(\omega - \omega_0)^4}{(\omega - \omega_0)^4 + 4\gamma^2(\omega - \omega_0)^2 + 4\gamma^4 - 4\gamma^2(\omega - \omega_0)^2} \\
&= \frac{(\omega - \omega_0)^4}{(\omega - \omega_0)^4 + 4\gamma^4}.
\end{aligned} \tag{2.24}$$

The transmission spectrum (2.24) has a form very similar to the Lorentzian (e.g. (2.6) and $\gamma_i = 0$) except terms raised to the fourth power rather than squared.

2.2.3. OPTICAL ANALOGUE TO THE SUPERRADIANCE EFFECT

As shown in Chapter 1, the superradiance effect is an effect that coherent interactions between multiple emitters enhance their spontaneous emission rate. In a photonic waveguide-resonator system, however, the origin of the superradiance effect is purely classical and can also be understood by considering the system in Figure 2.2 and the transmission spectrum in (2.12). Again, we are interested in the case of $\omega_{A,B} = \omega_0 \pm \frac{\delta\omega}{2}$ and $\delta\omega \rightarrow 0$, as coherent interactions between the two resonators occur only when the two resonators have similar resonant frequencies. If the spacing of the two

cavities L and waveguide dispersion relation $\beta(\omega)$ are chosen such that $\phi_{\text{wg}}(\omega_0) = 2n\pi$, the transmission spectrum becomes

$$\begin{aligned}
|T|^2 &\rightarrow \frac{|t|^4}{|1-r^2|^2} \\
&= \frac{((\omega - \omega_0)^2 + \gamma_i^2)^2}{((\omega - \omega_0)^2 + (\gamma_c + \gamma_i)^2)^2} \\
&= \frac{[-(\omega - \omega_0)^2 + \gamma_i(\gamma_i + 2\gamma_c)]^2 + 4(\omega - \omega_0)^2(\gamma_c + \gamma_i)^2}{[-(\omega - \omega_0)^2 + (\gamma_c + \gamma_i)^2]^2 + 4(\omega - \omega_0)^2(\gamma_c + \gamma_i)^2} \\
&= \frac{((\omega - \omega_0)^2 + \gamma_i^2)^2 / ((\omega - \omega_0)^2 + (\gamma_c + \gamma_i)^2)^2}{\{[-(\omega - \omega_0)^2 + \gamma_i(\gamma_i + 2\gamma_c)]^2 + 4(\omega - \omega_0)^2(\gamma_c + \gamma_i)^2\} / ((\omega - \omega_0)^2 + (\gamma_c + \gamma_i)^2)^2} \\
&= \frac{((\omega - \omega_0)^2 + \gamma_i^2)^2}{[-(\omega - \omega_0)^2 + \gamma_i(\gamma_i + 2\gamma_c)]^2 + 4(\omega - \omega_0)^2(\gamma_c + \gamma_i)^2} \\
&= \frac{((\omega - \omega_0)^2 + \gamma_i^2)^2}{(\omega - \omega_0)^4 + (2\gamma_i^2 + 4\gamma_i\gamma_c + 4\gamma_c^2)(\omega - \omega_0)^2 + \gamma_i^2(\gamma_i + 2\gamma_c)^2} \\
&= \frac{((\omega - \omega_0)^2 + \gamma_i^2)^2}{((\omega - \omega_0)^2 + \gamma_i^2)((\omega - \omega_0)^2 + (\gamma_i + 2\gamma_c)^2)} \\
&= \frac{(\omega - \omega_0)^2 + \gamma_i^2}{(\omega - \omega_0)^2 + (\gamma_i + 2\gamma_c)^2} \\
&= |t_{\omega_0, \gamma_i, 2\gamma_c}(\omega)|^2.
\end{aligned} \tag{2.25}$$

Equation (2.25) has the form of a Lorentzian with the coupling-loss rate increased by a factor of two compared to Equation (2.6), indicating a twofold enhancement of the waveguide-cavity coupling as a result of the superradiance effect.

Recall that the condition for EIT-like optical resonance is also $\phi_{\text{wg}}(\omega_0) = 2n\pi$. The EIT-like lineshape can be viewed as the superposition of two modes: subradiance mode associated with a transparency peak with tiny linewidth, and superradiance mode

associated with a transmission dip with large linewidth (Figure 1.3). In the absence of cavity intrinsic loss, the linewidth of the transparency peak can be arbitrarily narrow (Figure 1.3(c)) [16]. For a subradiance mode with infinitesimal linewidth, the cavities are decoupled from the waveguide so photons are trapped in the coupled cavity system indefinitely. In the presence of intrinsic loss, however, photons through a system with finite lifetime are no longer transmitted with 100% transmission (Figure 2.4 (a)(b)), and photons through a system with infinite lifetime are no longer transmitted at all (Figure 2.4 (c)). Thus, the subradiance mode is suppressed when the frequency detuning is small enough ($|\omega_A - \omega_B| \ll \gamma$). The presence of intrinsic loss, which is inevitable in on-chip resonator systems, in fact facilitates the observation of the pure superradiance effect. The system exhibits only the superradiance mode with a Lorentzian-shaped transmission spectrum, whose linewidth is roughly twice as large as that of the Lorentzian generated by a single cavity (Figure 2.4 (c)). As mentioned in Section 2.1, the full width at half maximum is proportional to γ_{total} or $1/Q_{total}$. In our devices, $Q_i \gg Q_c$, so $Q_{total} \approx Q_c$, and the stronger the coupling, the larger the linewidth. The widened linewidth in the superradiance mode graphically indicates the enhanced waveguide-cavity coupling.

In view of the symmetry in the two-cavity setup, the system supports two modes, symmetric and anti-symmetric modes. When the round-trip propagation phase is a multiple of 2π , there are two possibilities, an odd or even multiple of 2π . If $\phi_{wg}(\omega_0)$ is an odd multiple of 2π , the anti-symmetric mode is the superradiance mode since the radiation amplitudes into the waveguide from the two resonators constructively interfere, and the symmetric mode is the subradiance mode since destructive interference occurs.

Oppositely, if $\phi_{\text{wg}}(\omega_0)$ is an even multiple of 2π , the symmetric mode is the superradiance mode and the anti-symmetric mode the subradiance mode.

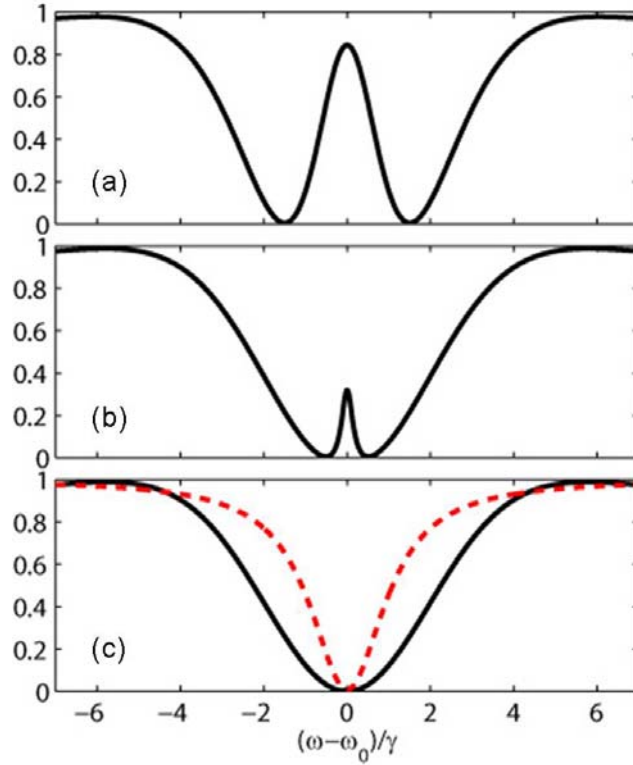


Figure 2.4. Transmission spectra (black curves) of the two intrinsically lossy cavities side-coupled to one waveguide. This configuration is directly compared to Figure 1.3 in which cavities are intrinsically lossless. In plotting the curves, we assume waveguide-cavity coupling rate γ_c equals γ and cavity intrinsic loss rate $\gamma_i = \gamma/10$. The resonant frequencies are detuned at various numbers $\omega_{1,2} = \omega_0 \pm \Delta\omega/2$. (a) $\Delta\omega = 1.5\gamma$ (b) $\Delta\omega = 0.5\gamma$ (c) $\Delta\omega = 0.1\gamma$. The distance along the waveguide between two resonators is $L = \pi c / \omega_0$ and the waveguide satisfies a dispersion relation $\beta(\omega) = \omega / c$, where c is the speed of light in the waveguide. As a reference, the red dashed curve is the Lorentzian-shaped transmission dip generated by a single cavity.

It can be shown that the superradiance effect can also be observed for a system similar to that in Figure 2.2, but with N resonators side coupled to a waveguide, provided that each resonator is intrinsically lossless and separated from its neighboring

resonators by a distance L such that $\phi_{\text{wg}}(\omega_0)$ is a multiple of 2π . In such a system, the transmission has the form of a single Lorentzian dip with width $N\gamma_c$, indicating a N times enhancement of the resonator-waveguide coupling rate due to the superradiance effect [24].

3. STRUCTURE DESIGN

Inspired by the preceding theoretical analysis, we designed photonic-crystal devices to enforce the coherent interactions and facilitate the phase and resonant frequency tuning.

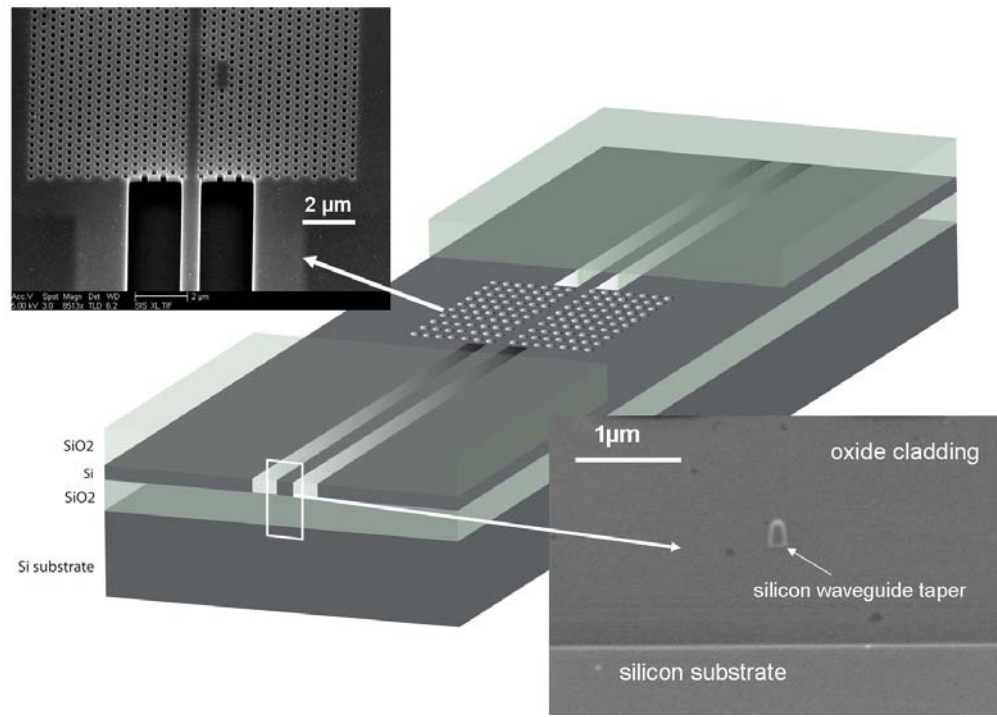


Figure 3.1. Schematic of the device structure. The photonic crystal is etched into a suspended silicon membrane. The input and output strip waveguides, which are surrounded by oxide claddings, are coupled to the photonic-crystal waveguide. The strip waveguides are tapered at the coupling facet to reduce back-reflections. Top insert: SEM of the interface between the photonic-crystal waveguide and the strip waveguide. Bottom insert: SEM of the cross section of the inverse taper.

The device consists of a suspended photonic slab and oxide-clad strip waveguides. Figure 3.1 shows a schematic of the device structure and SEM graphs of fabricated devices. In this chapter, I will discuss the design of various parts in the device, including the

photonic-crystal membrane, the strip waveguides and the layouts of the devices in the wafer as well.

3.1. PHOTONIC-CRYSTAL SLAB

The photonic-crystal slab is the key structure to enforce the coherent interactions. It is built in an air-bridged suspended membrane to maximize the contrast of the refractive indices between the silicon slab and the surroundings, and thus increase the confinement by index guiding. Moreover, the floated structures have $z = 0$ reflection symmetry. Placing the slab on a substrate will break the reflection symmetry, causing the TE-like and TM-like modes to couple. As a result, when a slab is placed on a substrate, the modes in the waveguide and cavities that were otherwise confined by the gap become leaky.

Even though photonic crystals can be made in any dielectric materials, silicon based photonic crystals are highly desirable. First, the index between silicon and air is quite large. Second, fabrication techniques in silicon have been incredibly well developed in the past six decades by the semiconductor industry. Finally, silicon photonic devices are intrinsically compatible with silicon based integrated circuits and there will thus be little barrier to integration in the future.

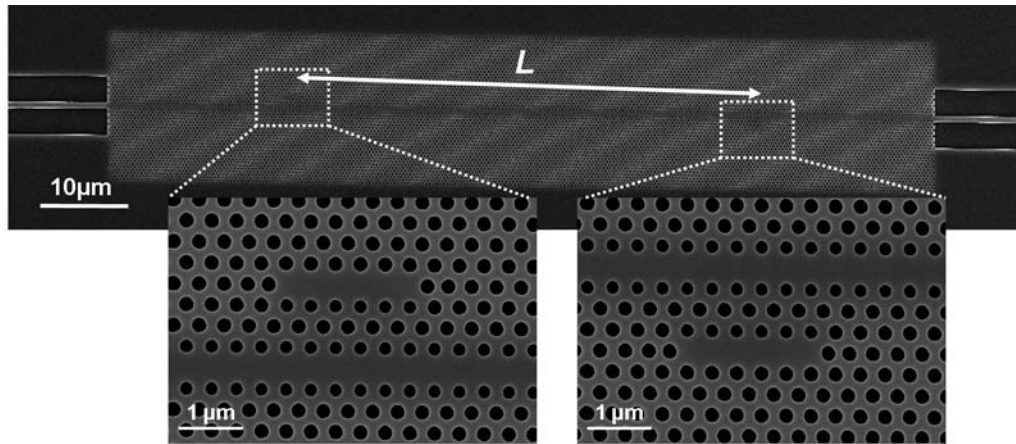


Figure 3.2. SEM graph of a fabricated photonic-crystal slab. The photonic crystal is formed by air holes in a triangular lattice in a silicon slab. The line defect, missing one row of air holes, is a waveguide. The point defect, missing five consecutive holes, is a cavity. The two cavities are separated by a distance L . Inserts: magnified view of the cavities and part of the waveguide.

We designed a photonic-crystal slab made of a triangular lattice of air holes with the lattice constant $a = 386\text{nm}$ and a hole radius of 116nm (Figure 3.2). The slab has a height of 320 nm and possesses a band gap for TE modes (magnetic field parallel to the hole axis). A single-mode photonic-crystal waveguide is generated by filling (i.e. not etching) one row of air holes with silicon. Each resonator is created by filling a row of five consecutive holes parallel to the waveguide. Since it is desirable to have a high ratio of intrinsic Q to coupling Q , there are some fine structures around the cavities and the waveguide. The nearest holes on both sides of the resonator are shifted outward by 77 nm to optimize the electric field distribution in the cavity. By breaking the periodicity at the first side holes and letting the electric field extend farther beyond the cavity, the field envelope follows a Gaussian profile more closely. It has been shown to significantly improve the confinement by index guiding, and thus increase the radiation Q of the cavity [55]. The waveguide-resonator coupling occurs through a barrier of three rows of holes.

Between the resonator and the waveguide, the radii of the six holes along the side of the resonator and the rows of holes along the side of the waveguide were reduced to 102nm. This adjustment moves the resonant frequency of the resonator closer to the band edge, where the waveguide has a flatter dispersion relation. This enhances waveguide-cavity coupling, and further increases the intrinsic quality factor [56, 57].

The two resonators are separated by a distance of 140 lattice constants, or 54.04 μm in the horizontal direction (L in Figure 3.2). The spacing is chosen such that the propagation phase between the two resonators is close to a multiple of 2π to enforce the transparency resonance. On one hand, it has to be large enough to provide sufficient room for the laser-pumped thermal tuning on the waveguide without significantly affecting the resonators. On the other hand, it must not be unnecessarily large. Reflections at two resonators produce Fabry-Perot resonances. Its oscillation periodicity, $\Delta\omega$, in the transmission spectrum is inversely proportionally to L with a relation $\Delta\omega/2\pi \approx v_g/2L$. As a result, L has to be maintained small enough so that the oscillation frequency is greater than the linewidth of the cavity resonant dip. In addition, smaller L makes the photonic crystal small, a desirable feature in the time-consuming procedure of electron-beam lithography.

The transmission spectrum of a photonic-crystal system, designed to demonstrate the EIT-like optical resonance, was obtained by using finite-difference time-domain (FDTD) simulation [58] performed by Sunil Sandhu in Professor Shanhui Fan's group. The computational cell was truncated by uniaxial perfectly matched boundary layers. The

transmission spectrum of the system is shown in Figure 3.3. The central peak has a full-width half-maximum of $2.5 \times 10^{-6} \times 2\pi c/a$ corresponding to a Q of 100,700. Note the asymmetric lineshape in Figure 3.3, which is due to the fact that the phase is close but not exactly equal to 2π . In design and simulation, the phase was controlled solely by the distance of the cavity separation, which can only be a multiple of the lattice constant. Since this adjustment was discrete, it was thus difficult to create an exact 2π propagation phase in the waveguide between the two cavities. Whereas in our experimental work, which I will show in Chapter 6, laser pumped thermal tuning was used to control the refractive index of the waveguide thus smoothly tune the waveguide dispersion. By varying the laser power, the phase could be changed continuously to 2π , resulting in a symmetric lineshape.

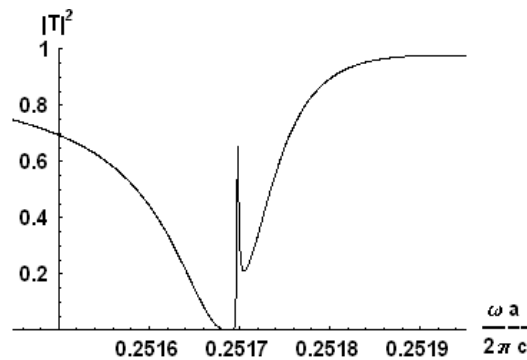


Figure 3.3. Transmission spectrum of a photonic-crystal structure calculated with FDTD simulation. The two-cavity structure gives rise to an optical analogue of electromagnetically-induced transparency, with a transmission spectrum featuring a narrow transparency peak within a broad transmission dip. (Courtesy of Sunil Sandhu and Professor Shanhui Fan)

3.2. STRIP WAVEGUIDES

In on-chip photonic-crystal devices, strip waveguides are typically used to facilitate coupling, because direct coupling from free space or telecom optical fiber to a W1 photonic-crystal waveguide (missing a row of air holes) is inefficient due to the large differences in effective refractive index, geometric size and profile of the optical modes. In this section, I will show an improved structure at the interfaces from the free space to the strip waveguide and from the strip waveguide to the W1 photonic-crystal waveguide to reduce reflections.

An intuitively simple solution for free-space to strip waveguide coupling is to increase the thickness and width of the waveguide at the coupling region and adiabatically taper it both laterally and vertically to the desired single-mode strip waveguide dimensions. Another approach is to introduce a surface grating to couple light perpendicularly to the planar waveguide [59]. However, most of these schemes require a number of additional processing steps that complicates the fabrication.

We instead adopted an inverse taper structure [60, 61] at the coupling interfaces. The strip waveguide is tapered to a width well below what could support a confined propagation mode. The optical modes thus spread extensively into the oxide cladding. This not only increases the modal size, but also decreases the effective index, both of which result in better coupling. Light in free space is coupled evanescently to the inverse taper and becomes progressively more confined as the width of the strip waveguide increases linearly from 150 nm to 400 nm over a distance of 50 μm . The gradual change of the width and effective refractive index significantly reduced back-reflections and

hence effectively eliminates Fabry-Perot “noise” oscillations in the transmission spectrum. One can find much weaker Fabry-Perot oscillations in the transmission spectrum in Figure 3.4(b) than those in Figure 3.4(a) owing to the improved impedance matching and the adiabatic effective index change. The reduction of Fabry-Perot reflections is crucial in order to unambiguously demonstrate the predicted effects that arise entirely from the interference between the two resonators.

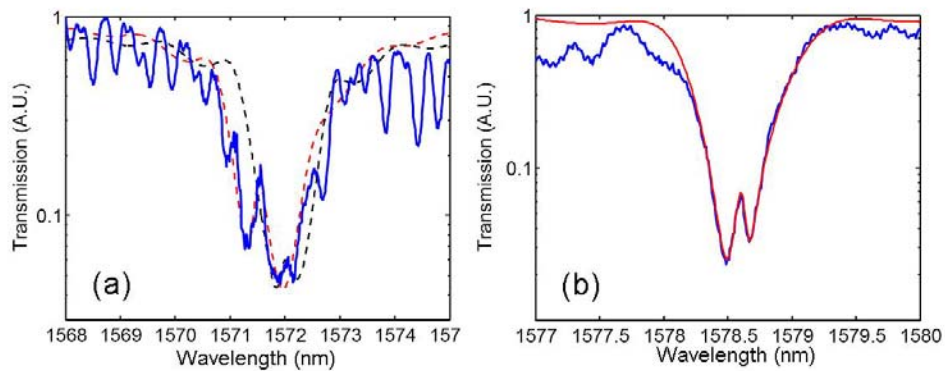


Figure 3.4. Comparison of the transmission spectra from devices (a) without and (b) with inverse tapers at coupling facets. (a) The prominent oscillations are due to strong back reflections at coupling facets. Features from coherent interactions are mixed with the oscillation noise. Experimental results are ambiguous, and could be fitted by multiple theoretical curves, *e.g.* either the red or blue dashed curves. (b) Oscillations are suppressed by the use of inverse tapers. The red theoretical curve fits well with the blue experimental result.

The next issue is the efficient coupling between the strip waveguide and the W1 photonic-crystal waveguide. The small group velocity of the TE mode in the W1 waveguide results in large impedance mismatch with the mode in the strip waveguide. Adiabatic approaches have been proposed, for example add smaller holes at the coupling region [62], or tapering the strip waveguide into the photonic-crystal waveguide [63]. In terms of fabrication, the easiest way is to simply butt couple the strip waveguide to the

photonic-crystal waveguide. In our devices, the width of the strip waveguide increases from 400 nm to 650 nm over a distance of 50 μm toward the photonic crystal.

3.3. DEVICE LAYOUT

Fabricated devices on each run are subject to fluctuations in the fabrication conditions, such as electron beam dose and etching rate. Our devices fabricated entirely in wafer pieces are particularly vulnerable to those fluctuations. More details about fabrication will be discussed in the next chapter. In this section, I will briefly talk about the device layout design in order to obtain at least a few working devices in one run of fabrication. We relied on fabricating an array of waveguides with different dose and geometric parameters. Out of about twenty devices that can be exposed in one e-beam lithography session, we divided them into three groups. Each group contained a half dozen waveguides, and waveguides within a group were separated by 50 μm from each other. Different groups were separated by 100 μm . This layout helped locate the waveguides in the subsequent optical measurements. Waveguides in the same group shared one identical parameter, such as dose, but varied another parameter, such as hole size.

It is ideal to cut and polish the coupling facet of the device right at the tip of the inverse taper. However, the polishing process at the Stanford crystal shop is only accurate to a dimension of 10 μm . On the other hand, the inverse tapers are very narrow in width, so it is difficult to extend the tip of the inverse taper very long. Therefore it is very likely that the inverse tapers will be either over-polished (tapers are gone) or under-polished

(the coupling facet is not polished to the position of the tip of the inverse taper). In order to overcome the difficulty, “stop signs” were created around the device region to improve the polishing accuracy. A “stop sign” was a set of adjacent 10-micron-wide silicon strips parallel to the waveguides. The ends of the columns were offset by $2\ \mu\text{m}$, with the first one starting slightly before the tip of the taper and the last one starting slightly after the position where the taper region completed. During polishing, one could determine the position of the facet relative to the inverse taper by counting the numbers of columns observed from the cross section. By using this method, polishing accuracy of 2-5 μm was achieved and a 5 μm extension of the tip of the inverse taper is sufficient. The “stop signs” were fabricated along with the photonic crystals and strip waveguides. These structures were very simple and did not increase any fabrication complexity, but they significantly improved the polishing accuracy.

4. FABRICATION

In this chapter, I will review the fabrication process of making suspended photonic-crystal membranes with oxide-clad strip waveguides in a silicon-on-insulator (SOI) platform. SOI is an attractive platform due to its wide availability, potential for strong optical confinement and compatibility for on-chip opto-electronic integration. The fabrication process is completed in the Stanford Nanofabrication Facility (SNF). Even though the recipes are equipment specific, the ideas are generic and highly transferrable to different fabrication facilities. In order to enable future researchers to repeat the process, I will provide detailed recipe for each step. In addition, I will also show some intermediate stages in the development of the process and alternatives for a few steps, which will potentially help future researchers further improve and optimize the process. At the end of this chapter, I will present an analysis of the quality of the fabricated photonic crystals based on SEM graphs.

4.1. OVERVIEW

4.1.1. WAFER PREPARATION

We start with 6" Unibond SOI wafers manufactured by SOITEC with a 320nm-thick top active silicon layer and 1.0 μ m-thick buried oxide layer. The buried oxide layer is chosen such that after etch removal, the evanescent wave is prevented from coupling and leaking into the underlying silicon wafer, but thin enough to avoid unnecessary

complexity in the step of membrane release. The thickness of the active silicon layer is chosen to be as close as to the designed thickness of the silicon membrane. If needed, digital etching (oxidation and etch) can be used to thin down the silicon layer accordingly to achieve the desired thickness. The SOI wafer is manufactured with the smart cut process. Both active and handle silicon wafers are p-type. The resistivity of the active wafer is 13.5-22.5 ohm-cm, and that of the handle wafer is 14-22 ohm-cm.

Pieces of $\sim 2\text{cm} \times 2\text{cm}$ in size, instead of whole 6" wafers, are used in fabrication. Because SOI wafers are generally thick compared to normal silicon wafers, it takes some practice to cleave the wafer decently into small squares. The ability to cleave a wafer piece cleanly and precisely (within a millimeter) is also helpful in characterizing a cross section (e.g. Figure 4.3). The method that I found handy is the following. First use a scribe to carefully notch the edges of a wafer at the desired position. Second flip the wafer upside down and place on a convex surface, such as a wafer carrier. Last, use the blade of Teflon tweezers to gently press the wafer at the notch, and the wafer will break neatly into two pieces.

4.1.2. OXIDE DEPOSITION

In order to prepare the surface for oxide deposition, one follows the standard SNF diffusion cleaning module to remove surface organic materials, trace of metals, and native oxide that may have grown on the surface of the wafers. This process leaves the wafer surface clean of any mobile ions in preparation for high temperature processing.

The process can be conducted in the “wbdiff” wet bench for wafers, or in clean quartz beakers at the “wbgeneral” wet bench for pieces.

A thin layer of oxide with thickness of 100-150 nm is deposited on the sample in the “teos2” low pressure chemical vapor deposition (LPCVD) system. This layer of oxide will serve as a hard mask in the subsequent step of reactive ion etching. The “teos2” system normally accepts only 4” and 6” wafers. In order to process pieces, a dummy wafer is placed flat at the bottom of the boat and pieces are then placed on the dummy wafer. Although the tube design is optimized for standup (vertical placed) wafers, the difference in deposition rate and uniformity between the vertical and horizontal configurations is insignificant in the system, at least for our devices covering an area only a few square millimeters. But the flat placed pieces are vulnerable to random peelings falling from the tube walls, so another dummy wafer is recommended to be placed above the pieces to protect them. The oxide deposition is followed by a step of one-hour annealing at 1100°C in the “tylan” system.

4.1.3. ELECTRON BEAM LITHOGRAPHY

The samples are first cleaned in acetone and isopropanol for 10 minutes each, optionally in an ultrasonic bath. Then prebake on a hotplate at 200 °C for 5 minutes. Spin coat with 5% 495K polymethyl methacrylate (PMMA) in anisole for 40 seconds at 2000 rpm, resulting in a 200nm-thick layer. Before placing the sample back onto the hotplate, remember to carefully clean the PMMA residue on the backside of the sample with Q-tips and acetone. The residues are very likely to ruin the leveling of the sample in the

succeeding electron-beam lithography. At last, bake the sample on a hotplate at 200 °C for 2 minutes.

We used the Raith 150 system in SNF to expose PMMA and define the device patterns. Before loading the sample, check that the back of the sample is clean so that the sample is well leveled on the stage. Because of the configuration of SOI wafers that the oxide layers are inserted between silicon layers, electron charge cannot conduct through the SOI substrate to the steel stage. Thus the top active silicon layer is connected to ground by a metal clip, otherwise charging will be a serious issue in exposure. Typical parameters used in exposure are voltage (10keV), aperture (20 μ m), and dose (135-150 μ C/cm²).

During exposure, air holes in the middle of the photonic crystal receive a higher electron dose than those at the edge. This proximity effect influences the hole uniformity around the cavity and waveguide, and seriously affects their characteristics, like Q . In designing the pattern, holes around the cavity should have higher nominal dose to compensate for the proximity effect. Depending on the scanning path of the electron beam, the nominally round air holes may come out elliptical. This defect can also be compensated by properly designed exposure pattern.

Develop the sample for 30 seconds in 3:1 in volume of MIBK and isopropanol. Shake gently. Rinse it with isopropanol for 30 seconds to stop developing.

4.1.4. REACTIVE ION ETCHING

Stick the pieces onto a carrier wafer with SPR3612, because the “P5000” etching system is only compatible with 4” wafers. The device patterns in PMMA are then transferred to the oxide hard mask (100~150nm thick, deposited in “teos2” before lithography) in Chamber B of the “P5000” plasma etching system using reactive ion etching for 80 seconds with fluorine based gases CF_4/CHF_3 and Ar. Gas flow rate is 20, 50, and 100 sccm respectively. Pressure is 250 mTorr and magnetic field is 50 Gauss. Because it is a high-temperature process, divide the total 80-second etching session into four 20-second sub-sessions separated with 30-second standby sessions in between to allow the sample to cool down.

The piece is taken off from the carrier wafer, sometimes with the help of acetone. The PMMA and SPR3612 are then stripped in the “gasonics” plasma system with a standard recipe #0166. The procedure is fast but also requires a 4” carrier wafer. In this case, the piece can be simply attached to a dummy wafer by double-sided carbon tape.

After stripping the polymer, attach the piece to a 4” carrier wafer again with SPR3612 photoresist. Load the sample back into the “P5000” system, but in Chamber C this time for silicon etching. Transfer the device patterns from the oxide hard mask to the active silicon layer with a combination of $\text{HBr}/\text{NF}_3/\text{He}/\text{O}_2$. Gas flow rate is 45, 10 and 8 sccm, respectively. Pressure is 90 mTorr, magnetic field is 65 Gauss, and power is 350W. The main etching last 45 seconds and etches through the 320nm-thick silicon.

4.1.5. OXIDE CLADDING DEPOSITION

After cleaning the sample again in acetone or the “gasonics” plasma system, the photonic crystals and the strip waveguides are completed in the silicon layer. The next step is to change their surroundings: let the strip waveguides buried in the oxide claddings and the photonic crystal slab sandwiched by air. I will dedicate Section 4.3 to describe the challenges, tests and solutions. Here, I will still continue to focus on the process flow to finish the device.

We first need to deposit a layer of oxide with thickness about 1 μm , roughly the same as that of the buried oxide layer, on top of the active silicon layer. Combined with the already existing buried oxide, the deposited oxide serves as the cladding around the strip silicon waveguides. The “teos2” LPCVD system is chosen for the deposition primarily for its exceptionally conformal coverage. Since we need to deposit more than one micron here, it is recommended to divide the deposition into two steps, each depositing 0.5~0.6 μm thick. Anneal the sample in the “tylan1” or “tylan2” tube at 1100°C for 1 hour to release the strain. Otherwise, the thick oxide could crack, or even worse, the overly strained oxide may damage the active silicon layer where the devices are located. A dummy silicon piece goes side by side with the real SOI piece through the process. The dummy piece is used to monitor the oxide thickness, as the thickness of the oxide on a silicon substrate can be measured much more easily and accurately than that on a SOI wafer.

4.1.6. BI-LAYER LITHOGRAPHY

The following steps are to mask the oxide cladding around the strip waveguide to prevent it from being etched by hydrofluoric acid in the subsequent membrane-release steps. LOL2000, a kind of non-UV-sensitive polymer, is first spun on the sample at 3000 rpm for 60 seconds, resulting in a 200 nm thick layer. Bake it on a hotplate at 160 °C for 5 minutes. Then spin coat SPR3612 photoresist at 5500 rpm for 30 seconds, resulting in a 1 μm thick layer. Bake at 90 °C for 1 minute. Expose the photoresist above the strip waveguides immediately in a “KarlSuss” aligner. The “KarlSuss” aligner system is a quite versatile exposure tool, which accommodates pieces and performs near-UV photoresist exposure. Typical conditions used in “KarlSuss” are front alignment, hard contact and 40 μm gap. Exposure time is between 1.2 seconds and 1.4 seconds, but it is recommended to calibrate on a dummy wafer before the real exposure. Develop immediately in MF-26 for 40 seconds and rinse by water for 1 minute. LOL2000 is an inert, non-UV-sensitive polymer, which can be etched with most standard developers. The standard MF-26 developer will clear the exposed SPR3612 areas and open up a window above the strip waveguides, but will also "etch" LOL2000, leading to undercutting of the photoresist (Figure 4.1 (a)). It is this overhang that prevents sidewall deposition of film and helps the lift-off process. Check under an optical microscope to assure the overhang feature.

4.1.7. METAL EVAPORATION

Prepare the sample for metal deposition by attaching the piece to a 4” wafer with Kapton tape. Cover the edges of the piece with tape for an easier lift-off process in the

future. Load the sample in the “Innotec” electron-beam metal evaporation system to deposit 10nm-thick chromium and 1800nm-thick gold. Gold is a good mask in hydrofluoric acid but adheres poorly to the substrate. The thin chromium layer serves as an adhesion layer. Evaporation is a directional process and results in the least conformal coverage, a desirable feature for lift-off applications. After this step, the sample is gold-contaminated and will not be allowed back into any SNF defined “clean equipment”.

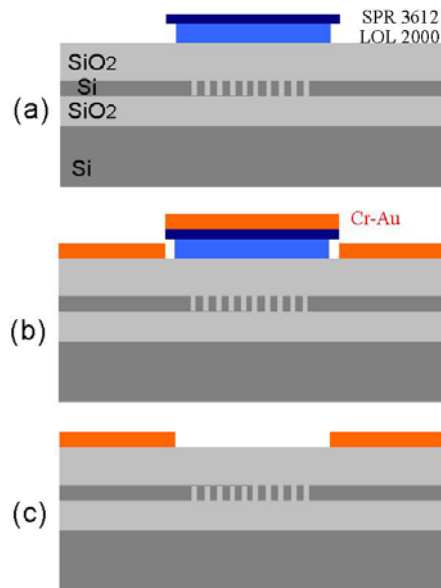


Figure 4.1. Schematics of the steps of (a) bi-layer lithography (b) metal evaporation (c) lift-off.

4.1.8. LIFT-OFF

The sample is thereafter placed in Microposit Remover 1165 overnight for lift-off. Gold-chromium on the strip waveguides adheres to the silicon dioxide and remains, but that on top of the photoresist which is above the photonic crystal area should be gone within 12 hours (Figure 4.1 (c)). If the metal is not completely removed, heating the

solvent to 50°C or cleaning the sample in an ultrasonic bath helps. Now, the metal mask has a window on the photonic crystal area for subsequent steps of membrane release.

4.1.9. HYDROFLUORIC ACID WET ETCHING

Prepare 10:1 hydrofluoric acid by mixing the standard 49% hydrofluoric acid and water in a plastic or Teflon beaker at the “wbgeneral” or “wbgaas” wet bench. Place the sample in a basket and slowly put it in the acid contained in the beaker. The hydrofluoric acid etches the oxide above the photonic crystal slab, penetrates through the air holes, removes the oxide underneath the slab, and releases the membrane, while the oxide cladding around the strip waveguides is intact under the protection of the gold mask. Etching time is 50-55 minutes, depending on the thickness of the oxide cladding.

4.1.10. FACET POLISHING

The sample is cut from the wafer piece. Coupling facets are polished toward the ends of the strip waveguides, and into mirror surfaces to facilitate transmission measurement. Since the device consists of a fragile suspended membrane, it is wise to provide some protective coating layers before the polishing procedure in the crystal shop. I usually spin coat three layers of 2% PMMA and then another three layers of 5% PMMA both at very low speed, 1000 rpm. Bake on a hotplate at 200 °C for 5 minutes after coating each layer. The dilute 2% PMMA is likely to penetrate the photonic-crystal holes and support the membrane from underneath. The thicker 5% PMMA is stronger and protects the whole device.

4.1.11. FINAL CLEANING

Remove PMMA in acetone or other solvent-based removers. The sample is now only a millimeter wide after polishing, so handle with great care. You may notice that the gold-chromium mask has not been removed. It is intentionally left after the polishing procedure because the process of mask stripping takes away the “dirt” generated during the polishing process. The “dirt”, which is actually silica particles, sticking very strongly on the sample, is very difficult to clean otherwise. The metal removal is straightforward: place the sample for 8 minutes in gold etcher and 40 seconds in chromium etcher. The silica particles are removed in this process. Figure 4.2 shows a SEM graph of a completed device.

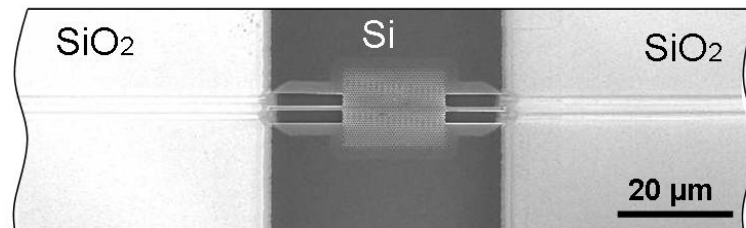


Figure 4.2. SEM of a completed device. The photonic crystal membrane is suspended. The strip waveguides extend to the oxide cladding.

4.2. PATTERN TRANSFER

Patterns in PMMA can be transferred to silicon directly by using fluorine based gases ($\text{CHClF}_2/\text{SF}_6$) in the “drytek2” system, or HBr/Cl_2 chemistry in the “P5000” system. But the previously discussed two-step etching process is adopted because a) it enables deep etching in silicon; b) it results in straighter vertical side walls. Oxide has a much higher selectivity than PMMA in etching with silicon, and has been used to etch

several microns deep into silicon. This feature provides the necessary flexibility for the slab height, thus makes the etching recipe much more adaptable to different structure designs. More importantly, the high selectivity and anisotropy lead to much more vertical side walls in the photonic crystal air holes, an essential feature for fabricating high- Q cavities. Figure 4.3 shows a comparison of the etching results by these two methods.

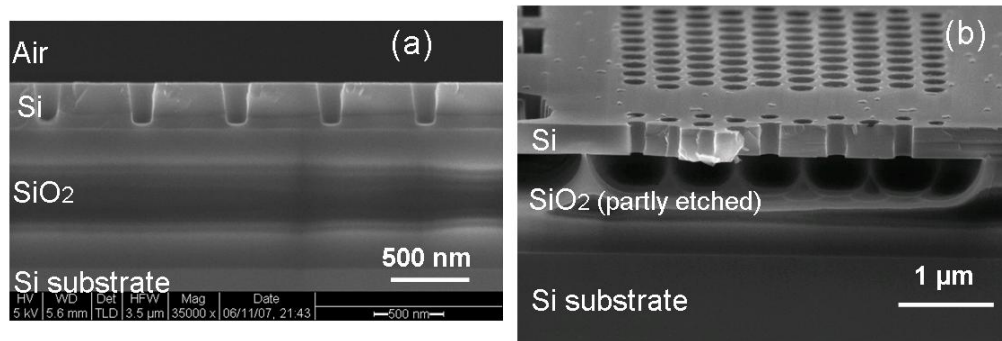


Figure 4.3. Comparison of cross sections of the photonic crystal air holes in silicon slabs. (a) Patterns transferred from PMMA to silicon directly. (b) Patterns transferred from PMMA to oxide and then to silicon. Method (b) results in much more vertical side walls.

Because the “P5000” etching system is only compatible with 4” wafers, pieces have to be attached to a carrier wafer. In that configuration, the temperature on the sample can be quite different than the program-specified temperature on the carrier wafer. The uneven wafer surface due to the attached piece changes the gas flow. One often finds the pieces have fallen off the carrier wafer and are lost in chamber, or the temperature is so high that the PMMA is burned and the patterns are damaged. Examples of unsatisfactory results are shown in Figure 4.4. After extensive tests, I found the following procedure work well. Spin coat SPR3612 photoresist on a 4” wafer for 30 seconds at 1500 rpm. Immediately stick the piece on the 4” carrier wafer. Gently press the piece to make sure it

sticks well. Bake the wafer on a hotplate for 30 minutes at 90 °C. It is recommended to gradually ramp up the temperature in order to drive out the air bubbles between the piece and the wafer. Oxide etching using fluorine based gases CF_4/CHF_3 and Ar is a high temperature process, and the backside helium gas flow does not cool down the piece as efficiently as the carrier wafer. In order to avoid resist burning, I divided the 80-second etching session into four 20-second etching sessions, and added a 30-second standby session between each etching session. The gas flow and pressure of the standby sessions are the same as those in the etching sessions, but the plasma electromagnetic fields are turned off in the standby sessions.

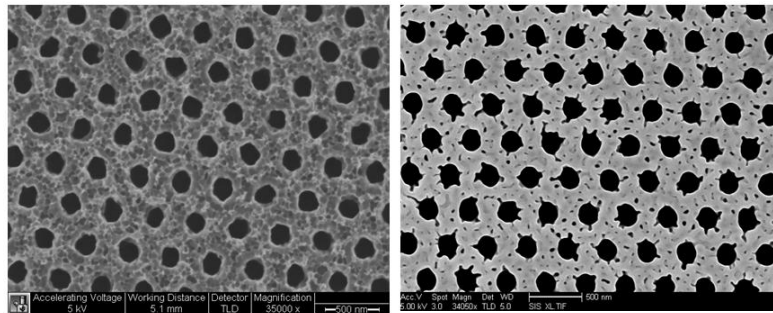


Figure 4.4. Examples of unsatisfactory photonic crystals etched by over-heated processes.

4.3. SELECTIVE MEMBRANE RELEASE

4.3.1. MASK

SU-8, a chemically amplified negative photoresist, was the first candidate. Cured SU-8 films are highly resistant to solvents and acids, making them suitable for masking purposes. While this provided some encouraging results, they are inconsistent. The optical microscopic images in Figure 4.5(a)(b) show how SU-8 mask behaved against HF.

The same waveguide showed sufficient protection on one end in figure (a), but the other end suffered substantial leakage in figure (b). HF penetrated through the cracks in the SU-8 layer and etched the oxide layer below. In Figure 4.5(c), SU-8 was spun on an oxide layer instead of on the SOI directly. The right part of the waveguide was fine, but the left part collapsed because the supporting oxide underneath the silicon strip was etched away. SU-8 was extraordinary difficult to remove after exposure, and left residues that can be seen in Figure 4.5(c).

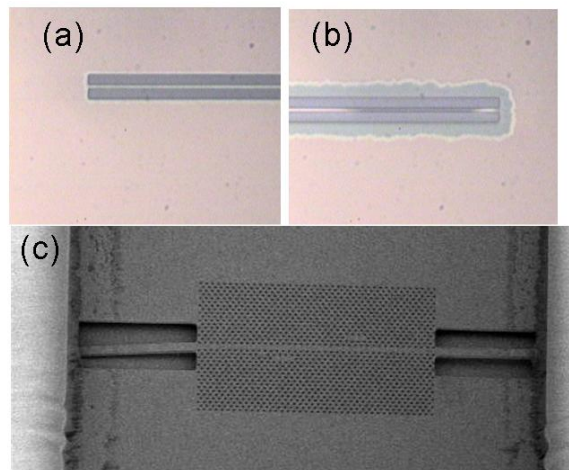


Figure 4.5. Results of membrane release with SU-8 masks. (a) and (b) shows optical microscopic images of the two ends of a same waveguide. The left part survived and right part suffered HF leakage and collapsed. (c) SEM of a released photonic crystal membrane with connected strip waveguides. The waveguide on the right hand side of the photonic crystal was good but the part on the left hand side collapsed. In conclusion, SU-8 mask provides inconsistent results. Figure (c) also shows some hard-to-remove SU-8 residues.

Metal was the second candidate. Gold has excellent resistance in acid but poor adhesion to the substrate. So a thin layer of chromium was deposited before gold to improve its adhesion. Evaporation was used for metal deposition, because it is a very directional process and results in the least conformal coverage, ideal for lift-off. The

drawback is the poor coverage at the waveguide edges even though the metal layer is thicker than the height of the waveguide (Figure 4.6(a)). HF would effortlessly leak through the obvious cracks at the waveguide edge and etch the oxide underneath. Therefore, a layer of oxide on top of the silicon layer is highly desirable, as it not only serves as the cladding but also smoothes the surface and dramatically improves the metal coverage (Figure 4.6(b)).

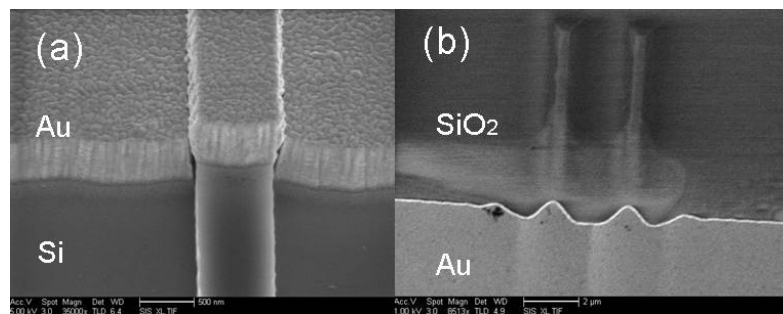


Figure 4.6. Gold coverage. (a) Evaporation process resulted in poor coverage of gold mask at the edge of the strip waveguide. (b) The deposited oxide cladding smoothed the surface and significantly improved the coverage of gold.

4.3.2. OXIDE

There seem plenty of systems to choose to deposit the oxide, such as the “sts” plasma enhanced chemical vapor deposition (PECVD) system, the “tylanbpsg” low pressure chemical vapor deposition (LPCVD) system and the “teos2” LPCVD system. But we have many constraints too. First, the refractive index should be as close as possible to that of the buried oxide layer (thermal oxide) in order to maximally maintain the $z=0$ reflection symmetry. Second, the deposition should be as conformal as possible for good coverage. Third, the system should be able to accommodate pieces in one way or another. Last, HF etching rate should be as low as possible so that there is minimum

lateral etching during the membrane release. The buried oxide is thermal oxide, whose etching rate is lower compared to the deposited oxide, so it takes time to release the membrane. Meanwhile, if the etching rate of the deposited oxide is too fast, HF will flow substantially in the horizontal direction under the gold mask and etch away the oxide cladding.

The “sts” PECVD system is fast and perfectly compatible with pieces. However, results are far from satisfactory. As shown in Figure 4.7(a), the oxide exhibited obvious interfaces at the waveguide edges, even after annealing at 1000 °C for 2 hours. Figure 4.7(b) shows the results of the sample after dipped in 10:1 HF for merely 5 minutes. HF quickly etched through the interface and began to reach the buried oxide. After 25 minutes in HF (Figure 4.7(c)), before the membrane was released, the oxide cladding around the waveguide had been gone by laterally etching, even though it was covered by a gold mask.

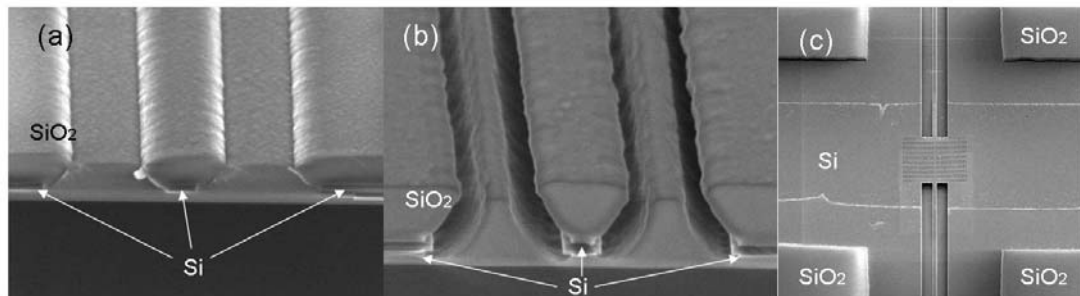


Figure 4.7. 3 μ m-thick oxide. (a) Deposited by the “sts” PECVD system, and annealed at 1100 °C for 1 hour. (b) Dipped in 10:1 HF for 5 minutes. (c) Placed in 10:1 HF for 25 minutes with a gold mask. The gold mask was removed before taking this picture.

LPCVD leads to more conformal coverage and more uniform oxide. Figure 4.8 shows the result of membrane release for the low temperature oxide (LTO) (deposited in

the “tylanbpsg” tube) without (a) and with (b) annealing. We no longer observed the obvious interfaces at the edge of the waveguide even before annealing. Annealing for 1 hour at 1100 °C significantly densified the oxide and decreased its etching rate.

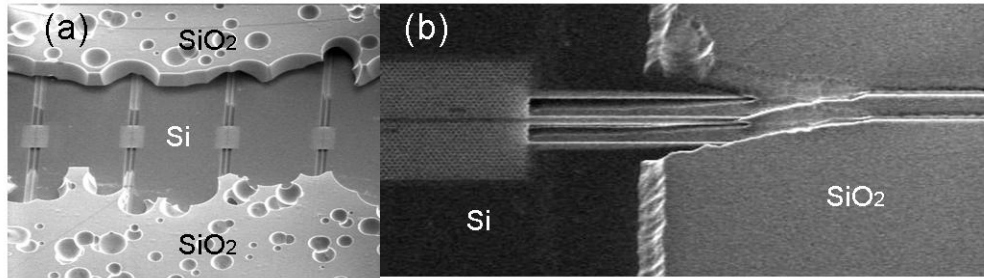


Figure 4.8. Results of low temperature oxide (LTO) deposited in the “tylanbpsg” tube. (a) Without annealing. (b) Annealed at 1100 °C for 1 hour.

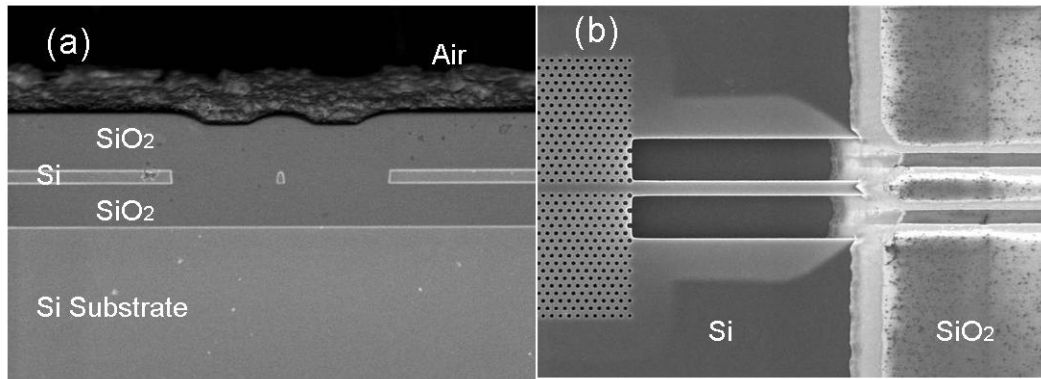


Figure 4.9. Results of the oxide deposited in the “teos2” tube. (a) Cross section of the strip waveguide surrounded by oxide cladding. (b) Top view of the interface between the suspended waveguide and the cladding-supported waveguide.

The “teos2” LPCVD tube provides even better results, shown in Figure 4.9. Figure 4.9(a) is a cross-section of the oxide-clad strip waveguide. Not only the deposition is very conformal, but no interface is observed between the deposited “teos2” oxide and the buried oxide originally manufactured in the SOI wafer. Figure 4.9(b) is the top view at the interface between the suspended waveguide and the cladding-supported waveguide.

The triangular shape indent observed at this place in Figure 4.8(b), which was due to the faster etching rate of the oxide along the edge of the waveguide, has disappeared in Figure 4.9(b). The etching rate of the oxide in 10:1 HF is 570 Å/min on average (Figure 4.10), the lowest among all the deposited oxide tested, and the closest to that of thermal oxide.

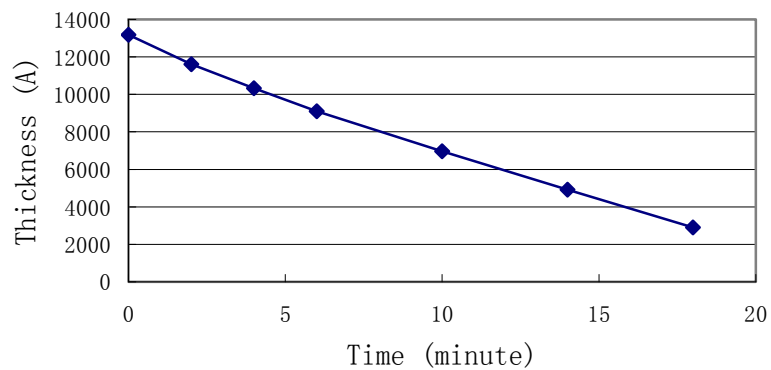


Figure 4.10. Etching rate of the oxide deposited in the “teos2” tube, etched with 10:1 HF. The average etching rate is 570 Å/min, the slowest among all the deposited oxide tested.

4.4. SEM-BASED FABRICATION ANALYSIS

Fabricated photonic crystals could have discrepancies from the design in hole shape, hole size, lattice constant etc. The geometrical disorders significantly influence the characters of the cavity and waveguide [64]. Hence, we used SEM graphs to analyze the quality of the fabricated photonic crystals.

4.4.1. SEM IMAGE PROCESSING

The SEM graphs were converted from grayscale into binary black-and-white, using the Matlab built-in functions, `im2double` and `im2bw`. The argument level in `im2bw` is

the threshold of the digital conversion, in which all numbers (gray scale) below the level are converted to zero (black), and above the level to one (white). The proper threshold depends on the brightness of the SEM graph. The trial-and-error method was used to find the value of this argument up to a proper range. Using a value beyond the proper range, the converted image would be completely white or black. The exact value of the converting threshold has to be inferred by an inverse process. We relied on the fact that the extracted hole size increase monotonically with the threshold (Figure 4.12(b)), and the resonant wavelength is highly sensitive to the real hole size. By measuring the cavity resonant wavelength experimentally, we could therefore determine the proper value for the conversion threshold.

Dirt on the sample adds substantial unnecessary complexity in data analysis, since it might mix with the real feature or even worse cover the feature. As a result, it is important to keep the sample surface as clean as possible when taking SEM pictures. Dirt with size much larger or smaller than the holes, as well as noise can mostly be eliminated by labeling (`bwlabel` function) and deleting collectively. Any remaining dirt, with area comparable to that of the air hole, has to be treated manually.

In order to keep sufficient resolution for each hole and obtain enough number of holes, a number of SEM graphs were taken around the cavity at the same magnification, orientation, brightness and contrast. We then combined them by aligning a common hole, such as the size hole of the cavity. Figure 4.11 shows the digitization and combination of SEM graphs.

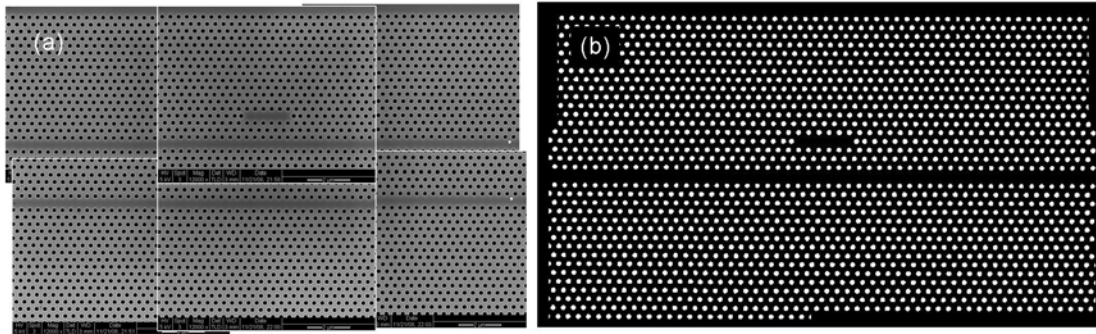


Figure 4.11. Digitization and combination of SEM graphs. (a) Original SEM graphs around a photonic-crystal cavity with the same magnification, orientation, brightness and contrast. (b) SEM graphs are converted to black-and-white images, and combined into a single image.

4.4.2. STATISTICS

Geometrical parameters, such as the hole diameter and nearest-neighbor distance, are extracted from the digitized SEM graphs. As shown in Figure 4.12(b), the mean of hole diameter is certainly dependent on the conversion threshold, but its uniformity is not, as the standard deviation is about the same for different threshold settings. Figure 4.12(a) shows the hole diameter distribution has a bell-shaped profile. The mean is 217nm and the standard deviation is 2.0nm. It is fairly uniform, reflecting stable e-beam writing. In plotting the histogram, the threshold was taken as 0.6 and the smaller holes along the cavity and waveguide were not counted.

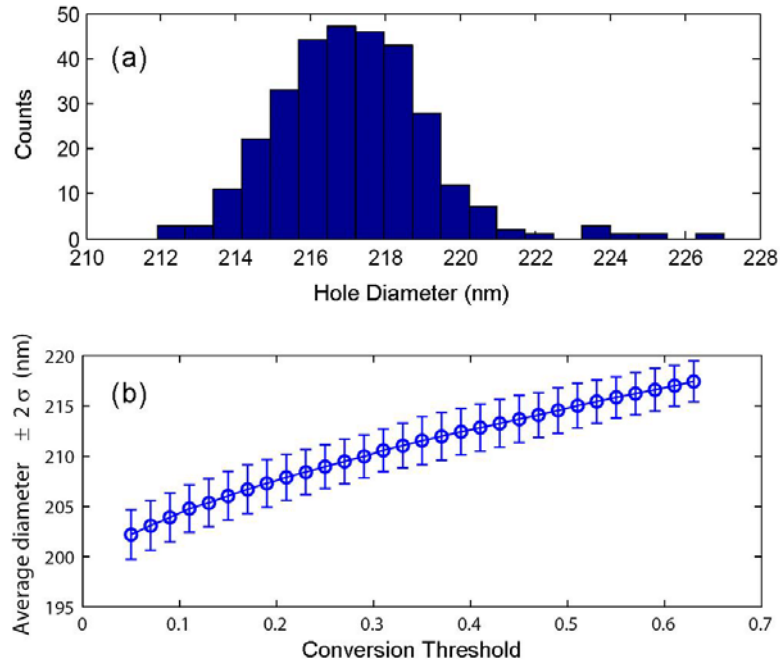


Figure 4.12. Analysis of air hole diameters in a fabricated photonic-crystal slab. (a) Histogram of hole diameter. The mean is 217nm and the standard deviation is 2.0nm. Smaller air holes along the waveguide and cavity are not counted. (b) Mean of extracted value of the hole diameter increases monotonically with the conversion threshold. But the standard deviation is almost a constant. So the analysis of uniformity is not affected by the choice of the threshold.

Lattice constant is another important parameter in photonic crystal design. Figure 4.13(a) shows a histogram of the distance between the nearest neighbors. The mean is 385 nm, very close to the designed 386 nm. The standard deviation is merely 2.7 nm, which is small owing to the precise position control in the e-beam lithography. The already-small deviation and non-uniformity could be partly attributed to the non-roundness of the air holes, which could shift the center of gravity. In addition, as shown in Figure 4.13(b), the distances between nearest neighbors mix well, and are orientation-independent.

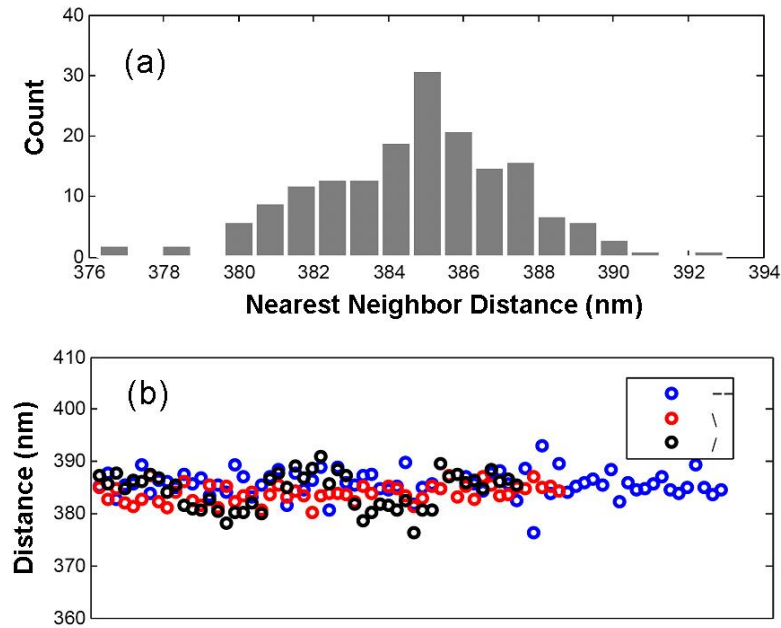


Figure 4.13. Analysis of the lattice constant in a fabricated photonic-crystal slab. (a) Histogram of the distance between adjacent holes. The mean is 385nm and the standard deviation 2.7nm. (b) Orientation analysis of the nearest-neighbor distance. Distances in three orientations mix well and no obvious orientation dependence is observed.

4.4.3. INPUT FOR FDTD SIMULATION

Simulation usually uses an ideal structure with perfectly round, uniform air holes. Fabricated devices, however, suffer geometrical disorders as well as rough and non-vertical side walls. These disorders result in a discrepancy between the simulated results and the measured properties. In order to reduce the discrepancy, we simulated two structures that better resemble the real one. The first structure used only the first moment of the distribution. It was a uniform structure constructed by using the mean of the diameter and nearest-neighbor distance. The second one was simply the digitized SEM (e.g. Figure 4.11(b)), which incorporated the variation of the hole size and position. Neither structure included side wall roughness, for the limit of resolution, and tilt of side

walls, which were in the third dimension. Results from both structures were close to the measured properties, indicating that the geometrical disorder, particularly the first moment, is the first order effect in influencing the photonic-crystal cavity characters.

5. POST-FABRICATION TUNING

Photonic-crystal structures incorporating multiple microcavities are predicted to exhibit a wide range of useful optical functionalities. Two-cavity designs, for example, can be tailored to give all-pass [35], band-pass [65], flat-top [37, 65], or channel-drop [66] filter response. Coupled multi-cavity structures have further been proposed for slowing [29, 33, 35] and stopping [29, 31] of light. However, an important prerequisite for the experimental demonstration of any of these schemes is the ability to tune different microcavities to a desired resonance frequency. Due to slight geometrical errors introduced during the fabrication process, it is virtually impossible to fabricate two photonic-crystal microcavities with identical resonances. In this chapter, we demonstrate the use of differential thermal tuning to align the resonance frequencies of two microcavities in photonic-crystal structures, eliminating the effects of fabrication errors.

The thermal tuning technique requires no extra materials or structures, which avoids the potential quality degradation of the photonic crystal microcavities and excess fabrication complexity. Furthermore, we directly measure device transmission in our experiments, rather than measuring the light emitted out of the photonic-crystal plane as in some previous work [25, 67]. Transmission measurements are particularly relevant in the context of on-chip, integrated optics applications, where the ultimate goal is to integrate multiple or cascaded devices. For instance, experiments in reference [23] have

demonstrated that differential thermal tuning can be used to tune the transmission lineshape of silicon microresonator devices yielding adjustable optical delays.

5.1. LASER-PUMPED TUNING

In this section, we first characterize a single cavity resonance in the presence of laser pumping. By using the cavity resonance, we probed the spatial distribution of both temperature and free carrier concentration in the slab associated with the laser pumping.

To tune the microcavity resonance, an Ar-ion, CW pump laser with a wavelength of 514nm was focused onto the surface of the photonic crystal from the perpendicular (vertical) direction. The spot size of the pumping laser is 2~3 μm in diameter. The laser spot was first focused in an area near the cavity. The size and position of the laser spot is illustrated by the green dot in Figure 5.1(a), and the transmission spectra are plotted in Figure 5.1(b). The transmission dip corresponds to the resonance of the cavity, generating a Lorentzian optical response. We observed a redshift of the cavity resonant wavelength with the increasing laser power. The reason is the following. The focused laser beam induces a thermal gradient in the suspended silicon membrane, which raises the refractive index (n) at the cavity. The increased refractive index pushes up the resonant wavelength of the cavity. For silicon, $\Delta n / \Delta T$ is $1.85 \times 10^{-4} / \text{K}$ at $1.55 \mu\text{m}$ [68] so a temperature rise of 10 K will result in an index increase of 0.00185, roughly 0.05%. Since the fractional resonance wavelength shift approximately equals the fractional refractive index change ($\Delta\lambda / \lambda \approx \Delta n / n$), a 10K cavity “warming” leads to a 0.05% resonant wavelength shift, or 0.8 nm at our measured wavelength.

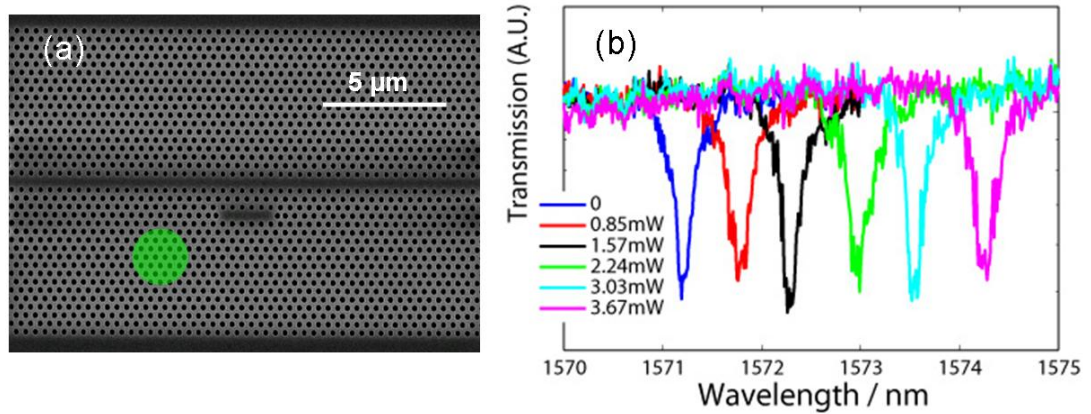


Figure 5.1. Single cavity tuning by a laser focused at an area a few microns away from the cavity. (a) SEM of the cavity and illustration of the laser spot by the green dot. (b) Transmission spectra in the presence of the pumping laser with different laser powers. The transmission dip corresponds to the cavity resonance. The resonance shifts to a longer wavelength with increased laser power.

However, it is only part of the story. When the laser spot was moved to a point very close to the cavity or even on the cavity (illustrated in Figure 5.2(a)), the corresponding transmission spectra were recorded in Figure 5.2(b). With increasing laser power, in addition to the redshift, we consistently observed a prominent reduction of the depth in the transmission dip. The reason is the following. Photons in the pump laser are absorbed by silicon and their energy is used to generate electron-hole pairs. These free carriers are able to reach the cavity before they recombine, when the laser-cavity separation is smaller than the electron and hole diffusion lengths in silicon. The increased concentration of free carriers has two effects: first decreasing the refractive index, second increasing the material absorption loss. These effects can be quantified as follows [69, 70]:

$$\Delta n = \Delta n_e + \Delta n_h = -[8.8 \times 10^{-22} \cdot \Delta N + 8.5 \times 10^{-18} \cdot (\Delta P)^{0.8}] \quad (5.1)$$

$$\Delta\alpha = \Delta\alpha_e + \Delta\alpha_h = 8.5 \times 10^{-18} \cdot \Delta N + 6.0 \times 10^{-18} \cdot \Delta P, \quad (5.2)$$

where α is the absorption loss coefficient in cm^{-1} , N and P are electron and hole concentration in cm^{-3} , respectively. The decreased refractive index leads to a blueshift in the background of the thermal redshift, however, the thermal effect still dominates. So in this case, only redshifts are observed. The increased material loss leads to excessive intrinsic optical loss in the cavity, since the intrinsic loss consists of a combination of the radiation loss and material loss. Optically, the intrinsic loss rate γ_i goes up and the intrinsic quality factor Q_i comes down. As discussed in section 2.1, in a Lorentzian generated by the resonance of a single cavity, the depth of the transmission dip, or the inverse of the transmittance, is approximately proportional to the square of Q_i . Hence the material loss reduces the depth in the transmission dip. In the case of Figure 5.1, where the laser was focused a few microns away from the cavity, the injected excessive free carriers recombined before reaching the cavity. The carrier concentration in the cavity was the original equilibrium level, so there was no additional material loss.

Tuning the resonant wavelength and the intrinsic loss are both of great practical importance. The thermal tuning of the resonant wavelength has been demonstrated to control the resonance of a single microcavity [25, 71], align the resonant frequency of a single microcavity to a quantum dot [67] in photonic-crystal structures, and align multiple cavity resonances, as shown in the subsequent section of this dissertation. The induced intrinsic loss can be potentially used to modulate the bandwidth of a coupled-resonator optical waveguide for stopping and time-reversing a light pulse [72].

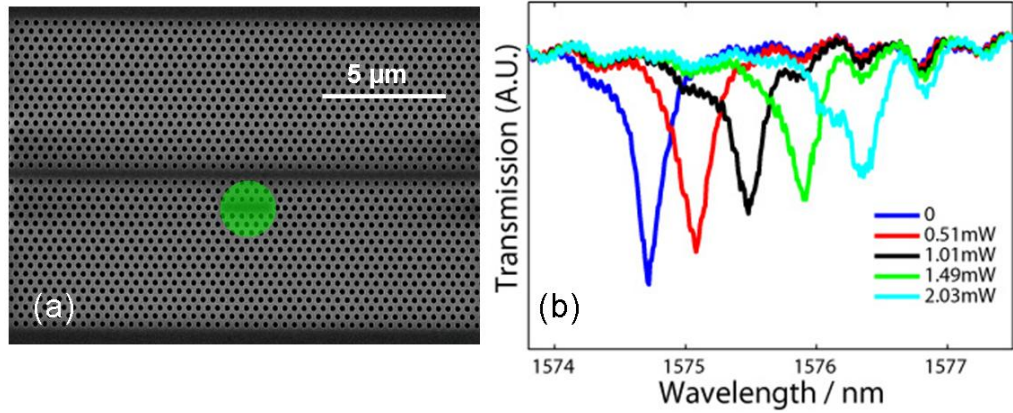


Figure 5.2. Single cavity tuning by a laser focused on the cavity. (a) SEM of the cavity and illustration of the laser spot by the green dot. (b) Transmission spectra in the presence of the pumping laser with different laser powers. The transmission dip corresponds to the cavity resonance. In addition to the redshift, the depth of the transmission dip decreased with increased laser power, due to injected free carriers, which induced excessive material loss.

5.1.1. DIFFUSION LENGTH OF FREE CARRIERS

The diffusion length of free carriers can be estimated by a back-of-the-envelope calculation. The resistivity of the boron doped silicon layer in the SOI wafer is between 13.5 and 22.5 $\Omega\cdot\text{cm}$, corresponding to the dopant density of around 10^{15} cm^{-3} [73]. We assume that the mobility of the electrons is around $1400 \text{ cm}^2\text{V}^{-1}\text{s}^{-1}$ [73]. By the Einstein relation, the diffusivity is

$$D_e = \frac{kT}{q} \mu_e = 0.0259 \times 1400 = 36.26 \text{ cm}^2\text{s}^{-1}. \quad (5.3)$$

According to reference [74], the minority carrier lifetimes in completed Si devices tend to lie about midway between milliseconds (after gettering) and nanoseconds (intentionally gold contaminated). But minority carrier life time in a similar kind of photonic crystal slab has been reported to be 80 ps [75], which is much shorter than that

of typical bulk silicon. This is likely due to the considerable number of unpassivated surfaces of the air holes. Hence the diffusion length is

$$L_e = \sqrt{D_e \tau_e} = \sqrt{36.26 \text{ cm}^2\text{s}^{-1} \times 80 \text{ ps}} = 0.5386 \text{ } \mu\text{m}. \quad (5.4)$$

Even if the carrier lifetime rose to 1 ns, the diffusion length would be merely 1.9 μm . So it is sufficient to eliminate the free-carrier related loss in the cavity by moving the laser spot a few microns away from the cavity. This is consistent with our experimental results. For comparison, the lattice constant is 0.386 μm and distance between the waveguide and the cavity is 1.34 μm . The diameter of the laser spot is 2-3 μm .

5.1.2. SPATIAL CHARACTERIZATION OF THERMAL AND FREE-CARRIER EFFECTS

In order to characterize the spatial distribution of temperature and free carrier concentration in the slab, we scanned the laser spot across the photonic-crystal slab along two pathways, shown in the blue and red arrows in Figure 5.3(a). Both pathways were parallel to the waveguide. The blue pathway went through the cavity, but the red one was about 3 μm away from the cavity. The resonant wavelength shift and the transmission dip depth were recorded as a function of laser spot position in Figure 5.3(b) and (c) respectively.

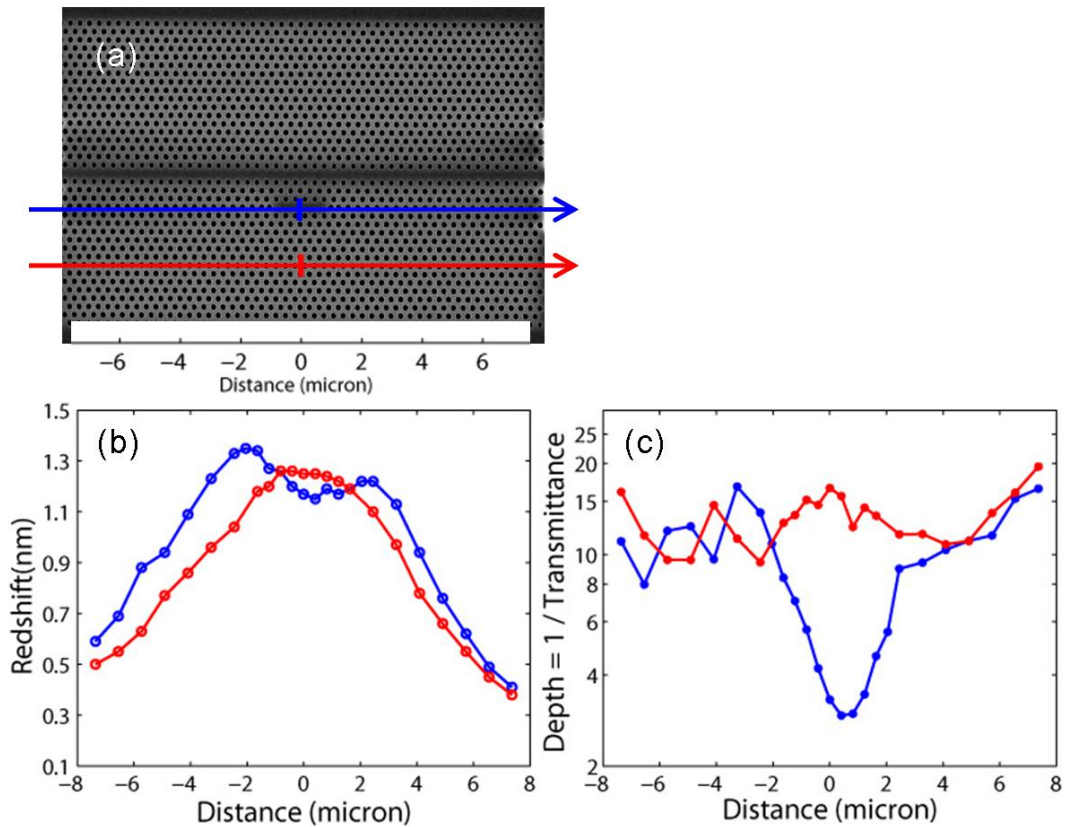


Figure 5.3. Spatial characterization of thermal and free-carrier effects in the slab. (a) SEM of the cavity and illustration of the laser spot scanning pathways. The blue pathways went through the cavity and the red one was $3\mu\text{m}$ away. (b) Redshift of the cavity resonant wavelength as a function of the laser position. (c) Depth of the transmission dip as a function of the laser position.

The red curve in Figure 5.3(b) shows a bell-shaped profile, corresponding to the temperature distribution in the slab. Since the thermal conductivity of silicon is much larger than that of air, the temperature distribution outside the laser spot can be modeled by a two-dimensional Laplace equation. Its solution has a $\log(r)$ form, where r is the distance from the laser spot, which matches well with the experimental curve. The red curve in Figure 5.3(c) is approximately a constant, indicating the absence of the free

carriers at the cavity. Free carriers generated by the pumping laser recombined before diffusing to the cavity.

The wing of the blue curve in Figure 5.3(b) still exhibits a $\log(r)$ dependence. But there is a dip at the peak of curve within $\pm 2-3 \mu\text{m}$. It is the resonant wavelength blueshift as a consequence of the reduced refractive index. The blue curve in Figure 5.3(c) also has a prominent dip in the same position, which is caused by free-carrier induced material loss.

5.1.3. ESTIMATION OF FREE-CARRIER CONCENTRATION

The carrier concentration, in principle, can be inferred from the preceding experimental data in two ways, one from the resonant wavelength shift and the other from the increased intrinsic loss.

In contrast to the thermal effect, the free-carrier effect decreases the refractive index and shifts the cavity resonance to a shorter wavelength. Given $\Delta\lambda / \lambda = \Delta n / n$, $n = 3.48$ at 1550nm, and $\Delta N = \Delta P$ as free carriers are generated in pairs, the carrier concentration could be calculated from Equation (5.1). By assuming $\Delta\lambda = 0.2\text{nm}$ at the origin when the laser spot was placed on the cavity, the carrier concentration is estimated to be $\sim 10^{17} \text{ cm}^{-3}$. However, the exact amount the blueshift is unknown, as the blueshift takes place in the background of the redshift. The thermal and free-carrier effects are competing with each other.

Distance(μm)	Q_{int}	α_i (cm^{-1})	$\Delta\alpha$ (cm^{-1})	ΔN (10^{18}cm^{-3})
-2.0455	14,000	9.93	4.37	0.30
-1.6364	12,000	11.58	6.02	0.42
-1.2273	10,000	13.90	8.34	0.58
-0.8182	8,000	17.38	11.82	0.81
-0.4091	6,000	23.17	17.61	1.21
0	5,200	26.73	21.17	1.46
0.4091	5,800	23.97	18.41	1.27
0.8182	6,500	21.39	15.83	1.09
1.2273	8,500	16.35	10.79	0.74
1.6364	10,000	13.90	8.34	0.57
2.0455	14,000	9.93	4.37	0.30

Table 5.1. Carrier concentration estimated from the increased intrinsic loss or decreased intrinsic quality factor, which is extracted from Figure 5.3.

The carrier concentration inferred from the intrinsic loss is more reliable. The intrinsic quality factor Q_{int} can be extracted by fitting the experimental transmission spectrum with the theoretical Lorentzian in Equation (2.7). The intrinsic quality factor Q_{int} is related to the absorption coefficient α by

$$Q_{int} = 2\pi n / \alpha_i \lambda_0, \quad (5.5)$$

where n is the refractive index, λ_0 is the resonant wavelength of the cavity, and α_i is the intrinsic loss coefficient. For example, without laser pumping, the resonator appears to have $Q_{int} = 25,000$, corresponding to $\alpha_i = 5.56 \text{ cm}^{-1}$. The intrinsic loss can be attributed to two parts, structural radiation loss and material loss. The carrier-injection increases the

material loss but does not change the radiation loss of the cavity, at least to first order. So the difference of α_i between the presence and absence of the pumping laser is purely increased material loss rate, $\Delta\alpha$, due to the increased free carrier concentration. Given the fact that free carriers are generated in pairs $\Delta N = \Delta P$, the increased carrier concentration has been estimated from (5.2), and listed in Table 5.1. Carrier concentration at the laser spot is on the order of 10^{18} cm^{-3} . The estimation from the material loss is larger than that from the blueshift.

5.2. DIFFERENTIAL TUNING TO ALIGN CAVITY RESONANCES

A variety of optical functionalities in multi-cavity systems based upon coherent interactions require aligning the cavity resonances within a linewidth or better. Despite the well fabricated photonic crystals, it is generally impossible to fabricate two microcavities with identical resonant wavelengths because of the geometrical disorders introduced during the fabrication process. This requirement imposes incredibly strict fabrication tolerances. The laser-pumped tuning provides the capability to control an individual cavity resonance and make it resonant at a desired wavelength. The differential tuning, relying on introducing a gradient in the slab, is able to control one cavity relative to the others in a multi-cavity system. In particular, we demonstrated using laser-pumped thermal tuning to align the cavity resonances.

We used a silicon-membrane PhC structure with a triangular lattice of air holes. Figure 5.4(a) shows a SEM graph of the device. A single-line-defect (W1) waveguide was formed by removing one row of holes. Away from the central region, the W1

waveguide was coupled to a lower-loss strip waveguide. The center-to-center separation of the microcavities was about 54 μm in the horizontal direction, and each microcavity was separated from the waveguide by three rows of holes. Under the SEM, the two microcavities appear identical.

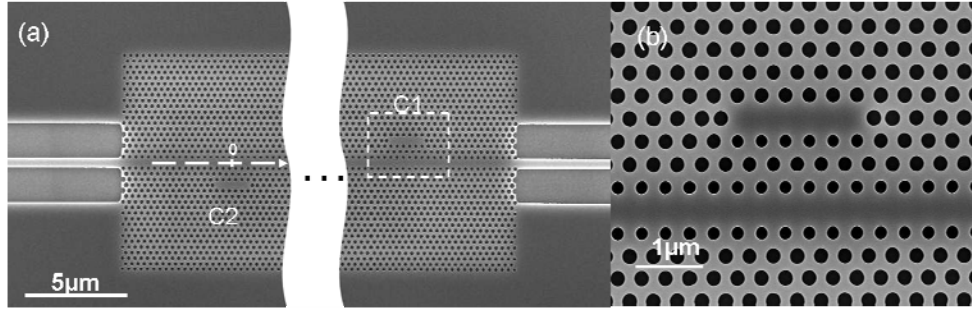


Figure 5.4. SEM images of the fabricated device. (a) Top view of the PhC structure with two cavities. (b) Magnified view of microcavity C1.

The transmission spectrum of the fabricated device is shown by the black solid line in Figure 5.5(a). The red dashed line is the theoretical fitting according to Equations (2.21)-(2.23). In the absence of the pump laser, the structure exhibits two distinct transmission dips at 1568.99 and 1572.14 nm, corresponding to resonances for cavities C1 and C2 (Figure 2a). Cavity C1 has Q_{int} and Q_{c} of 9,500 and 3,000 respectively, and C2 has Q_{int} and Q_{c} of 5,000 and 1,600. The difference in resonant wavelengths and quality factors can be attributed to visually imperceptible fabrication differences between the cavities shown in Figure 5.4. In our experimental devices, the difference in resonance wavelength between two cavities on the same sample was typically several nanometers. In the application which requires strict resonance alignment, introducing a post-fabrication tuning method is essential to relax the fabrication requirements.

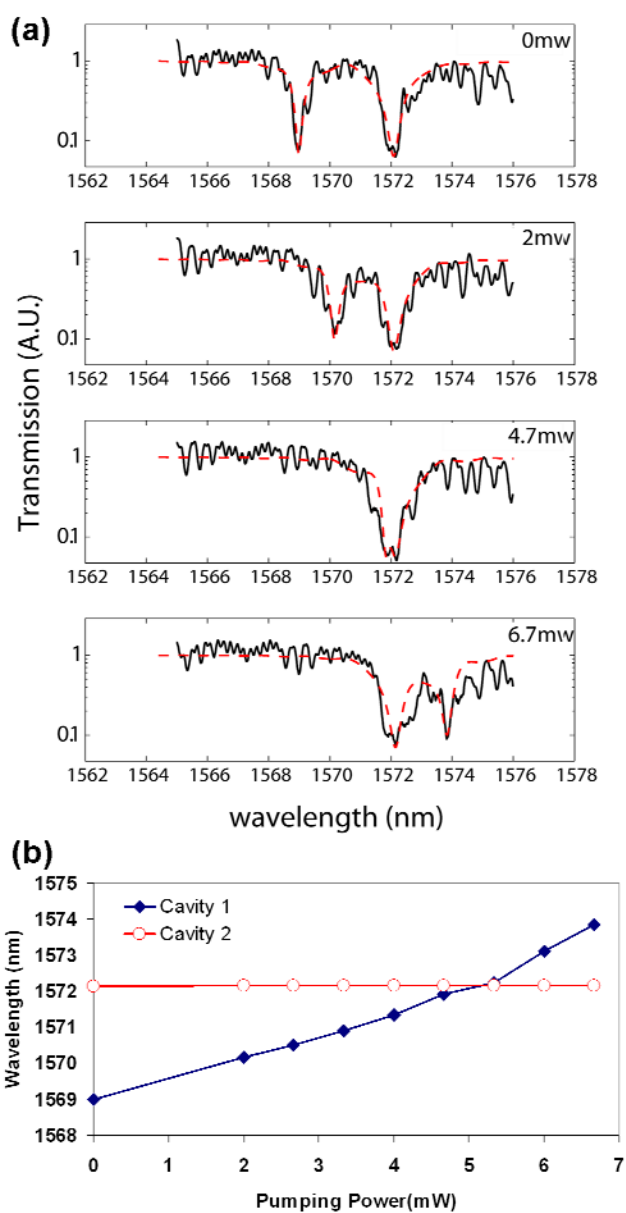


Figure 5.5. Experimental results of laser-pumped thermal tuning of photonic-crystal microcavities with laser pump light focused near microcavity C1. (a) Transmission spectra for pump powers between 0 and 6.7 mW. Solid, black lines show experimental data, and red, dashed lines show theoretical fits. (b) Resonance wavelengths (dip positions) as a function of pump power.

To tune the resonance wavelengths, the pump laser was focused on the surface of the device, in the vicinity of the microcavity C1. We avoided focusing the laser spot directly on the cavity, since the pump laser introduces free carriers in the silicon slab that result in optical loss. The effect of loss on Q_{int} can be reduced by focusing the laser spot several microns from the cavity, since the carrier concentration decreases with distance from the laser spot due to recombination. Figure 5.5(a) shows measured transmission spectra for the power delivered on the sample between 0 and 6.7 mW. The spectrum exhibits two clearly-separated resonance dips. (The additional oscillations seen in the spectrum are due to Fabry-Perot reflections from the ends of the device, and do not change substantially with laser power.) The resonance wavelengths are plotted in Figure 5.5(b). As the source power is increased, one resonance linearly shifts to higher wavelength and the other stays almost the same. We can infer that the longer-wavelength resonance is from C2, which is farther away from the laser focus and thus experiences less heating and less temperature-induced shift. From the maximum shift (4.85 nm) the temperature rise at C1 was estimated to be about 59K with 6.7 mW incident laser power. If farther detuned resonances are desired, the laser spot can be moved to C2. The larger-wavelength resonance will shift to an even larger wavelength while the resonance of C1 will stay the same. During the thermal tuning of C1, its Q_{int} decreases as power increases, due to loss, and reaches 6000 at maximum power, while its Q_{c} does not change significantly.

We have clearly experimentally demonstrated the use of laser-pumped thermal effects for differential tuning of microcavity wavelengths in silicon photonic-crystal slabs.

An initial difference of 3.15nm in the resonant wavelengths of two closely-separated microcavities was decreased to zero using the thermal gradient induced by a focused laser spot. A crossover in the resonant wavelengths was also demonstrated, showing a tunable range of more than 5 nm. Using multiple spots should allow the post-fabrication alignment of multiple microcavity resonances. This technique should be useful for the realization of increasingly complex devices employing multiple microcavities in photonic-crystal structures. Thermal tuning could be used to improve the performance of passive multi-cavity devices, such as filters. Moreover, combined with faster tuning methods such as free-carrier injection, dynamical reconfiguration schemes such as stopping-light systems could be realized in photonic-crystal structures.

6. EXPERIMENTS

Motivated by the fundamental and practical importance, inspired by the theoretical analysis, equipped with the design, fabrication and essential toolbox, we present experimental demonstration of the coherent interactions of photonic-crystal cavities in this chapter. Starting with a description of the experimental setup, we will then show EIT-like, flattop reflection optical resonances in a single structure, as well as an optical analogue to the superradiance effect. By changing the propagation phase in the waveguide between two cavities, we tuned the device behavior from EIT-like to flattop optical resonance. We also experimentally measured the group delay generated by the EIT-like optical resonance.

6.1. EXPERIMENTAL SETUP

The experimental setup is illustrated in Figure 6.1. A tunable laser source with a large tunable range is necessary to characterize the microcavities. Depending on availability, we typically used a laser with a tunable range of 1480 – 1583 nm. The output power is limited to a few milliwatts, so the laser is connected to an Erbium-Doped Fiber Amplifier (EDFA) during the alignment process when higher power is needed. Although the EDFA has an output power up to 2 watts, it was usually kept lower than 300 milliwatts to avoid damage to the waveguide.

The fiber-guided light is converted to a free-space beam by a collimator. Then distance from the collimating lens to the fiber can be adjusted to obtain the best spot size for the input coupling lens. A polarizer is placed between the collimator and the sample to control the input beam TE-polarized (in-plane polarization, magnetic field parallel to the hole axis) for the measurement. Since the polarization may change while tuning the wavelength, the polarizer also ensures stable polarization. After the polarizer, a beam sampler monitors the input power.

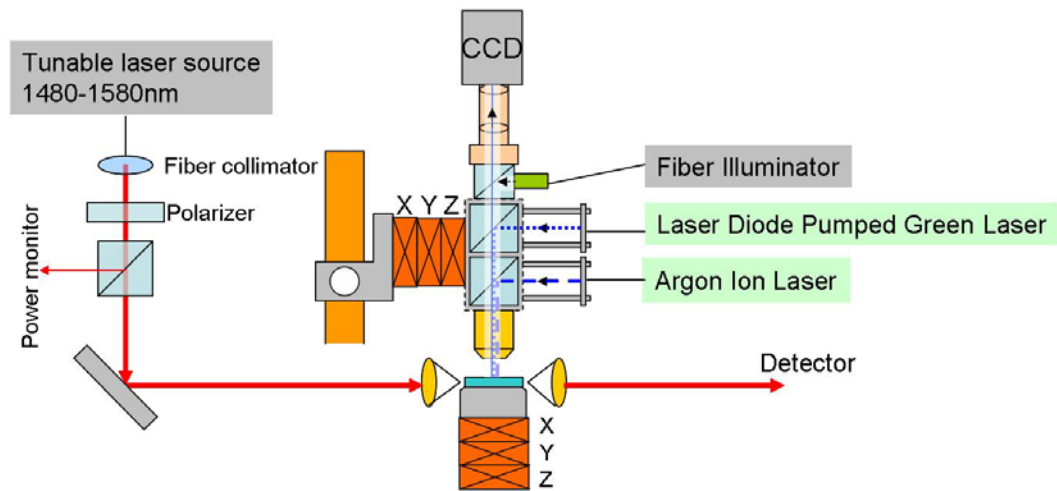


Figure 6.1. Schematic of the experimental setup. Sample waveguide is placed on a XYZ stage. In the horizontal direction, light from a tunable laser source is first coupled to the waveguide, and the transmitted power is detected at the other side of the waveguide. Above the sample, a microscope column is attached to another XYZ stage. Pumping laser beams are focused by the objective lens on the sample. A CCD camera, at the top of the column, is used to locate and monitor the laser spot and the cavity.

We coupled the free-space laser beam to the sub-micron waveguide through a high numerical aperture ($NA = 0.65$) lens and collected the transmitted light from another similar lens into a germanium infrared detector. Both the lens and the sample are mounted on three-axis translation stages. Electrostrictive actuators are employed to

control the position of the axes that are most sensitive to alignment. An infrared camera is also placed along with the detector for alignment and navigation purposes.

Above the sample, a vertical microscope column is placed on a three-axis stage for the purpose of laser-pumped tuning. At the bottom of the column, there is a 20x microscope objective lens with focal length 10 mm and numerical aperture 0.42. In the middle, beam splitters guide the pumping laser beams into the column from the fiber illuminator. One laser beam is from an Ar-ion laser with wavelength 488 nm or 514 nm, with relatively high power and a small focal spot. The other is from a portable diode pumped green laser, which is convenient in transporting the setup. In addition, two laser spots are generally necessary to control both the cavity resonant wavelength and the waveguide propagation phase. At the top of the microscope column, a CCD camera and a 7x zoom lens are placed to conveniently locate and monitor the laser spots relative to the photonic-crystal cavities.

6.2. TUNING THE PROPAGATION PHASE

6.2.1. DEVICE UNDER TEST

We consider a photonic-crystal structure in which two resonators are side-coupled to a waveguide (Figure 6.2), and experimentally demonstrate that the characteristics of coherent interaction between the two resonators can be drastically tuned by changing the refractive index of the waveguide. As a result, the transmission lineshape can be tuned from a flat-top band-reflection filter to an EIT-like lineshape and vice versa.

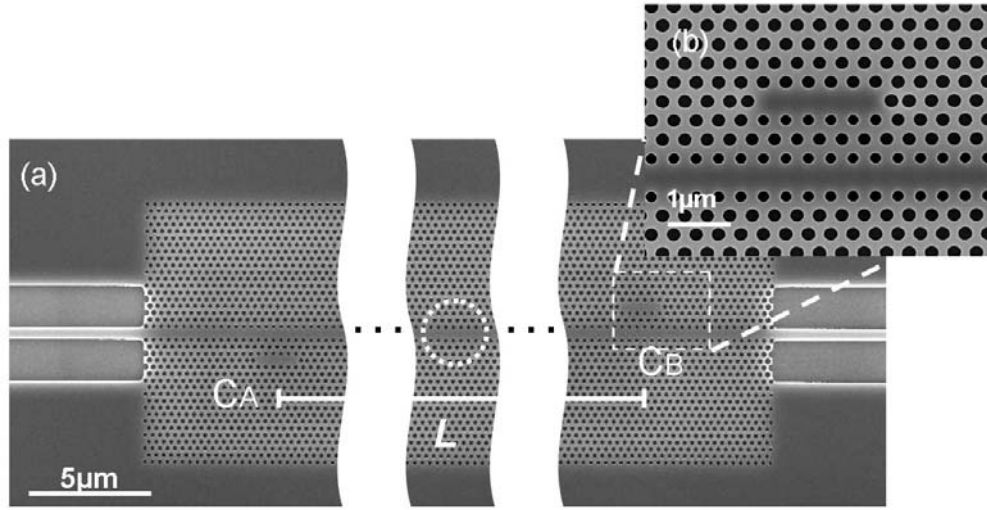


Figure 6.2. SEM images of the fabricated device for the demonstration of EIT-like optical resonance and flat-top reflection filter. (a) Top view of the photonic-crystal structure with two cavities side-coupled to one waveguide. (b) Magnified view of the microcavity C_B . The circle approximately corresponds to the size of the focal spot of the pumping laser. The actual heated region however is substantially larger due to thermal conductance.

Theoretically and graphically, Equation (2.21) and Figure 2.3 clearly show that a waveguide-resonator system, such as the one in Figure 6.2, can exhibit various lineshapes of transmission spectra depending on the resonant frequency detuning between the two cavities and the propagation phase in the waveguide between them. Motivated by the preceding analysis, we designed and fabricated a photonic-crystal structure in a suspended silicon membrane (Figure 6.2). The periodic region consisted of a triangular lattice of air holes with the lattice constant $a = 386\text{nm}$, and hole radius of 116nm . The nearest hole on either side of the resonator was shifted outward by 77nm to increase the intrinsic quality factor. The waveguide-resonator coupling occurred through a barrier of three rows of holes. Between the resonator and the waveguide, the radii of the six holes along the side of the resonator and the rows of holes along the side of the waveguide were reduced to 102nm to enhance the waveguide-cavity coupling. The propagation-

phase shift was achieved by laser-pumped thermal tuning on the waveguide. The two resonators were separated by $140a$ in the horizontal direction (L in Figure 6.2). By incorporating inverse tapers at the ends of the strip waveguide, we effectively improved coupling and minimized back reflection. The width of the strip waveguide in the inverse taper regions gradually decreased from 400nm to 150nm linearly towards the edge of the chip over a distance of $50\mu\text{m}$. In the transmission spectra shown in Figure 6.3 that will be discussed in more details below, there are only very weak Fabry-Perot oscillations due to the improved impedance matching at interfaces. The reduction of Fabry-Perot reflections is crucial in order to unambiguously demonstrate the predicted effects that arise entirely from the interference between the two resonators.

6.2.2. TRANSMISSION SPECTRA

Prior to any tuning, the device exhibited an EIT-like transmission spectrum in Figure 6.3(a) featuring a narrow transparency peak in a broad spectral region that had very little transmission. In the subsequent tuning experiments, we focused Ar-ion laser beam with a wavelength of 514nm into a spot of $2\sim 3\mu\text{m}$ in diameter (roughly the circled region in Figure 6.2), and gradually increased the pumping power. The heated region however was substantially larger than the laser spot size due to thermal conductance. At a pumping power of 1.4mW (Figure 6.3 (b)), the spectrum represented a cleaner EIT-like spectrum as compared with Figure 6.3 (a); it featured a transparency peak with a higher peak transmission and a near-symmetric lineshape. At a pumping power of 5.3mW, in Figure 6.3(c), the EIT-peak disappeared, and we instead observed a flat-top reflection response. At a pumping power of 11.2mW, the EIT peak was recovered. (Figure 6.3(d)).

Therefore the experiment has demonstrated the tuning between the EIT and the flat-top response lineshapes. The two resonators in this sample in the absence of external tuning already have similar resonance wavelengths, which facilitates the observation of various coherent interaction effects. In general, we can precisely control the detuning of the cavities by thermal differential tuning [24], which was discussed in Section 5.2.

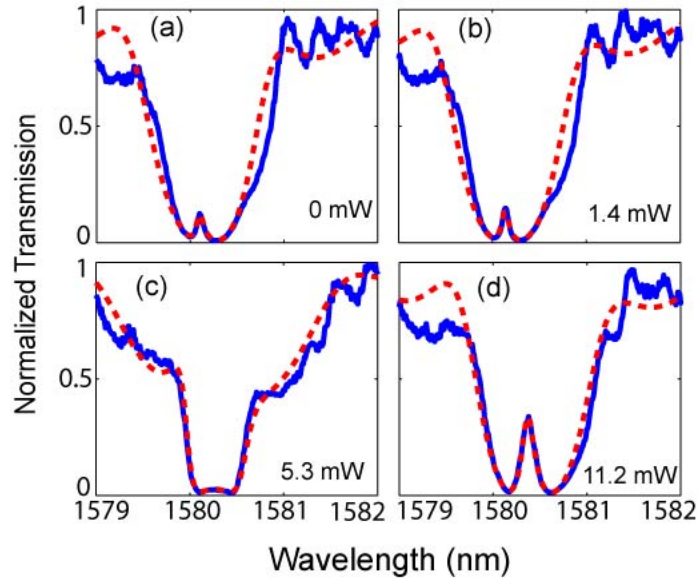


Figure 6.3. Experimental transmission spectra (blue solid line) and theoretical fits (red dashed line) of the photonic-crystal system of Figure 6.2, with a pump laser beam incident on the waveguide near the mid-point between the two microcavities. Curves (a) – (d) correspond to different pump powers. In particular, curves (a)(b)(d) exhibit a lineshape analogous to electromagnetically-induced transparency, with the transparency peak of 0.08, 0.07 and 0.15 in linewidth respectively, corresponding to a quality factor of 19800, 22600 and 10500 respectively, which are all substantially larger than the loaded Q of each individual cavity. Curve (c) exhibits a flat-top reflection response. The detuning of the two cavity resonances is 0.26, 0.26, 0.36 and 0.45 nm respectively in curves (a) – (d).

The experimental spectra shown in Figure 6.3 are well explained theoretically by Equation (2.21)-(2.23) with the fitting parameters in Table 6.1. In the experiments, the focused laser beam heats up a portion of the photonic crystal waveguide and the

refractive index of silicon increases with temperature by $1.85 \times 10^{-4}/\text{K}$ at $1.55 \mu\text{m}$ [68]. We assume that the waveguide propagation phase has a linear form $\phi_{\text{wg}}(\omega) = \tau\omega + \phi_0$, with $\tau = -6.0 \times 10^{-12} \text{ sec}$ as determined from the finite-difference time-domain simulation. We further assume that the slope of guided mode band diagram does not change substantially due to the tuning so that τ remains the same, and we vary ϕ_0 to fit the spectra at different tuning powers. As one of the fitting results, decreasing ϕ_0 with the laser power is consistent with the fact the temperature rise increases the refractive index and thus pulls the guided band downward in the band diagram. Other fitting parameters in Table 6.1 are the resonant wavelengths $\lambda_{A,B}$, the intrinsic quality factors $Q_{\text{int},A}$ and $Q_{\text{int},B}$, and the waveguide-resonator coupling quality factors $Q_{c,A}$ and $Q_{c,B}$. The theoretical fit agrees excellently with the experimental measurement.

Fig.	Power /mW	λ_A /nm	λ_B /nm	$Q_{\text{int},A}$	$Q_{\text{int},B}$	$Q_{c,A}$	$Q_{c,B}$	ϕ_0 / π
3(a)	0	1580.02	1580.28	13,000	13,000	3,900	2,200	2524.08
3(b)	1.4	1580.03	1580.29	13,000	13,000	3,900	2,200	2523.99
3(c)	5.3	1580.09	1580.45	13,000	13,000	3,900	2,200	2522.76
3(d)	11.2	1580.17	1580.62	13,000	13,000	3,900	2,200	2521.52

Table 6.1. The parameters used in Equation (2.21)-(2.23) to fit the experimental curves in Figure 6.3. The second column is the power of the laser beam that is delivered to the sample. In the remaining columns the subscripts A or B label the two resonators. $\lambda_{A,B}$ are the resonant wavelengths. $Q_{\text{int},A}$ and $Q_{\text{int},B}$ are the intrinsic quality factors. $Q_{c,A}$ and $Q_{c,B}$ are the waveguide-resonator coupling quality factors. ϕ_0 is a parameter that determines the waveguide propagation phase $\phi_{\text{wg}}(\omega) = \tau\omega + \phi_0$, where $\tau = -6.0 \times 10^{-12} \text{ sec}$ as calculated by the finite-difference time-domain simulation.

An important observation from Table 6.1 is that all figures are fitted by the *same* set of quality factors. Moreover, both the resonant wavelengths of the two cavities experience a small redshift due to thermal tuning. The detuning between them, however, is kept small enough so that the detuning does not alter the characteristic of the transmission lineshape. The change of the lineshape, instead, comes almost entirely from the change of the propagation phase ϕ_0 . In the spectrum of Figure 6.3(c), the round-trip phase at the center of the low-transmission range is close to $(2n + 1)\pi$, which is indeed the condition for the flat-top reflection response. On the other hand, the round-trip waveguide phase at transparency peak in Figure 6.3(a)(b)(d) are all very close to $2n\pi$, the condition of constructive interference between multiple reflections in order to generate the EIT-like optical resonance.

We demonstrated both EIT-like and flat-top reflection optical resonance in a single device structure by controlling the phase between the cavities. Both lineshapes are of substantial importance in practical applications, as shown in Chapter 1. The flat-top band-reflection filter, which reflects a narrow range of wavelengths while letting other wavelengths pass through, is a higher-order filter as compared to the regular Lorentzian lineshape commonly observed in photonic-crystal resonator filters. This filter lineshape is important for achieving low inter-channel cross-talk in wavelength-division multiplexing and robustness against fluctuations in input-signal wavelength in communication applications [37, 38]. The EIT-like optical resonance, on the other hand, renders an integrated optical system transparent at an otherwise highly reflective wavelength. The potential for slowing [33, 35], stopping [31] and time-reversing of light pulses [54] on

chip in such a system has profound impact for both fundamental science and application in optical communications. Our results on tuning therefore experimentally demonstrate substantial re-configurability, enabled by coherent resonant interactions in these structures. Moreover, in our results, while the EIT lineshape has an exact atomic physics analogue, the flat-top reflection filter does not. Demonstrating the tuning between these two effects thus indicates some of the unique richness in nanophotonic resonances.

6.2.3. ESTIMATION OF INDEX CHANGE

In the end, we estimate the temperature rise that is needed to achieve a change of 2π in the round-trip waveguide propagating phase. The experimental measurements (Figure 5.3) and detailed simulation [76] show that the temperature profile in the photonic-crystal slab exhibits a bell-shaped curve with full-width of about $10 \mu\text{m}$ at half-maximum and about $16 \mu\text{m}$ at $1/e$ -maximum. For simplicity, in this calculation, we approximate the bell-shaped temperature profile with a rectangular profile that gives rise to the same phase change.

Specifically, to achieve a round-trip-phase change of 2π , we have

$$2 \cdot \delta\beta(\omega) \cdot l = 2\pi, \quad (6.1)$$

where β is the wave vector and l is the length of the heated waveguide region. The equation above can be written as

$$\frac{\delta\beta}{\delta\omega} \cdot \delta\omega \cdot l = \pi. \quad (6.2)$$

Since $\frac{\delta\omega}{\omega} \approx \frac{\delta n}{n}$, which is the fractional change in the material index, while $\frac{\delta\beta}{\delta\omega} = \frac{n_g}{c_0}$ and

$\lambda_0 = \frac{2\pi c_0}{\omega}$, we have

$$\frac{\delta n}{n} = \frac{\lambda_0}{2l} \cdot \frac{1}{n_g}, \quad (6.3)$$

where n_g is the group index in the waveguide, c_0 is the speed of light in free space and λ_0 is the wavelength in free space. As a result, for a given length of the tuned region in the waveguide, the higher the group index, the smaller the index change required to shift a certain amount of propagation phase. In other words, the sensitivity of the phase to the induced change in the index of refraction can be drastically enhanced if one operates in the regimes of slow group velocities. A more detailed discussion can be found in [77].

For our waveguide, with $n_g = 16.67$ as determined from bandstructure calculations, also assuming that $l \approx 10\mu m$, we have a $\delta n \sim 0.016$ which is achievable with a temperature change of less than 100K, given $\Delta n / \Delta T = 1.85 \times 10^{-4} / K$ at $1.55\mu m$. Again, this number is consistent with the power delivered on the sample, about 11 milliwatts to achieve 2π phase shift.

6.3. EIT-LIKE OPTICAL RESONANCE AND GROUP DELAY

A key signature of the EIT-like optical resonance is the excess group delay. The delay is a consequence of multiple reflections of light waves in the waveguide between

the cavities. To illustrate this effect, we consider the case of Figure 6.3(b) and infer the group delay of the system from the parameters obtained from the theoretical fit. As shown in Figure 6.4, the EIT resonance corresponds to a peak delay of almost 20 ps, which significantly exceeds the maximum delay of 10ps as obtained by the sum of the contributions from the two individual resonances and the propagation in the waveguide. The EIT-like optical effect enhances the group delay by a factor of two.

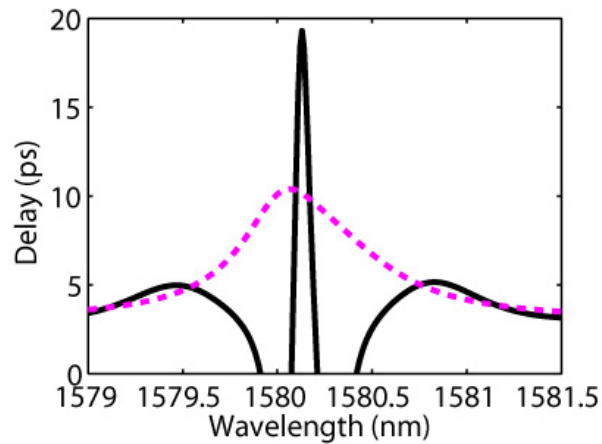


Figure 6.4. The solid line is the calculated delay for the EIT-like spectrum in Figure 6.3(b), using parameters in Table 6.1. The dashed line is the delay as obtained from a sum of contributions from the two individual resonances and the propagation in the waveguide. Notice the significant excess delay due to the coherent interference between the two resonances.

We present a direct time-domain measurement of the optical delay. In the experimental setup, light from a CW laser was modulated by a GHz sinusoidal signal. The modulated light was sent through two pathways, one through an optical fiber as the reference, the other through the photonic crystal cavity system that has the EIT-like resonance. The transmitted light from the photonic crystal was collected by a lens fiber. We obtained the optical delay by measuring the phase difference between the sinusoidal

waves from the two pathways. Group delays measured at different wavelengths were plotted by the red dots in Figure 6.5. Results displayed in Figure 6.5 have been shifted by such an arbitrary amount that the delay far from the EIT-like resonance is set to be zero. This data process subtracts the delay that is due to the traveling in the waveguides and fiber outside the interfered cavity system. As a result, the displayed delays are entirely generated by the EIT-like optical resonance. The peak delay was measured to be 20 ps. Given 54 μm center-to-center distance between the cavities in the transmission direction, the delay corresponds to a group index of 110. As a reference, the blue curve is the theoretical result calculated from the transmission spectrum.

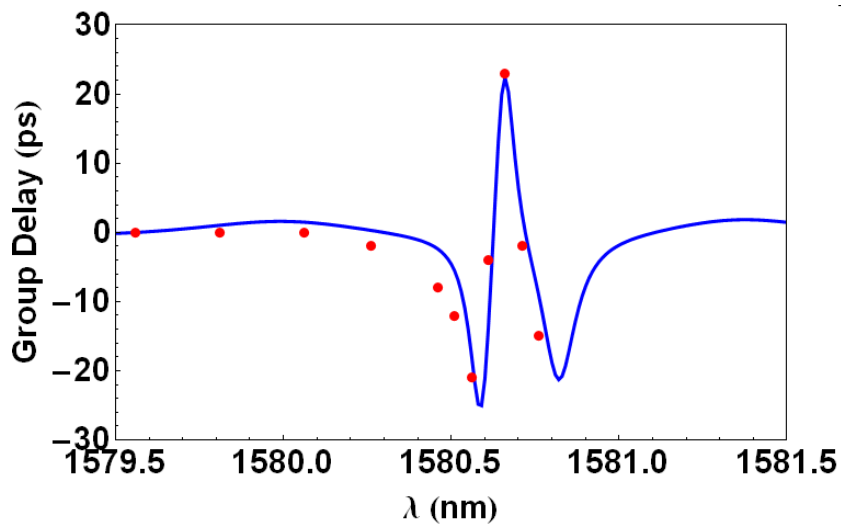


Figure 6.5. Delay spectrum of an EIT-like optical system. The blue curve is theoretically inferred group delay from the transmission spectrum. The red dots are experimentally measured delays. A maximum delay of 20 ps was generated by the EIT-like optical resonance.

In the absence of intrinsic loss, photons can be trapped in the system indefinitely when the cavities have the same resonance frequency and photons are on resonance with both cavities, resulting in a transparency peak with infinitesimal linewidth. In such a case,

the two cavities are completely decoupled from the input and output waveguides and the group delay is simply infinite. In the presence of intrinsic loss, light decays in the cavities,

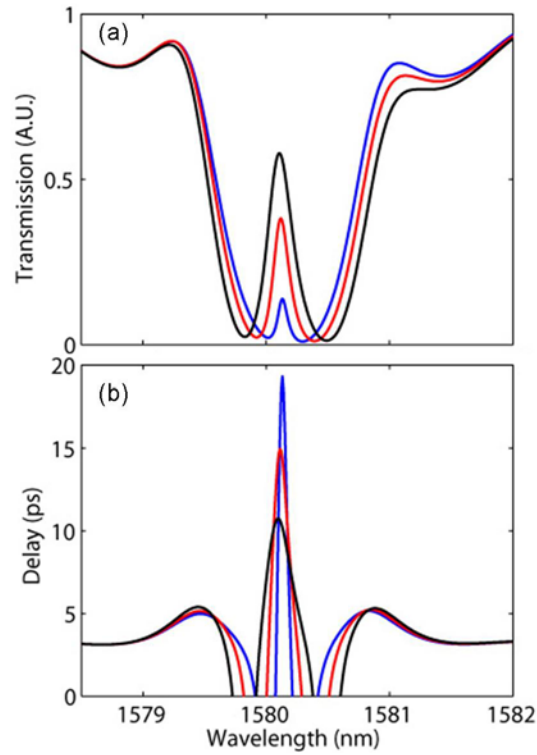


Figure 6.6. Theoretical transmission spectra and corresponding delay spectra of an EIT-like system with different cavity resonance detuning. In plotting the blue curves, fitting parameters for Figure 6.3(b) in Table 6.1 are used. In plotting the red and black curves, the resonant wavelength of cavity A was decreased by 0.1 nm incrementally and that of cavity B was increased by 0.1 nm incrementally.

and thus is not able to stay in the system indefinitely. In practice, in order to observe transmitted light, the system has to have a finite lifetime, so the frequency detuning of the two cavities has to be non-zero. The optical delay is very sensitive to frequency detuning. A smaller frequency detuning makes a larger group delay, but a lower transmitted power, because light stays longer in the lossy system. Figure 6.6 shows the theoretically

calculated transmission and delay spectra for different amounts of frequency detuning. The detuning can be controlled by the previously discussed thermal differential tuning.

6.4. OPTICAL ANALOGUE TO THE SUPERRADIANCE EFFECT

The superradiance effect [44], where the radiation emitted by N identical neighboring atoms interfere constructively, results in the enhancement of the spontaneous emission rate of the system by a factor of N . It has been observed using a variety of systems [45-51] when different emitters couple to a common mode of light. In this section, I present the experimental demonstration of an optical analogue to the superradiance effect in photonic-crystal cavities.

This work is along the direction of recent substantial efforts in mapping the coherence effects in atomic systems to on-chip photonic systems. One important example is the previously discussed all-optical analogue to the electromagnetically-induced transparency, which not only points out the conceptual link between atomic physics and nanophotonics, but also has led to applications of stopping and slowing light. This is a crucial step towards the development of integrated optical devices. The superradiance effect also has broad implications for integrated optics, as the enhancement of waveguide-resonator coupling is essential for low loss device applications.

6.4.1. EXPERIMENTAL RESULTS AND THEORETICAL FITTING

We consider a photonic-crystal device in Figure 6.7, in which the two resonators have resonant frequencies in close proximity to each other. The center-to-center

separation of the resonators is $140a$, where $a = 386$ nm, the nearest-neighbor hole separation (lattice constant) of the structure.

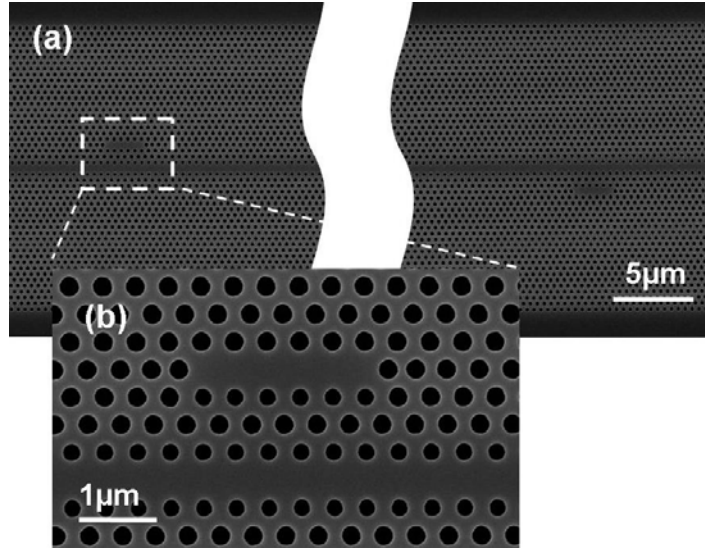


Figure 6.7. SEM images of the fabricated device for demonstration of the superradiance effect. (a) Top view of the PhC structure with two resonators. (b) Magnified view of a single resonator and a portion of waveguide.

We measured the transmission spectrum to investigate the waveguide-resonator coupling characteristics, since the coupling rate is directly related to the linewidth (Section 2.1). First, to measure the linewidth due to coupling between a single resonator and the waveguide, we detuned one of the resonators using laser-pumped thermal differential tuning as described in Section 5.2. The output of a 514nm Ar-ion laser was focused on the surface of the structure at a spot closer to one of the resonators. The temperature rise in the vicinity of the resonator increased the refractive index and caused a redshift of its resonant wavelength. Figure 6.8(a) shows the transmission spectrum of the device where the detuning between the resonators was $\Delta\lambda = 0.65$ nm. The theoretical fit of the full spectrum indicates a single resonator-waveguide coupling quality factor of

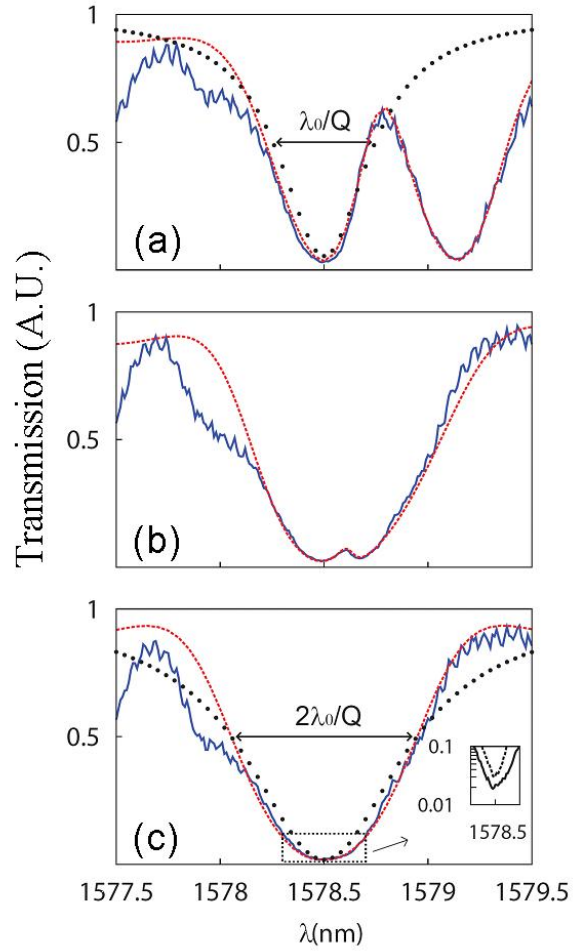


Figure 6.8. Experimental transmission spectrum (solid line) and theoretical fits (dashed line) for the two-resonator system shown in Figure 6.7 at different resonance frequency detuning $\Delta\lambda$ between resonators: (a) $\Delta\lambda = 0.65\text{nm}$, (b) $\Delta\lambda = 0.17\text{nm}$, (c) $\Delta\lambda = 0\text{nm}$. Plots in (a) include the theoretical transmission spectrum (dotted line) of a single-resonator system with coupling rate γ_c , and plots in (c) include the theoretical transmission spectrum (dotted line) of a single-resonator system with coupling rate $2\gamma_c$. The inset of (c) shows the depth of the experimental transmission dip (solid line) is deeper compared with the depth of the single-resonator system experimental transmission dip (dashed line) from (a), indicating enhancement of waveguide-resonance coupling in the superradiance regime of the two-resonator system.

$Q_c = 4,000$ and a single resonator intrinsic quality factor of $Q_{\text{int}} = 13,000$. The two transmission dips in Figure 6.8(a) are at the resonant frequencies of the two resonators.

We subsequently decreased the power of the pumping laser. As the resonance frequency detuning of the two resonators is reduced, there is increased interaction between the two resonators through the waveguide [Figure 6.8(b)]. Figure 6.8(c) shows the transmission spectrum of the device for the case when there was no frequency detuning between the two resonators. The transmission spectrum features a single transmission dip, with a lineshape closely resembling that for a waveguide coupling to a single resonator, with a linewidth twice as large as the dip generated by a single cavity. The linewidth corresponds to a quality factor of 1805, which, in comparison with the results in Figure 6.8(a), indicates a nearly two-fold enhancement in the resonator-waveguide coupling rate. This gives a strong indication of coherent, resonant interaction between the two resonators.

As additional experimental evidence of the superradiance effect, the minimum transmission in Figure 6.8(c) has a value of 0.0189, as compared to the minimum transmission value of 0.0297 in Figure 6.8(a) for the single resonance case. The enhancement of waveguide-resonator coupling in the superradiance regime leads to a higher reduction in the forward transmission as compared to the single-resonance case. This result agrees well with our theoretical discussion in Section 2.1: the smaller the coupling Q (or equivalently stronger coupling), the lower the transmittance.

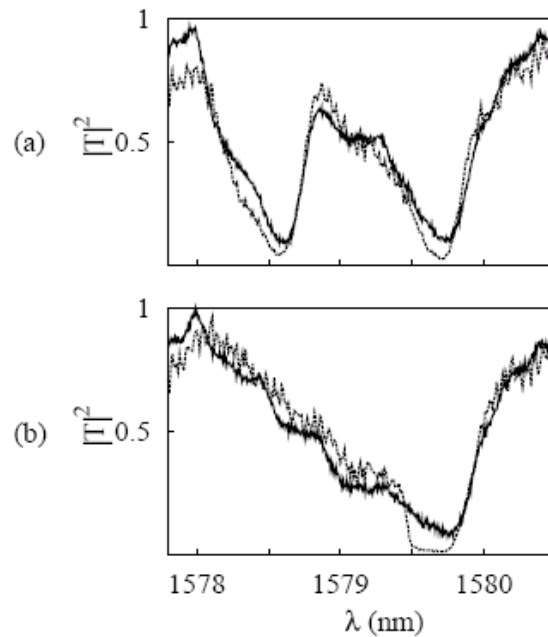


Figure 6.9. Comparison of experimental transmission spectrum of the two-resonator system using an incoherent ASE source (solid line), and a tunable coherent laser source (dashed line). Plots show system at different resonance frequency detunings, $\Delta\lambda$, between resonators.

We emphasize that this coherence effect between resonators is intrinsic to the structure, and is not enforced by the use of coherent excitation. This in fact can be anticipated theoretically. In the case where there exists intrinsic loss, and when the detuning between the two cavities is far smaller than the intrinsic decay rate, under the superradiant condition, the superradiant state is in fact the only state accessible to external radiation, as the subradiant state is suppressed (Section 2.2.3). In other words, for all practical purposes, here it is the only state in the system. The existence of such a state is independent of the excitation scheme. To prove this point experimentally, we measured the transmission spectrum of the structure with a coherent laser source and with an incoherent amplified spontaneous emission (ASE) source, as shown in Figure 6.9. A comparison of the two spectra showed that they essentially agree with one another, either

in the presence or in the absence of the tuning laser, indicating that the existence of the superradiant state is independent of the excitation scheme.

6.4.2. RESONATOR SEPARATION

In contrast to the previous demonstrated superradiance effect where emitters have to be placed within a wavelength of each other, the all-optical analogue to the superradiance effect that we showed was observed in an optical resonator system where the two resonators are separated by a distance much longer than the wavelength. This was enabled by the use of a single-mode tightly-confined waveguide, and the specific design that enabled strong waveguide-resonator coupling. As a result, the resonators couple through a restricted one-dimensional photon continuum, which leads to the superradiance effect.

We subsequently analyze the resonator separation dependence of the superradiance effect in the system shown in Figure 6.7. Figure 6.10 shows the analytical power transmission spectrum and the impulse response obtained using Equation (2.21) for various resonator separations, L . In plotting Figure 6.10, the single resonator-waveguide coupling quality factor was $Q_c = 4,000$, the group velocity in the waveguide was $v_g = 18 \times 10^6$ m/s, and the resonators were assumed to have a small intrinsic loss that suppresses the subradiant state. In the case of separation $L = 0$ (Figure 6.10(a)), the transmission spectrum shows a Lorentzian dip with a full width at half maximum $2\lambda / Q$ while the impulse response shows an exponential decay rate with time constant twice as fast as the single resonator decay rate into the waveguide, indicating the superradiance

effect. When the resonator separation L is non-zero, there is a finite roundtrip delay $2L/v_g$ as the photon propagates between resonators, and, as a result, additional dips due to the Fabry-Perot effect with frequency separation $\Delta\omega/2\pi \approx v_g/2L$ are observed in the transmission spectrum (Figure 6.10(b) and Figure 6.10(c)). However, as long as the frequency separation between nearby Fabry-Perot resonances satisfies $\Delta\omega > 2\omega/Q$, the center resonance dip around frequency ω_0 still has approximately twice the linewidth of a single resonance (Figure 6.10(b)). Moreover, the impulse response exhibits an exponential decay envelope with a decay rate that is twice of that of a single resonance. Thus, the superradiant state persists in this case, provided that the resonator separation satisfies: $L < L_0 \equiv \frac{\pi v_g Q_c}{2\omega_0}$. In the opposite limit, when $L > L_0$, the frequency spacing of the Fabry-Perot resonances becomes smaller compared with the linewidth of the superradiant state (Figure 6.10(c)). The impulse response thus consists of a large number of oscillations, without an enhanced decay rate in its envelope. After the initial superradiant state decay at $t < 20 \text{ ps} \cong 2L/v_g$, the discontinuity at $t > 20\text{ps}$ is the delayed energy decay from the system after the photon roundtrip time (Figure 6.10(c)). In our experiment, the distance L_0 is estimated to be $95.1 \text{ }\mu\text{m}$. By choosing a resonator separation $L=54.04\mu\text{m}$, we are therefore in the superradiant regime in spite of a large separation of the two resonators by many wavelengths.

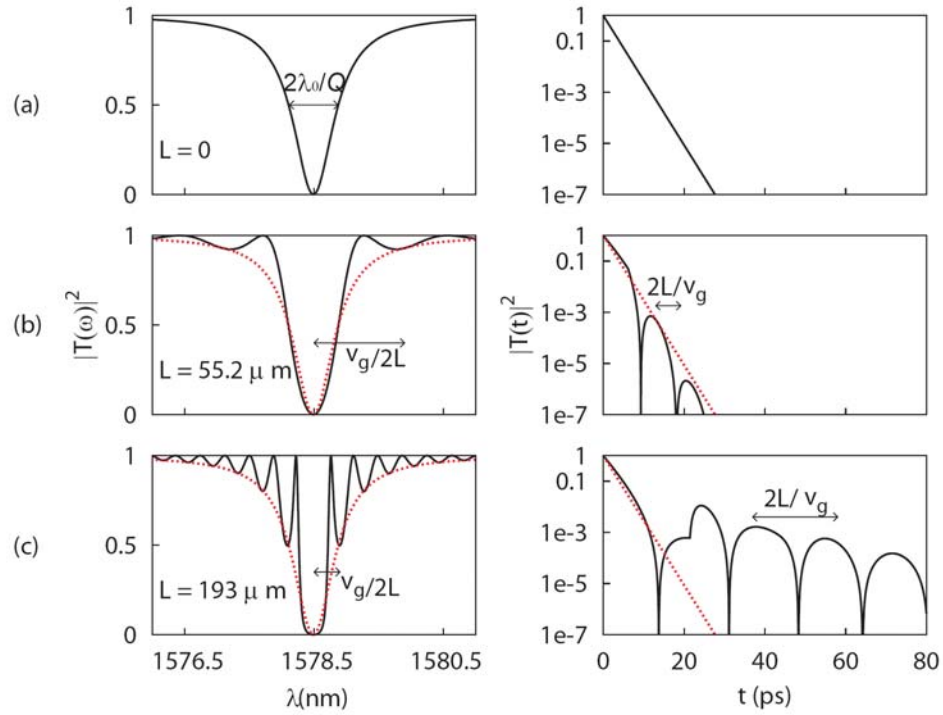


Figure 6.10. Theoretical plots from coupled-mode theory showing the power transmission spectrum (left, solid line) and the impulse response (right, solid line) for different cavity separations L in Figure 1. Plots in (b) and (c) include the $L = 0$ plots (dotted line).

The superradiance effect has broad implications for on-chip photonic integration, where strong waveguide-resonator coupling is essential for low loss device operation. Here, one key figure of merit is the ratio between the in-plane waveguide-resonator coupling rate and the out-of-plane radiation loss rate. Our work indicates this ratio can be enhanced through coherence effects. In addition, this result provides an indication of enforced long-distance coherence between two remotely placed resonances, through the strong coupling to a common waveguide. While the present experiment is entirely a classical electromagnetic effect, one can certainly anticipate that such a coherent effect can be enforced between quantum objects (for example, two two-level systems) as well.

7. CONCLUSION

The work contained in this dissertation demonstrated a number of coherent interactions that are of substantial theoretical and practical significance in on-chip photonic-crystal cavities, namely optical analogues to electromagnetically induced transparency (EIT) and the superradiance effect, as well as a flattop reflection filter. The results mapped the phenomena in quantum mechanics to classic physics, and pointed the conceptual links between atomic physics and nanophotonics.

We first presented the interconnections between the coherences in the framework of coupled mode theory. In particular, all the coherences can be enforced by the same configuration with two cavities side-coupled to a waveguide. Furthermore, we experimentally demonstrated the coherent interactions by employing photonic-crystal slabs.

As the first part of the experimental work, we smoothly changed the transmission lineshape of a single structure from EIT-like to flattop reflection optical resonance, by tuning the refractive index and thus the propagation phase in the waveguide between two cavities. When the propagation phase is an even multiple of π , constructive interference between multiple reflections renders the system transparency that closely resembles EIT. When the propagation phase is an odd multiple of π , the structure behaves as a flat-top reflection filter. This tuning shows substantial re-configurability in such a nanophotonic

structure, and also indicates the coherent nature of resonant interaction in such a system. Moreover, in our results, while the EIT lineshape has an exact atomic physics analogue, the flat-top reflection filter does not. Demonstrating the tuning between these two effects thus indicates some of the unique richness in nanophotonic resonances.

In the second part, we demonstrated an optical analogue to the superradiance effect, in which the coherent interaction enhances waveguide-resonator coupling. We showed that a two-cavity system with constructive interferences between reflecting waves could exhibit a combination of superradiance and subradiance modes. However, when the detuning is far smaller than the cavity loss rate, the presence of the cavity intrinsic loss suppresses the subradiance mode, so the superradiance mode is the only accessible state. Additionally, we provided an experimental demonstration of the structural tuning of the superradiance effect. In contrast to all the previously demonstrated superradiance effects where emitters had to be placed within a distance shorter than a wavelength, the all-optical analogue to the superradiance effect that we showed was observed in an optical resonator system where two resonators are separated by a distance much longer than the wavelength. This was enabled by the use of a single-mode tightly-confined waveguide, and the specific design that enabled strong waveguide-resonator coupling. As a result, the resonators coupled through a restricted one-dimensional photon continuum.

In order to experimentally demonstrate the coherent interactions, we designed photonic crystal structures to enforce the coherences and strip waveguides to facilitate transmission measurement. Inverse tapers were employed to improve impedance and modal size matching, in order to reduce back reflections at coupling interfaces and

suppress the corresponding Fabry-Perot oscillations. The consequent clean transmission spectra are essential for unambiguously observing the coherent features in the system.

We developed a fabrication process to make high-quality photonic crystal slabs with strip waveguides in a SOI platform. The photonic crystal slabs were suspended in air to maximize the index contrast and maintain the $z=0$ reflection symmetry. The strip waveguides, however, were surrounded by oxide cladding for robustness. Good quality of fabricated photonic crystal structures was verified by statistical analysis based on SEM graphs. In addition, SEM graphs were employed as the input to simulations, and the simulated results agreed well with the experimentally measured results.

Despite the good fabrication results, inevitable geometrical disorders kept us from making identical photonic-crystal cavities. Nevertheless, for the coherent schemes, cavity resonances are required to be aligned within their linewidth or better. We developed laser-pumped tuning schemes to control a cavity in a desired resonant frequency and even tune its intrinsic loss rate. Thermal differential tuning was employed to align and detune resonances in multi-cavity structures. This post-fabrication technique substantially relaxed fabrication tolerance, and should be useful for increasingly complex multi-cavity devices.

All the coherences are of great importance in applications. First of all, EIT-like optical resonance renders an integrated optical system transparent over a very narrow frequency range which is otherwise highly reflective. The potential for slowing, stopping and time-reversing of light pulses on chip has profound implications. In particular, we

measured the group delay generated by an EIT-like optical resonance. A maximum delay of 20 ps was observed and it corresponded to a group index over 110. The EIT effect, which was the consequence of *multiple* reflections between the cavities, enhances the group delay by a factor of two as compared to the delay contributed only from the reflections at both cavities and propagation in the waveguide between the cavities. The group delay from an EIT system is highly sensitive to the frequency detuning between the cavities. Since the cavity detuning can be controlled by the refractive index tuning, the EIT-like transparency peak can be dynamically controlled to achieve an optical delay of a light pulse beyond the constraint of its bandwidth imposed by the delay-bandwidth product limit. Second, the flat-top band-reflection filter reflects a narrow range of wavelengths while letting other wavelengths pass through. It features a flattened resonance and sharper transition from the transmission to reflection band, and is a higher-order filter as compared to the regular Lorentzian lineshape commonly observed in photonic-crystal resonator filters. This filter lineshape is important for achieving low inter-channel cross-talk in wavelength-division multiplexing and robustness against fluctuations in input-signal wavelength in communication applications. Third, the superradiance effect enhances waveguide-resonator coupling, essential for low-loss on-chip photonic integration. In many applications, one key figure of merit is the ratio between the in-plane waveguide-resonator coupling rate and the out-of-plane radiation loss rate. This ratio can be enhanced through the superradiant coherence. In addition, our work provided an indication of enforced long-distance coherence between two remotely placed resonators through strong coupling to a waveguide.

8. BIBLIOGRAPHY

1. J. D. Joannopoulos, *Photonic crystals : molding the flow of light* (Princeton University Press, Princeton, 2008).
2. Rayleigh, "On the maintenance of vibrations by forces of double frequency, and on the propagation of waves through a medium endowed with a periodic structure," in *Philosophical Magazine*(1887), pp. 145-159.
3. E. Yablonovitch, "Inhibited Spontaneous Emission in Solid-State Physics and Electronics," *Physical Review Letters* **58**, 2059 (1987).
4. S. John, "Strong localization of photons in certain disordered dielectric superlattices," *Physical Review Letters* **58**, 2486 (1987).
5. S. E. Harris, J. E. Field, and A. Imamoglu, "Nonlinear optical processes using electromagnetically induced transparency," *Physical Review Letters* **64**, 1107 (1990).
6. K. J. Boller, A. Imamolu, and S. E. Harris, "Observation of electromagnetically induced transparency," *Physical Review Letters* **66**, 2593 (1991).
7. J. H. Eberly, M. L. Pons, and H. R. Haq, "Dressed-field pulses in an absorbing medium," *Physical Review Letters* **72**, 56 (1994).
8. L. V. Hau, S. E. Harris, Z. Dutton, and C. H. Behroozi, "Light speed reduction to 17 metres per second in an ultracold atomic gas," *Nature* **397**, 594-598 (1999).
9. N. S. Ginsberg, S. R. Garner, and L. V. Hau, "Coherent control of optical information with matter wave dynamics," *Nature* **445**, 623-626 (2007).
10. M. D. Lukin, S. F. Yelin, and M. Fleischhauer, "Entanglement of Atomic Ensembles by Trapping Correlated Photon States," *Physical Review Letters* **84**, 4232 (2000).
11. D. F. Phillips, A. Fleischhauer, A. Mair, R. L. Walsworth, and M. D. Lukin, "Storage of Light in Atomic Vapor," *Physical Review Letters* **86**, 783 (2001).
12. C. Liu, Z. Dutton, C. H. Behroozi, and L. V. Hau, "Observation of coherent optical information storage in an atomic medium using halted light pulses," *Nature* **409**, 490-493 (2001).
13. S. E. Harris, "Electromagnetically Induced Transparency in an Ideal Plasma," *Physical Review Letters* **77**, 5357 (1996).

14. A. G. Litvak, and M. D. Tokman, "Electromagnetically Induced Transparency in Ensembles of Classical Oscillators," *Physical Review Letters* **88**, 095003 (2002).
15. D. D. Smith, H. Chang, K. A. Fuller, A. T. Rosenberger, and R. W. Boyd, "Coupled-resonator-induced transparency," *Physical Review A* **69**, 063804 (2004).
16. L. Maleki, A. B. Matsko, A. A. Savchenkov, and V. S. Ilchenko, "Tunable delay line with interacting whispering-gallery-moderesonators," *Opt. Lett.* **29**, 626-628 (2004).
17. W. Suh, Z. Wang, and S. Fan, "Temporal coupled-mode theory and the presence of non-orthogonal modes in lossless multimode cavities," *Quantum Electronics, IEEE Journal of* **40**, 1511-1518 (2004).
18. S. Fan, "Sharp asymmetric line shapes in side-coupled waveguide-cavity systems," *Applied Physics Letters* **80**, 908-910 (2002).
19. S. Fan, W. Suh, and J. D. Joannopoulos, "Temporal coupled-mode theory for the Fano resonance in optical resonators," *J. Opt. Soc. Am. A* **20**, 569-572 (2003).
20. Q. Xu, S. Sandhu, M. L. Povinelli, J. Shakya, S. Fan, and M. Lipson, "Experimental Realization of an On-Chip All-Optical Analogue to Electromagnetically Induced Transparency," *Physical Review Letters* **96**, 123901 (2006).
21. X. Yang, M. Yu, D.-L. Kwong, and C. W. Wong, "All-Optical Analog to Electromagnetically Induced Transparency in Multiple Coupled Photonic Crystal Cavities," *Physical Review Letters* **102**, 173902 (2009).
22. J. Pan, Y. Huo, S. Sandhu, N. Stuhmann, M. L. Povinelli, J. S. Harris, M. M. Fejer, and S. Fan, "Tuning the Coherent Interaction in an On-Chip Photonic-Crystal Waveguide-Resonator System," submitted (2010).
23. Q. Xu, J. Shakya, and M. Lipson, "Direct measurement of tunable optical delays on chip analogue to electromagnetically induced transparency," *Opt. Express* **14**, 6463-6468 (2006).
24. J. Pan, Y. Huo, K. Yamanaka, S. Sandhu, L. Scaccabarozzi, R. Timp, M. L. Povinelli, S. Fan, M. M. Fejer, and J. S. Harris, "Aligning microcavity resonances in silicon photonic-crystal slabs using laser-pumped thermal tuning," *Applied Physics Letters* **92**, 103114 (2008).
25. T. Asano, W. Kunishi, M. Nakamura, B. S. Song, and S. Noda, "Dynamic wavelength tuning of channel-drop device in two-dimensional photonic crystal slab," *Electronics Letters* **41**, 37-38 (2005).
26. Q. Xu, P. Dong, and M. Lipson, "Breaking the delay-bandwidth limit in a photonic structure," *Nat Phys* **3**, 406-410 (2007).
27. F. Raineri, C. Cojocar, R. Raj, P. Monnier, A. Levenson, C. Seassal, X. Letartre, and P. Viktorovitch, "Tuning a two-dimensional photonic crystal resonance via optical carrierinjection," *Opt. Lett.* **30**, 64-66 (2005).

28. J. J. Longdell, E. Fraval, M. J. Sellars, and N. B. Manson, "Stopped Light with Storage Times Greater than One Second Using Electromagnetically Induced Transparency in a Solid," *Physical Review Letters* **95**, 063601 (2005).
29. M. F. Yanik, and S. Fan, "Stopping Light All Optically," *Physical Review Letters* **92**, 083901 (2004).
30. M. F. Yanik, and S. Fan, "Stopping and storing light coherently," *Physical Review A* **71**, 013803 (2005).
31. M. F. Yanik, W. Suh, Z. Wang, and S. Fan, "Stopping Light in a Waveguide with an All-Optical Analog of Electromagnetically Induced Transparency," *Physical Review Letters* **93**, 233903 (2004).
32. M. Notomi, K. Yamada, A. Shinya, J. Takahashi, C. Takahashi, and I. Yokohama, "Extremely Large Group-Velocity Dispersion of Line-Defect Waveguides in Photonic Crystal Slabs," *Physical Review Letters* **87**, 253902 (2001).
33. A. Yariv, Y. Xu, R. K. Lee, and A. Scherer, "Coupled-resonator optical waveguide: a proposal and analysis," *Opt. Lett.* **24**, 711-713 (1999).
34. G. Lenz, B. J. Eggleton, C. K. Madsen, and R. E. Slusher, "Optical delay lines based on optical filters," *Quantum Electronics, IEEE Journal of* **37**, 525-532 (2001).
35. Z. Wang, and S. Fan, "Compact all-pass filters in photonic crystals as the building block for high-capacity optical delay lines," *Physical Review E* **68**, 066616 (2003).
36. J. Pan, S. Sandhu, Y. Huo, M. L. Povinelli, M. M. Fejer, S. Fan, and J. S. Harris, "Optical Analogue to Electromagnetically Induced Transparency in Photonic Crystals, Simulation and Experiments," in *Slow and Fast Light*(Optical Society of America, 2007), p. SWB2.
37. Y. Akahane, T. Asano, H. Takano, B.-S. Song, Y. Takana, and S. Noda, "Two-dimensional photonic-crystal-slab channel-drop filter with flat-top response," *Opt. Express* **13**, 2512-2530 (2005).
38. D. K. Jacob, S. C. Dunn, and M. G. Moharam, "Flat-Top Narrow-Band Spectral Response Obtained from Cascaded Resonant Grating Reflection Filters," *Appl. Opt.* **41**, 1241-1245 (2002).
39. W. Suh, and S. Fan, "Mechanically switchable photonic crystal filter with either all-pass transmission or flat-top reflection characteristics," *Opt. Lett.* **28**, 1763-1765 (2003).
40. W. Suh, and S. Fan, "All-pass transmission or flattop reflection filters using a single photonic crystal slab," *Applied Physics Letters* **84**, 4905-4907 (2004).
41. S. Fan, P. R. Villeneuve, J. D. Joannopoulos, M. J. Khan, C. Manolatou, and H. A. Haus, "Theoretical analysis of channel drop tunneling processes," *Physical Review B* **59**, 15882 (1999).

42. M. J. Khan, C. Manolatou, F. Shanhui, P. R. Villeneuve, H. A. Haus, and J. D. Joannopoulos, "Mode-coupling analysis of multipole symmetric resonant add/drop filters," *Quantum Electronics, IEEE Journal of* **35**, 1451-1460 (1999).
43. B. E. Little, S. T. Chu, H. A. Haus, J. Foresi, and J. P. Laine, "Microring resonator channel dropping filters," *Lightwave Technology, Journal of* **15**, 998-1005 (1997).
44. R. H. Dicke, "Coherence in Spontaneous Radiation Processes," *Physical Review* **93**, 99 (1954).
45. N. Skribanowitz, I. P. Herman, J. C. MacGillivray, and M. S. Feld, "Observation of Dicke Superradiance in Optically Pumped HF Gas," *Physical Review Letters* **30**, 309 (1973).
46. C. Greiner, B. Boggs, and T. W. Mossberg, "Superradiant Emission Dynamics of an Optically Thin Material Sample in a Short-Decay-Time Optical Cavity," *Physical Review Letters* **85**, 3793 (2000).
47. R. G. DeVoe, and R. G. Brewer, "Observation of Superradiant and Subradiant Spontaneous Emission of Two Trapped Ions," *Physical Review Letters* **76**, 2049 (1996).
48. M. Scheibner, T. Schmidt, L. Worschech, A. Forchel, G. Bacher, T. Passow, and D. Hommel, "Superradiance of quantum dots," *Nat Phys* **3**, 106-110 (2007).
49. X. H. Zhang, S. J. Chua, A. M. Yong, S. Y. Chow, H. Y. Yang, S. P. Lau, and S. F. Yu, "Exciton radiative lifetime in ZnO quantum dots embedded in SiO₂ matrix," *Applied Physics Letters* **88**, 221903-221903 (2006).
50. M. Hubner, J. P. Prineas, C. Ell, P. Brick, E. S. Lee, G. Khitrova, H. M. Gibbs, and S. W. Koch, "Optical Lattices Achieved by Excitons in Periodic Quantum Well Structures," *Physical Review Letters* **83**, 2841 (1999).
51. T. F. Finnegan, and S. Wahlsten, "Observation of coherent microwave radiation emitted by coupled Josephson junctions," *Applied Physics Letters* **21**, 541-544 (1972).
52. J. Pan, S. Sandhu, Y. Huo, N. Stuhmann, M. L. Povinelli, J. S. Harris, M. M. Fejer, and S. Fan, "Experimental demonstration of an all-optical analogue to the superradiance effect in an on-chip photonic crystal resonator system," *Physical Review B* **81**, 041101(R) (2010).
53. H. A. Haus, *Waves and fields in optoelectronics* (Prentice-Hall, Englewood Cliffs, NJ, 1984).
54. M. F. Yanik, and S. Fan, "Time Reversal of Light with Linear Optics and Modulators," *Physical Review Letters* **93**, 173903 (2004).
55. Y. Akahane, T. Asano, B.-S. Song, and S. Noda, "High-Q photonic nanocavity in a two-dimensional photonic crystal," *Nature* **425**, 944-947 (2003).

56. D. Englund, I. Fushman, and J. Vuckovic, "General recipe for designing photonic crystal cavities," *Opt. Express* **13**, 5961-5975 (2005).
57. K. Hwang, and G. Song, "Design of a high-Q channel add-drop multiplexer based on the two-dimensional photonic-crystal membrane structure," *Opt. Express* **13**, 1948-1957 (2005).
58. A. Taflove, and S. C. Hagness, *Computational electrodynamics : the finite-difference time-domain method* (Artech House, Boston, 2005).
59. D. Taillaert, W. Bogaerts, P. Bienstman, T. F. Krauss, P. Van Daele, I. Moerman, S. Verstuyft, K. De Mesel, and R. Baets, "An out-of-plane grating coupler for efficient butt-coupling between compact planar waveguides and single-mode fibers," *Quantum Electronics, IEEE Journal of* **38**, 949-955 (2002).
60. V. R. Almeida, R. R. Panepucci, and M. Lipson, "Nanotaper for compact mode conversion," *Opt. Lett.* **28**, 1302-1304 (2003).
61. S. McNab, N. Moll, and Y. Vlasov, "Ultra-low loss photonic integrated circuit with membrane-type photonic crystal waveguides," *Opt. Express* **11**, 2927-2939 (2003).
62. A. Talneau, P. Lalanne, M. Agio, and C. M. Soukoulis, "Low-reflection photonic-crystal taper for efficient coupling between guide sections of arbitrary widths," *Opt. Lett.* **27**, 1522-1524 (2002).
63. Y. Xu, R. K. Lee, and A. Yariv, "Adiabatic coupling between conventional dielectric waveguides and waveguides with discrete translational symmetry," *Opt. Lett.* **25**, 755-757 (2000).
64. T. Asano, B.-S. Song, and S. Noda, "Analysis of the experimental Q factors (~ 1 million) of photonic crystal nanocavities," *Opt. Express* **14**, 1996-2002 (2006).
65. L.-L. Lin, Z.-Y. Li, and B. Lin, "Engineering waveguide-cavity resonant side coupling in a dynamically tunable ultracompact photonic crystal filter," *Physical Review B* **72**, 165330 (2005).
66. S. Fan, P. R. Villeneuve, J. D. Joannopoulos, and H. A. Haus, "Channel Drop Tunneling through Localized States," *Physical Review Letters* **80**, 960 (1998).
67. A. Faraon, D. Englund, I. Fushman, J. Vuckovic, N. Stoltz, and P. Petroff, "Local quantum dot tuning on photonic crystal chips," *Applied Physics Letters* **90**, 213110-213113 (2007).
68. G. Cocorullo, F. G. Della Corte, and I. Rendina, "Temperature dependence of the thermo-optic coefficient in crystalline silicon between room temperature and 550 K at the wavelength of 1523 nm," *Applied Physics Letters* **74**, 3338-3340 (1999).
69. C. Manolatou, and M. Lipson, "All-optical silicon modulators based on carrier injection by two-photon absorption," *Lightwave Technology, Journal of* **24**, 1433-1439 (2006).

70. R. Soref, and B. Bennett, "Electrooptical effects in silicon," *Quantum Electronics, IEEE Journal of* **23**, 123-129 (1987).
71. I. Marki, M. Salt, H. P. Herzig, R. Stanley, L. El Melhaoui, P. Lyan, and J. M. Fedeli, "Optically tunable microcavity in a planar photonic crystal silicon waveguide buried in oxide," *Opt. Lett.* **31**, 513-515 (2006).
72. S. Sandhu, M. L. Povinelli, and S. Fan, "Stopping and time reversing a light pulse using dynamic loss tuning of coupled-resonator delay lines," *Opt. Lett.* **32**, 3333-3335 (2007).
73. R. S. Muller, T. I. Kamins, and M. Chan, *Device electronics for integrated circuits* (John Wiley & Sons, New York, 2003).
74. R. F. Pierret, *Semiconductor device fundamentals* (Addison-Wesley, Reading, Mass., 1996).
75. T. Tanabe, M. Notomi, S. Mitsugi, A. Shinya, and E. Kuramochi, "Fast bistable all-optical switch and memory on a silicon photonic crystal on-chip," *Opt. Lett.* **30**, 2575-2577 (2005).
76. N. Stuhmann, "Master Thesis: Thermal Tuning of Photonic Slab Structures," (2010).
77. M. Soljacic, S. G. Johnson, S. Fan, M. Ibanescu, E. Ippen, and J. D. Joannopoulos, "Photonic-crystal slow-light enhancement of nonlinear phase sensitivity," *J. Opt. Soc. Am. B* **19**, 2052-2059 (2002).